University of Cincinnati

Date: 3/30/2016

I, Carson L Willey, hereby submit this original work as part of the requirements for the degree of Doctor of Philosophy in Engineering Mechanics.

It is entitled:

Ultrasonic guided wave tomography for wall thickness mapping in pipes

Student's name: **Carson L Willey**

This work and its defense approved by:

Committee chair: Francesco Simonetti, Ph.D.

Committee member: Jongguen Lee, Ph.D.

Committee member: Guirong Liu, Ph.D.

Committee member: T. Douglas Mast, Ph.D.

19712

Ultrasonic guided wave tomography for wall thickness mapping in pipes

A dissertation submitted to the
Graduate School
of the University of Cincinnati
in partial fulfillment of the
requirements for the degree of

Doctor of Philosophy

in the Department of Aerospace Engineering and Engineering Mechanics
of the College of Engineering and Applied Science

by

Carson L. Willey
M.S. Miami University 2011

Committee Chair: Francesco Simonetti, Ph.D.

Abstract

Corrosion and erosion damage pose fundamental challenges to operation of oil and gas infrastructure. In order to manage the life of critical assets, plant operators must implement inspection programs aimed at assessing the severity of wall thickness loss (WTL) in pipelines, vessels, and other structures. Maximum defect depth determines the residual life of these structures and therefore represents one of the key parameters for robust damage mitigation strategies. In this context, continuous monitoring with permanently installed sensors has attracted significant interest and currently is the subject of extensive research worldwide.

Among the different monitoring approaches being considered, significant promise is offered by the combination of guided ultrasonic wave technology with the principles of model based inversion under the paradigm of what is now referred to as guided wave tomography (GWT). Guided waves are attractive because they propagate inside the wall of a structure over a large distance. This can yield significant advantages over conventional pulse-echo thickness gage sensors that provide insufficient area coverage – typically limited to the sensor footprint.

While significant progress has been made in the application of GWT to plate-like structures, extension of these methods to pipes poses a number of fundamental challenges that have prevented the development of sensitive GWT methods. This thesis focuses on these challenges to address the complex guided wave propagation in pipes and to account for parametric uncertainties that are known to affect model based inversion and which are unavoidable in real field applications.

The main contribution of this work is the first demonstration of a sensitive GWT method for accurately mapping the depth of defects in pipes. This is achieved by introducing a novel forward model that can extract information related to damage from the complex waveforms measured by pairs of guided wave transducers mounted on the pipe. An inversion method that iteratively uses the forward model is then developed to form a map of wall thickness for the entire pipe section comprised between two ring arrays of ultrasonic transducers that encircle the pipe.

It is shown that time independent parametric uncertainties relative to the pipe manufacturing tolerances, transducers position, and ultrasonic properties of the material of the pipe can be minimized through a differential approach that is aimed at determining the change in state of the pipe relative to a reference condition. On the other hand, time dependent parametric uncertainties, such as those caused by temperature variations, can be addressed by exploiting the spatial diversity of array measurements and the non-contact nature of electromagnetic acoustic transducers (EMATs).

The range of possible applications of GWT to pipes is investigated through theoretical and numerical studies aimed at developing an understanding of how the performance of GWT varies depending on damage morphology, pipe geometry, and array configuration.

Acknowledgments

Working at the Ultrasonic Imaging Laboratory (USIL) over the course of my time at the University of Cincinnati has provided an environment rich with challenging research opportunities. I give my sincere thanks to my advisor, and the director of USIL, Dr. Francesco Simonetti who never failed to spur on a deeper understanding of topics through practical investigations. In addition, it is necessary to thank my colleagues from USIL who were always ready to provide some new insight on concepts that seemed to momentarily elude my grasp.

I would like to thank my parents, Donald and Devon Willey, as well as grandparents, Byron and Patricia Poindexter, and Frank and Doris Willey. They helped me to understand the value of an education early on, and always found interesting ways to motivate in me the pursuit of high aspirations.

Most of all I am grateful for the support of Katie, who has gracefully endured my musings on a range of engineering topics and mathematical concepts.

Contents

Abstract **i**

Acknowledgments **iv**

Contents **v**

List of Tables **viii**

List of Figures **ix**

Nomenclature **xx**

1 Introduction **1**

1.1 Motivation 1

1.1.1 High Resolution GWT 10

1.1.2 Parametric Uncertainties 11

1.1.3 New criterion for accuracy of GWT 12

1.1.4 GWT performance study 12

1.2 Outline 13

2 Guided waves **15**

2.1 Guided waves in plates 19

2.1.1 Shear horizontal waves 19

2.1.2 Lamb waves . . . 24
2.2 Guided waves in pipes . . . 27
2.2.1 Axial guided waves . . . 28
2.2.2 Circumferential guided waves . . . 34
2.3 Mode selection for GWT . . . 35
2.4 Summary . . . 39

3 Theory of high resolution GWT in pipes 41
3.1 Theory . . . 41
3.1.1 Forward model . . . 41
3.1.2 Virtual arrays . . . 47
3.1.3 Inversion . . . 49
3.2 Numerical example . . . 56
3.3 Conclusion . . . 60

4 Parametric Uncertainties 62
4.1 Experimental setup . . . 62
4.2 Mitigation of TIPU . . . 65
4.3 Signal pre-processing and temperature TDPU compensation . . . 66
4.3.1 Traveltime estimation . . . 66
4.3.2 Temperature compensation . . . 69
4.4 Experimental depth reconstructions . . . 72
4.5 Discussion of EMATs . . . 75
4.6 Conclusion . . . 77

5 On the accuracy of wave speed reconstructions below the resolution scale of ray tomography 78
5.1 Introduction . . . 79
5.2 The encoding of information in pulse traveltimes . . . 83

5.3 Validity of the ray model beyond $\sqrt{\lambda L}$ 88
5.3.1 Cylindrical inclusions 89
5.3.2 Complex media 96
5.4 Tomographic reconstructions 99
5.5 Conclusions 102

6 Performance analysis of GWT **107**
6.1 Introduction 107
6.2 Study of GWT problem parameters 110
6.2.1 Effect of pipe parameters 111
6.2.2 Effect of defect parameters 113
6.2.3 Effect of array parameters 116
6.3 Conclusions 122

7 Conclusions **124**
7.1 Review 124
7.2 Main findings 126
7.3 Avenues of future research 128

List of Publications **130**

Bibliography **132**

A Definition of the inhomogeneous region **143**

List of Tables

3.1 Nominal and reconstructed defect depths for different numbers of replicas. . 56

5.1 Upper and lower contrast bounds for different cylinder diameters relative to the width of the first Fresnel zone as predicted by the criterion in Eq. (5.13). 94

6.1 Wavelength, λ, and nominal thickness, t, for each pipe. 112

6.2 Fresnel zone widths, $\sqrt{\lambda L_{avg}}$, for each pipe, and separation. 120

6.3 L_{avg}, for each pipe, and separation. 120

A.1 Factors of Eq. (A.1), noted as Q_{mk}. 144

List of Figures

1.1 A schematic of a pipe, and defect with symbolic dimensions is shown. Tx and Rx refer to the transmitter and receiver ring arrays. 6

1.2 Three examples of wave propagation are shown, where the green star is a transmitter, the red hexagon is a receiver, and the white circles are point scatterers. Examples of linear scattering are shown in (a) and (b) for different scatterer positions, where the dark arcs represent the transmitted waves, and the light arcs represent the scattered waves. In (c) both scatterers are shown producing the same scattered waves due to the transmitted wave as in (a) and (b), but also secondary scattered waves (the dotted arcs) due to multiple scattering between them. 8

2.1 A section of fiber optic cable is shown. The multiple reflections in the core result in the generation of a guided wave. 16

2.2 An example of SH guided wave propagation in an infinite plate is shown. The dotted plane is the mid-surface of the plate, in which a slice of the displacement distribution is shown. The reflected S waves propagation directions are shown as u_y^+ and u_y^-, and the SH direction is shown as c_{ph}. 20

2.3 The mode shapes of SH_1 and SH_2 are shown in (a) and (b) respectively at a frequency-thickness product of 5 MHz-mm in a steel plate 1 mm thick. These have been normalized by power flow in the direction of guided wave propagation. 23

2.4 The phase velocity (a) and group velocity (b) dispersion curves of SH waves in a steel plate are shown. The red curves refer to the symmetric modes, and blue curves refer to the antisymmetric modes. In both cases, the subscripts refer to the mode order n. 24

2.5 The phase velocity (a) and group velocity (b) dispersion curves of Lamb waves in a steel plate are shown. The red curves refer to the symmetric (S_n) modes, and blue curves refer to the antisymmetric (A_n) modes. The subscripts n refers to the mode order. 26

2.6 The mode shapes of A_0 and S_0 are shown in (a) and (b) respectively at a frequency-thickness product of 1.4 MHz-mm in a steel plate 1 mm thick. These have been normalized by power flow in the direction of guided wave propagation. 27

2.7 A section of pipe is shown with a representation of an axial guided wave propagating along the z direction of the cylindrical coordinate system. 28

2.8 The mode shapes of $T(0,2)$ and $T(0,3)$ are shown in (a) and (b) respectively at a frequency-thickness product of 5 MHz-mm in a steel pipe with 10 mm inner radius and 1 mm wall thickness. These have been normalized by power flow in the direction of guided wave propagation. 29

2.9 The phase velocity (a) and group velocity (b) dispersion curves of $T(0,q)$ in a steel pipe with 10 mm inner radius and 1 mm wall thickness are shown. The red curves refer to the symmetric modes, and blue curves refer to the antisymmetric modes. 30

2.10 The mode shapes of $L(0,1)$ and $L(0,2)$ are shown in (a) and (b) respectively at a frequency-thickness product of 1.4 MHz-mm in a steel pipe with 10 mm inner radius and 1 mm wall thickness. These have been normalized by power flow in the direction of guided wave propagation. 31

2.11 The phase velocity (a) and group velocity (b) dispersion curves of L$(0, q)$ in a steel pipe with 10 mm inner radius and 1 mm wall thickness are shown. The red and blue curves refer to the symmetric and antisymmetric modes respectively. 31

2.12 The mode shapes of F$(1, 1)$ and F$(1, 3)$ are shown in (a) and (b) respectively at a frequency-thickness product of 1.4 MHz-mm in a steel pipe with 10 mm inner radius and 1 mm wall thickness. These have been normalized by power flow in the direction of guided wave propagation. 32

2.13 The phase velocity (a) and group velocity (b) dispersion curves of F$(1, q)$ in a steel pipe with 10 mm inner radius and 1 mm wall thickness are shown for $q = \{1, 2, 3\}$. The L$(0, 1)$, T$(0, 1)$, and L$(0, 2)$ dispersion curves are also shown for comparison. 32

2.14 A section of pipe is shown with a representation of a circumferential guided wave propagating in the β direction of the cylindrical coordinate system. . . 34

2.15 The fundamental flexural (A_0) and extensional (S_0) phase velocity and group velocity dispersion curves of Lamb waves in a steel plate are shown. The large black dot shows the maximum of the A_0 group velocity. The dotted black vertical line shows that the maximum occurs at $f \cdot d \approx 1.4$ MHz-mm, which is termed the CGV point. 36

2.16 The effect of dispersion on a three-cycle Hann-windowed A_0 wave pulse with 160 kHz center frequency that has propagated 400 mm is shown in plates of different thicknesses. Because each of the frequency-thickness products shown are near the CGV point, the envelope of the pulse is relatively stable for different plate thicknesses. 38

2.17 The fundamental flexural (A_0) and extensional (S_0) attenuation dispersion curves of Lamb waves in a 1 mm thick steel plate bounded by a water half space above, and vacuum half space below are shown. In the region near the CGV point ($f \cdot d \approx 1.4$ MHz-mm) the attenuation of A_0 is significantly higher than that of S_0. 39

3.1 Coordinate systems used to form the parameterization of a circular cylinder. (a) 3-D physical space; (b) 2-D acoustic domain. 42

3.2 Replication method used to describe wave-paths wrapping around a pipe. (a) 3-D physical model showing the position of a point source (T) and receiver (R) and the corresponding first three wave-paths Γ_0, Γ_1, and Γ_{-1}; (b) Extended acoustic domain Ω_∞ showing the dependence of $\mathbf{r}'_n$ on $\mathbf{r}'$ for the first two replicas; (c) Acoustic wave-paths corresponding to the guided wave-path on the surface σ. 45

3.3 Block structure of the information matrix. The sub-matrices have dimension $N \times N$ and correspond to different combinations of the sub-apertures of the transmit and receive virtual arrays. 48

3.4 Block diagram of the iterative algorithm used to solve the inverse problem. . 53

3.5 Model used for the numerical simulations. (a) WTL map; % values indicate wall loss relative to thickness; (b) Phase velocity model containing two replicas; % value indicate the phase velocity contrast. The red and black dots represent the position of the transducers of the transmit and receive arrays. . 56

3.6 Simulated time delay matrix from the acoustic model in Fig. 3.5. 57

3.7 Examples of reconstructed WTL map at different steps of the iterative inversion: (a) At the end of the first step; (b) End of the third step; (c) End of iteration. 59

3.8 Benefit of higher-order helical modes. WTL maps obtained: (a) Using up to the second order helical modes; (b) Up to the first order; (c) Only considering the direct wave-paths. 60

4.1 Experimental setup: (a) An 8" diameter pipe is instrumented with two ring arrays each containing 16 EMAT transducers; (b) Detail of the defect consisting of a deeper region pointed by the arrow and smooth transition zone starting along the contour indicated by the star arrow. 63

4.2 Temperature control setup: (a) The heater consists of four strands of heat tape wrapped helically around a 90 mm diameter, 2000 mm length steel pipe; (b) The insulated pipe/transducer setup is shown. 64

4.3 Waveforms measured across the transducers of the receive array when source # 6 radiates. The source is aligned with the defect and its effect on the transmitted signals is most evident among the direct arrivals measured with receivers # 5-6. (Red waveforms) baseline signals; (blue waveforms) current signals; (black curves) predicted group traveltimes for different helical paths. 67

4.4 Effect of temperature on the measured waveforms when source #6 radiates. (a) Current signals measured at 126°C; (b) Current signals measured at room temperature. In both cases the baseline (red waveforms) is measured at room temperature. 70

4.5 Temperature compensation of experimental data: (a) Traveltime delay matrix obtained when the temperature differential between current and baseline measurements is 100°C; (b) Traveltime delay matrix after temperature compensation; (c) Traveltime delay matrix obtained under stable temperature conditions — current and baseline measurements are performed both at room temperature. Note the color scale of the uncompensated matrix is different from the others. 72

4.6 WTL maps reconstructed from the experimental data. The maps are obtained by considering up to the second order modes (first column), first order (second column) and direct wave-paths only (third column). The first row uses the data in Fig. 4.5(c) which was measured under stable temperature conditions while the second row is obtained from the temperature compensated data in Fig. 4.5(b). The estimated values of maximum depth are indicated in each image. 73

4.7 Maximum depth monitoring: (a) The pipe is exposed to normal room temperature variations; (b) An internal heater is used to increase the pipe temperature up to 175°C. The horizontal lines indicate the nominal depth measured with a fingertip ultrasonic probe. 74

4.8 Long term monitoring of EMAT transducers under thermal cycling: (a) Applied thermal cycles; (b) True phase; (c) Normalized amplitude. 76

5.1 Illustration of the effect of pulse distortion on traveltime estimations: (a) when a pulse undergoes a rigid translation traveltime can be estimated by tracking any point in the pulse; (b) due to distortion it is no longer possible to track the same pulse point leading to ambiguity in traveltime estimations. 84

5.2 Illustration of the role of the sensitivity kernel width, $\sqrt{\lambda L}$, on the resolution of ray tomography and the wavefront healing phenomenon. (a) A uniform sound speed perturbation of size $\delta l < \sqrt{\lambda L}$ occupies a small portion of the kernel volume causing a small change in traveltime and making it dependent on the sound speed contrast in the direction transversal to the ray; (b) A perturbation with $\delta l > \sqrt{\lambda L}$ leads to a traveltime that is only dependent on the sound speed contrast along the ray consistently with ray theory; (c) Increasing the distance of the receiver from the source widens the kernel causing the sound speed perturbation to become increasing smaller relative to the kernel and hence weakening the effect of the perturbation on traveltime. 86

5.3 Transformation of signal function with center frequency of 160 kHz, $s(t)$ (a) into the instantaneous frequency function (b). The black horizontal line shown in (b) corresponds to the threshold associated with the picked traveltime. . . 89

5.4 Normalized traveltime shifts predicted by the eikonal equation for a homogeneous cylinder immersed in a homogeneous background. The traveltimes are computed for different values of the sound speed contrast μ and for a range of cylinder diameter to width of the sensitivity kernel ratios, d/w. The markers indicated the eikonal predictions while the curves correspond to the analytical expressions given in the text. 90

5.5 Diagram illustrating the refracted and diffracted wave paths observed when a cylinder is placed half way between a source S and a receiver R. 91

5.6 Full wave simulation of scattering by a slow cylinder ($\mu = -40\%$) of diameter equal to the width of the sensitivity kernel. (a) diagram showing the position of the cylinder relative to the source and 15 receivers, (b) waveforms measured by the 15 receivers, (c)-(f) snapshots of the wavefield over the rectangular area around the cylinder shown in (a). 92

5.7 Traveltime shifts estimated from full wave simulations using the IF method (a) and the cross-correlation method (b) as a function of contrast, μ, and cylinder diameter to width of the sensitivity kernel ratios, d/w. Note that the vertical scale of (b) is different from that of (a). 93

5.8 Example of defocusing occurring in the presence of positive contrast for a cylinder diameter equal to the width of the sensitivity kernel. The cylinder is centered between a point source and a receiver that are 400λ apart. (gray) baseline signals without the cylinder; (black) signals detected in the presence of the cylinder. 96

5.9 Inhomogeneous contrast maps. Map (a) is antisymmetric relative to the $x = 0$ axis and is then modified by adding a cylindrical inclusion of diameter $d = w/8$ with contrast varying from 10% (b) to 100% (c). The ray paths from the source to the receive array are shown for the different contrast levels of the cylinder. Note that the source and receive array are far from the edges of domain shown in the figure. 97

5.10 Through-transmission signals for the antisymmetric inhomogeneous medium of Fig. 5.9(a). (gray) signal propagated through the homogeneous background; (black) signal through inhomogeneous region. 97

5.11 Traveltimes shifts measured along the aperture of the receive array for the inhomogeneous models shown in Fig. 5.9. Six different contrast levels of the cylindrical inclusion are simulated: 10, 20, 40, 60, 80 and 100% with the increasing contrast direction being pointed by the arrows. (a) compare the eikonal and IF traveltimes while (b) the eikonal and cross-correlation traveltimes. 98

5.12 Reconstructed minimum contrast versus the nominal contrast of a uniform cylinder for three different cylinder diameter to sensitivity kernel width (d/w) ratios. The absolute values of the negative contrast are shown. The solid line corresponds to $\mu_r = \mu_0$. 100

5.13 Maximum contrast of cylindrical inclusions reconstructed with curved ray tomography (CRT) as a function of nominal contrast. CRT is applied to traveltime data obtained with the eikonal model and from full wave simulations though the IF and cross correlation methods. Different cylinder diameters, d, relative to the width of the sensitivity kernel, w, are considered: (a) d/w=0.25; (b) d/w=0.5; (c) d/w=1. 101

5.14 Reconstructed contrast profiles corresponding to the data shown in Fig. 5.13. The columns correspond to d/w =0.25, 0.50 and 1.00, while the rows correspond to contrast levels of 10, 20, 40, 60, 80 and 100% from top to bottom. (black solid lines) true contrast profile, (gray curves) CRT applied to eikonal data, (dash-dot curves) CRT applied to IF data obtained from full wave simulations, (dashed curves) CRT applied to cross-correlation data. 105

5.15 Reconstructed maximum contrast for a cylindrical inclusion of diameter d/w=0.25 at the center of the inhomogeneous model of Fig. 5.9(a) as a function of the cylinder nominal contrast. CRT is applied to traveltime data obtained with the eikonal model and from full wave simulations though the IF and cross correlation methods. 106

5.16 Reconstructed contrast profiles along the $y = 0$ axis for the inhomogeneous medium of Fig. 5.9 and for different values of the contrast of the cylindrical inclusion. (black solid lines) true contrast profile, (gray curves) CRT applied to eikonal data, (dash-dot curves) CRT applied to IF data obtained from full wave simulations, (dashed curves) CRT applied to cross-correlation data. . . 106

6.1 Absolute value of the A_0 Lamb wave phase velocity contrast, μ, given the nominal phase velocity coincides with the CGV point (i.e. $f \cdot t = 1.4$ MHz-mm), in terms of normalized defect depth, δ/t. 109

6.2 Schematic of pipe with arrays and defect profile. 110

6.3 Performance characterized as the agreement between the nominal defect depth, δ_o, and reconstructed δ_r. The level of gray moves from dark to light for increasing defect width: w = 1/4, 1/2, 1, 2 multiples of $\sqrt{\lambda L_{avg}}$. The marker faces ($\times$, $\circ$, $\triangle$) correspond to the array separation: $L = 2D$, $3D$, $4D$. Data for 8" schedule 40 (a), 8" schedule 120 (b), and 16" schedule 40 (c) are shown. The black line represents perfect performance where $\delta_r = \delta_o$. 111

6.4 Performance characterized as the agreement between the nominal defect depth, δ_o, shown as the horizontal grid lines, and reconstructed, δ_r. The level of gray moves from dark to light for increasing defect depth: $\delta = 5$, 10, 20, 30, 50, and 80% of wall thickness. The marker type ($\times$, $\circ$, $\triangle$) correspond to the array separation: $L = 2D$, $3D$, $4D$. Data is the same as that shown in Fig. 6.3. The black line corresponds to the δ_{cr} criterion. 114

6.5 Performance characterized as the absolute value of error, $|e|$, as a function of normalized defect width, w/L_{avg}, for defects outside of (a), and within (b) the δ_{cr} curve shown in Fig. 6.4. The level of gray moves from dark to light for increasing defect depth: $\delta = 5$, 10, 20, 30, 50, and 80% of wall thickness. The solid curves in (a) are the analytical error curves calculated using the critical defect depth, shown in Fig. 6.4, substituted into the δ_r term in Eq. 6.1 for each nominal defect depth, δ_o. The marker type ($\times$, $\circ$, $\triangle$) correspond to the array separation: $L = 2D$, $3D$, $4D$. 115

6.6 Performance characterized as signed error, e, in terms of array separation, L for all defect width and depth combinations within the δ_{cr} curve. The error for each L, is represented by the average error (dark gray dot), standard deviation error bars (light gray bars extending vertically from the average error), plotted over box plots (black) characterizing the spread of the data. The 8" schedule 40 (a), 8" schedule 120 (b), and 16" schedule 40 pipe results are shown. 117

6.7 Performance characterized as signed error, e, in terms of normalized defect width, w/L_{avg}, for all defect width and depth combinations within the δ_{cr} curve. The marker type ($\times$, $\circ$, $\triangle$) correspond to the 8" schedule 40, 8" schedule 120, and 16" schedule 40 pipe results. The level of gray moves from dark to light for increasing defect depth consistent with Fig. 6.5. The solid black line and dotted black lines correspond to the fitted error curve, and nonsimultaneous prediction bounds (based on 95% confidence interval). The array separations, $L = 2D$, $3D$, $4D$, are shown in (a)-(c) respectively. 117

6.8 Performance characterized as signed error, e, in terms of normalized defect width, w/L_{avg}, for all defect width and depth combinations within the δ_{cr} limit. The marker type ($\times$, $\circ$, $\triangle$) correspond to the 8" schedule 40, 8" schedule 120, and 16" schedule 40 pipe results. The level of gray moves from dark to light for increasing defect depth consistent with Fig. 6.5. The solid black line and dotted black lines correspond to the fitted error curve, and nonsimultaneous prediction bounds (based on 95% confidence interval). This figure combines all data from Fig. 6.7. 119

6.9 Performance characterized as signed error, e, in terms of number of transducers, N, for all defect width and depth combinations within the δ_{cr} limit. The error for each N, is represented by the average error (dark gray dot), standard deviation error bars (light gray bars extending from the average error), plotted over box plots (plotted in black) characterizing the spread of the data. Each column corresponds to the type of pipe: 8" schedule 40, 8" schedule 120, 16" schedule 40 moving left to right. Each row corresponds to the array separation: $L = 2D$, $3D$, $4D$ moving top to bottom. 121

Nomenclature

Chapter 1

δ	Defect depth
λ	Wavelength
C	Carbon
D	Separation of ring arrays
d	Pipe wall thickness
D_o	Diameter of pipe
e	electron
Fe	Iron
H	Hydrogen
N	Number of transmitter/receiver elements per array
O	Oxygen
S	Sulfur
w	Defect width
$^+$	Superscript indicating positive charge

$^-$ Superscript indicating negative charge

Chapter 2

$\mathbf{\Psi}$ Vector potential

$\mathbf{a}$ Arbitrary amplitude vector

$\mathbf{D}$ Directional component matrix

$\mathbf{f}$ Body force vector field

$\mathbf{u}$ Displacement vector field

$\ddot{\mathbf{u}}$ Acceleration vector field

λ' First Lamé constant

μ' Second Lamé constant

∇ Gradient operator

∇^2 Laplacian

ν Poisson's ratio

ω Angular frequency

ϕ Scalar potential

ρ Material density

σ stress

θ Angle of wave propagation relative to a surface normal

θ_i Angle of incidence

θ_r Angle of reflection

θ_t Angle of transmission

A Arbitrary scalar amplitude

c Generic wave speed

c_L Longitudinal wave speed

c_S Shear wave speed

c_{gr} Guided wave group velocity

c_{ph} Guided wave phase velocity

d thickness

E Young's modulus

f Frequency

k Wavenumber

$k_\circ$ Circular wavenumber, in direction of circumferential guided waves

$k_\parallel$ Wavenumber component in the direction of guided wave propagation

$k_{\perp L}$ Longitudinal perpendicular wavenumber component

$k_{\perp S}$ Shear perpendicular wavenumber component

$k_\perp$ Wavenumber component perpendicular to the direction of guided wave propagation

$m_r(r), m_\beta(r), m_z(r)$ Guided wave mode shapes in the pipe

$m_x(z), m_y(z), m_z(z)$ Guided wave mode shapes in the plate

n Order of guided modes in plates

p Circumferential order of guided waves in pipes

q Radial order of guided waves in pipes

r, β, z Cylindrical coordinates

t Time

u_r, u_β, u_z Components of the cylindrical displacement vector field

u_x, u_y, u_z Components of the Cartesian displacement vector field

x, y, z Cartesian coordinates

$\boldsymbol{\sigma}$ Traction vector

$^+$ Superscript of stress or displacement resulting from an up reflecting wave

$^-$ Superscript of stress or displacement resulting from a down reflecting wave

^{b} Superscript of displacement or stress interacting with the bottom surface of a plate

^{i} Superscript of displacement or stress interacting with the inner surface of a pipe

^{o} Superscript of displacement or stress interacting with the outer surface of a pipe

^{t} Superscript of displacement or stress interacting with the top surface of a plate

Chapter 3

$'$ Superscript indicating a two dimensional counterpart of a three dimensional variable

α_k Step size of the conjugate gradient method from line search

β_k Conjugate gradient update parameter

$\boldsymbol{\delta}_k$ Descent direction of the conjugate gradient method

$\boldsymbol{\phi}$ Discrete representation of ϕ

$\boldsymbol{\tau}$ Discrete representation of τ

$\delta\mathbf{u}$ Residual

Γ Ray path curve

γ Regularization parameter

Γ_R Closed curve representing the receiver array

Γ_T Closed curve representing the transmitter array

$\mathbb{U}$ Information matrix

$\mathcal{D}$ Regularization weighting operator

∇ Gradient operator

∇^2 Laplacian

Ω Two dimensional representation of σ

Ω_∞ Extension of Ω by repeating the domain in $\hat{\mathbf{x}}'$

Ω_e Extension of Ω by repeating the domain in $\hat{\mathbf{x}}'$ m times

ϕ Scalar potential

Σ Surface of cylinder

σ Surface of cylinder between arrays

τ Traveltime

$\hat{\mathbf{x}}'$ Unit vector parallel to the x'-axis

$\mathbf{F}$ Forward model operator

$\mathbf{f}$ Vector representing point sources

$\mathbf{G}_e$ Matrix of ray length segments

$\mathbf{G}_H$ Matrix of approximate Green's functions

$\mathbf{o}$ Object function vector

$\mathbf{r}$ Position vector of point P

$\mathbf{u}_m$ Information matrix $\mathbb{U}$ rearranged as a vector

$\mathbf{u}_s$ Synthetic data vector

P Point on the surface of the cylinder

$\{O, x, y, z\}$ Three dimensional Cartesian coordinates

a Average path length between transmitters and receivers

c Generic wave speed

c_0 Background velocity

c_{ph} Guided wave phase velocity

d Pipe wall thickness

d_0 Reference pipe wall thickness

$E(\mathbf{o})$ Cost function

f Frequency

H Length of pipe section

i Virtual array transmitter index

j Virtual array receiver index

k Iteration index of conjugate gradient method

k_0 Background wavenumber

L Length of transmitter/receiver array curve

l Number of nodes in the discrete representation of τ, or ϕ fields

m Highest order of helical mode considered

N Number of transmitters/receivers

O_e Object function with respect to the eikonal equation

O_H Object function with respect to the Helmholtz equation

p Receiver index

q Transmitter index

R Receiver point

r Average pipe radius across the wall thickness

T Transmitter point

* Complex conjugate

^{T} Matrix transpose

$_n$ Subscript indicating the replica of Ω a point belongs to

Chapter 4

Δc Phase velocity change due to temperature difference

$\delta \mathbf{u}'$ Residual based on differential measurements

$\Delta \mathbf{u}_m$ Differential measurement

$\hat{\mathbf{u}}_m$ The portion of the measured data vector free of parametric uncertainties

$\mathbb{U}$ Information matrix

τ Traveltime

τ^b Matrix of phase traveltimes from baseline measurements

τ^c Matrix of phase traveltimes from current measurements

$\mathbf{u}$ Dataset vector

$\mathbf{u}_T$ The portion of the measured data vector caused by parametric uncertainties

Θ_b Temperature at time of baseline signal acquisition

Θ_c Temperature at time of current signal acquisition

$C(\Delta c)$ Temperature compensation cost function

c^b Phase velocity at the temperature of the baseline measurements

c_{gr} Guided wave group velocity

c_{ph} Guided wave phase velocity

D Distance between virtual transmitter and receiver

d Thickness

f Frequency

i Virtual array transmitter index

j Virtual array receiver index

m Highest order of helical mode considered

N Number of transmitters/receivers

n Indicates the sub-aperture of the virtual array

$s_{ji}(t)$ Signal measured at the j-th receiver, excited by the i-th transmitter

^{b} Superscript indicating baseline data

^{c} Superscript indicating current data

$_m$ Subscript indicating measured data

$_s$ Subscript indicating synthetic data

Chapter 5

$\delta\Omega$ Volume of uniform sound speed perturbation

δc Velocity perturbation

δl Size of uniform sound speed perturbation

Δ Circular array diameter

$\delta\tau$ Traveltime shift

Γ Path linking the source and receiver

λ Wavelength

μ Wave speed contrast

∇^2 Laplacian

Ω Three dimensional volume

τ Traveltime field

$\mathbf{r}$ Receiver point defined as (r_1, r_2, r_3)

$\mathbf{s}$ Source point defined as (s_1, s_2, s_3)

$\mathbf{x}$ General point defined as (x_1, x_2, x_3)

$\{O, x_1, x_2, x_3\}$ Cartesian coordinates

c	wave speed field
c_0	reference wave speed
D	Characteristic size of the contrast support
d	Characteristic size of the contrast support normalized by λ
F	Acoustic source
f	Frequency
$h(t)$	Hilbert transform of signal function
K	Sensitivity kernel
L	Distance between a source and receiver
l	Distance between a source and receiver normalized by λ
M	Number of receivers
N	Number of sources
P	Pressure field
P_R	Receiver point
P_S	Source point
$s(t)$	Signal function
T	Period
W	Sensitivity kernel width
w	Sensitivity kernel width normalized by λ
$_0$	Nominal contrast subscript

$_{CC}$ Subscript of traveltime shift detected by cross correlation

$_{cr}$ Critical contrast subscript

$_{D}$ Traveltime shift subscript of diffracted ray path

$_{IF}$ Subscript of traveltime shift detected by instantaneous frequency

$_{R}$ Traveltime shift subscript of refracted ray path

$_{r}$ Reconstructed contrast subscript

Chapter 6

δ Defect depth

$\hat{e}$ Estimate of error determined by regression

μ Wave speed contrast

a, b Regression model parameters

D Pipe diameter

e Error in reconstructed defect depth relative to pipe wall thickness

f Frequency

L Separation of ring arrays

N Number of elements per transmitter/receiver array

t Pipe wall thickness

w Defect width

L_{avg} Average distance between transmitters and receivers

$_{cr}$ Subscript indicating critical contrast or defect depth

$_o$ Subscript indicating nominal defect depth

$_r$ Subscript indicating reconstructed defect depth

Appendix A

Q_{mk} Matrix of weighting factors

μ Wave speed contrast

g Masked weighted sum of Bessel functions

J_2 Bessel function of the first kind and order two

p Weighted sum of Bessel functions

W Sensitivity kernel width

x_1, x_2 Two dimensional Cartesian coordinates

z_m Zeros of Bessel function of the first kind and order two

Chapter 1

Introduction

1.1 Motivation

Globally, oil production has increased over the past few years to its highest historical levels. Current projections are that the production will increase by approximately 17.6 million barrels per day by 2020 [1]. This leads to a total global production of more than 100 million barrels per day. A main contributor to this increase is the production from the tight oil and shale oil fields of the United States. The projected increase will put the United States as the second largest oil producing nation by 2020 [2]. In addition, the United States is uniquely positioned to make use of the oil shale formations due to the number of oil drilling rigs that are equipped to perform horizontal drilling (95% of rigs are equipped), as well as a number of small companies that are willing to explore the possibility of harvesting oil from these geological formations [1, 2].

Shale oil is produced using a multistage process that unlocks the oil from the oil shale geological formations. Shale oil recovery consists of drilling a vertical shaft through the overburden (the geological formation covering the oil shale formation) which will eventually provide an escape for the gas produced as well as contain a pipe string that will convey the oil up from the horizontal shaft that is formed along the bottom of the shale bed.

After these shafts have been drilled, the oil shale has to be broken up somehow in order to create passages for the flow of oil out of the oil shale. This can be achieved by rubblization (explosives placed in the oil shale via drilled passages), or hydraulic fracturing. Once the shale has been broken up, heat must be applied to the oil shale. This heat can be supplied in situ by burning a small amount of the shale oil/some auxiliary fuel, or using controlled radio frequency fields in much the same way as a microwave to release the shale oil in a process known as retorting [3–5]. Heat could be supplied ex situ as well. When oil shale is retorted (heated to 600 – 900 °F in the absence of significant amounts of oxygen) pyrolysis takes place. Pyrolysis is the process of destructively distilling kerogen to form, oil, gas, coke, and water [4, 5].

Green River oil shale is physically composed of 80.5% Carbon, 10.3% Hydrogen, 2.4% Nitrogen, 1% Sulfur and 5.8% Oxygen, as well as minerals, such as, Carbonates, Feldspars, Quartz, Clays, Analcite and Pyrite [5]. This leads to the shale oil containing oxygen, nitrogen, sulfur, and metallic compounds, as well as, emulsified water and suspended solids [6]. The presence of these components has traditionally necessitated the upgrading (further processing to reduce the amount of oxygen/nitrogen/sulfur) of the shale oil before transportation [7].

After upgrading, the shale oil is stored in tanks until it can be transported to either a refinery to be used as feedstock, or some process where it will be directly used as fuel. Transportation of shale oil is achieved via train, ship, truck or pipeline [8]. The oil pipelines used are generally carbon steel. Transportation pipelines can be many miles in length between an input and output port [9].

Due to the chemical compounds present in shale oil corrosion of the pipelines becomes significant. Corrosion refers to the degradation of a structure via transformation of its chemical makeup. In the case of steel, oxidation (anodic reaction) occurs when an iron atom loses electrons [10], via

$$Fe \rightarrow Fe^{2+} + 2e^{-}. \tag{1.1}$$

This happens at the grain boundaries in the steel when exposed to an aqueous electrolyte, as this is where the steel is most reactive. The grain boundaries are also the site of the reduction (cathodic reaction) which consumes the electrons created by the oxidation. The simultaneous anodic and cathodic reactions in the presence of an aqueous electrolyte form the electrochemical cell (triangle of corrosion) [10–14]. Oil and gas pipelines contain carbon dioxide, hydrogen sulfide, organic acids, bacteria, sand and water which will react to the oxidation of the iron by forming many different types of corrosion [10, 14]. Two common types are sweet corrosion, given by

$$CO_2 + H_2O + Fe \rightarrow FeCO_3 + H_2, \tag{1.2}$$

and sour corrosion given by

$$H_2S + H_2O + Fe \rightarrow FeS_x + 2H + H_2O, \tag{1.3}$$

where FeS_x represents a range of iron sulfides. This corrosive action causes a thickness loss of the carbon steel structures used for transporting the shale oil, such as pipelines or tanks.

Pipelines carrying water alone experience wall thickness loss (WTL) rates of less than 1 mm/y [13]. The corrosion product will usually form a protective film over the steel. This will effectively block further corrosion, via separating the anode from the electrolyte. However, material loss can also come from the action of suspended solids eroding the inner surface of the pipe walls. The WTL in pipelines is enhanced via the synergistic action of erosion and corrosion (erosion-corrosion) [13]. Erosion-corrosion increases the WTL because the corrosion product is more easily eroded, and once the corrosion product is eroded, this exposes the base material to be further corroded. Pipelines carrying erosive-corrosive slurry can yield WTL rates of approximately 10 mm/y, or 27.4 μm/day [13].

Erosion-corrosion WTL increases the stress in the pipe wall from the pressure load used to transmit the oil as well as the weight of the structure, leading to failure [15]. Indeed, it is

estimated that the yearly cost of erosion-corrosion across all industries is somewhere between 4% and 6% of the gross domestic product of the United States [11–13]. There have been many recent cases of oil pipeline failure due to corrosion, such as the March 2006 incident in Alaska in which 200,000 gallons of oil were spilled [16]. This instance led to a long court battle and ultimately, the responsible company had to pay a US$20,000,000 fine to settle criminal charges. In addition to this being costly, it is also devastating to the environment and the general population.

This sort of catastrophic failure has necessitated the development of corrosion mitigation strategies. The main strategies available for corrosion planning are cathodic/anodic protection, material selection, chemical dosing and the application of internal and external coatings [10]. However, only chemical dosing and coatings are useful for internal corrosion mitigation [10]. These strategies require as an input some type of evaluation of the pipeline WTL rates in order to properly select a suitable combination of mitigation strategies. One type of analysis used is based on the statistical fatigue/failure analysis for the estimation of the structure's useful lifetime [17] which is based on sampling the current wall thickness at a few, statistically significant, locations along the pipeline. The effectiveness of this approach relies on accurate and quasi-real time measurements of the wall thickness at selected locations. As mentioned earlier, the WTL rate of 27.4 μm/day would be the theoretical average amount of sensitivity needed to monitor the corrosion-erosion caused by slurry, such as shale oil [13], on a daily basis. This is made even more difficult due to the fact that the tolerance of pipe wall manufacture is generally greater than this amount (ASTM standard A106 dictates that the wall thickness tolerance lower bound is 87.5% nominal wall thickness) [18].

Ultrasonic nondestructive evaluation provides several methods for evaluating the WTL rate that could give the desired accuracy, but would be prohibitively expensive due to the cost of access. The cost to inspect one meter of pipe can be as high as US$2,000-US$5,000 due to the difficulty of access. Scenarios of difficult pipeline access include: the assembly of scaffolding to inspect high segments, underwater access of subsea segments, and the

excavation of buried segments.

To contain the cost of inspections, permanently installed sensors are now being used in a number of industrial applications under the structural health monitoring paradigm. Commercial devices use electrodes welded onto the pipe to inject current according to the potential drop technique [19, 20] or ultrasonic transducers directly bonded, clamped [21] or attached through buffer waveguides to operate at higher temperatures [22]. While these sensors can provide accurate wall thickness estimations, their coverage is limited to the area beneath the transducer which may render the inspection ineffective if the transducer is not positioned at the point of maximum WTL or worse if it misses the damaged area entirely. Moreover, these sensors are not suited for monitoring inaccessible regions such as pipe supports or concrete penetrations.

To increase area coverage, guided ultrasonic waves provide an attractive solution since they can propagate over a large distance from a single transducer position [13]. Indeed, the long-range inspection capabilities of guided waves are now routinely used for the detection of defects in pipelines [23–25]. However, current long-range screening systems cannot provide accurate estimations of defect depth especially in the presence of complex morphologies [26]. On the other hand, the constant group velocity (CGV) method [27, 28] provides a medium range solution, typically over a distance of several pipe diameters, for the estimation of the average WTL between a pair of guided wave transducers arranged in a pitch-catch configuration. While average WTL may be sufficient to assess large and relatively uniform defects, more spatially localized information is needed to estimate the maximum depth of irregular defects.

The possibility of providing spatially localized information with guided waves through the combination of multiple transmission measurements and tomographic techniques was realized in the early 1990s by Hutchins's group [29] and has since received much attention [30–36]. The majority of research works on guided wave tomography (GWT) have focused on flat plate geometries and it has now been demonstrated that highly accurate depth maps can be

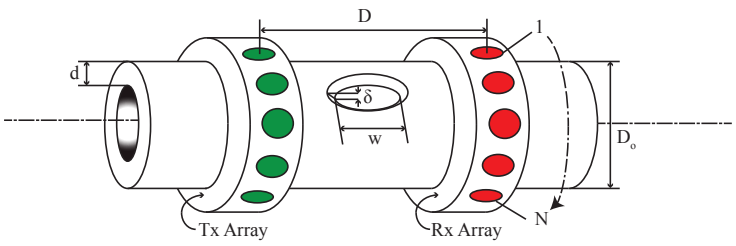

Figure 1.1: A schematic of a pipe, and defect with symbolic dimensions is shown. Tx and Rx refer to the transmitter and receiver ring arrays.

obtained by implementing tomographic algorithms that can take into account refraction and diffraction effects [36]. On the other hand, fewer works have investigated GWT applications to pipes. Here, a pair of transmit- and receive-ring arrays of ultrasonic transducers encircles the pipe and delimits the section to be monitored, as shown in Fig. 1.1. The arrays are used to transmit guided wave signals from any transducer of the transmit array to any transducer of the receive array thus insonifying potential defects from multiple angles. Assuming that the pipe wall thickness is small compared to its radius, GWT can be implemented by ideally unwrapping the section of pipe between the arrays and treating it as a flat plate. The ring arrays therefore transform into two parallel linear arrays and the GWT problem reduces to the classical borehole tomography configuration used for seismic profiling [37]. The borehole configuration leads to what is known as the limited view problem [38,39] since it is not possible to perform transmission measurements at insonification angles approaching the direction parallel to the arrays, i. e. the circumferential direction in the pipe. The missing angles cause image degradation and hence lead to insufficient depth estimation accuracy. Leonard and Hinders [32] and Volker and Bloom [35] suggested that the accuracy of GWT may be improved by exploiting the information contained in higher-order helical modes; however, they did not provide a methodology to do so and the extent of the potential benefits gained from the higher modes remained unclear.

Indeed, a thorough assessment of the potential of GWT for monitoring corrosion rates in real pipelines has not been conducted and very limited information can be found in the

literature that may support the feasibility of this approach. To appreciate the magnitude of the challenges posed by real field applications to GWT it is necessary to consider how GWT yields maps of WTL.

GWT is a model based inversion method that uses a forward model to predict the data that would be produced by the experiment if the input parameters (structure of the waveguide, the geometry of the defects, transducer locations, and any other conditions that might affect the propagation of the wave) are accurately incorporated into the model. In other words, the model is meant to accurately mimic the relevant physics of a wavefield interacting with the media through which it propagates. GWT uses a rule that updates the model's internal definition of the waveguide, specifically the defect geometry, based on the difference between the measured data produced by the physical experiment, and the synthetic data produced by the forward model. The difference between these two data sets is minimized by iteratively updating the model's internal definition of the waveguide and reevaluating the error in the data until no further progress is made in the minimization. This means that theoretically, if all of the input parameters that affect wave propagation can be included in the model accurately, the reconstruction will yield an exact description of the current state of the waveguide.

Due to the use of a forward model within GWT, errors in the input can propagate through the inversion and limit the accuracy of the estimation of the state of the waveguide. These errors in input parameters are termed parametric uncertainties. These can be divided into two groups: time dependent and time independent. One important example of a time dependent parametric uncertainty (TDPU) would be environmental temperature change which causes significant changes in the ultrasonic properties of the waveguide. Temperature variations can cause changes in the propagation characteristics of the waveguide regardless of the occurrence of damage. It is well known that an increase in temperature causes a decreases in Young's modulus [40]. Temperature differentials of 100 °C or even greater are likely in practice since pipelines are typically exposed to extreme weather conditions and variations

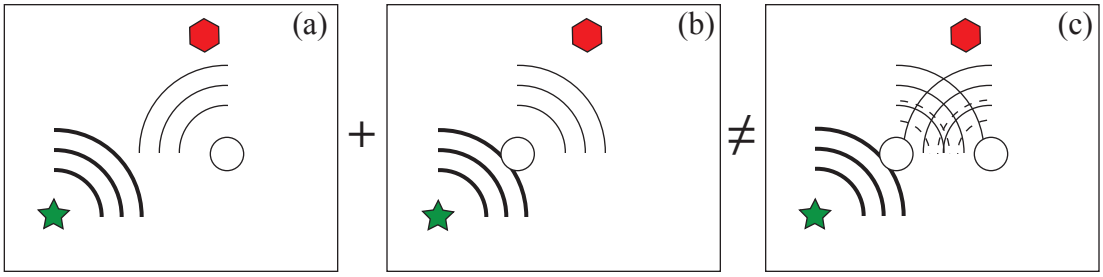

Figure 1.2: Three examples of wave propagation are shown, where the green star is a transmitter, the red hexagon is a receiver, and the white circles are point scatterers. Examples of linear scattering are shown in (a) and (b) for different scatterer positions, where the dark arcs represent the transmitted waves, and the light arcs represent the scattered waves. In (c) both scatterers are shown producing the same scattered waves due to the transmitted wave as in (a) and (b), but also secondary scattered waves (the dotted arcs) due to multiple scattering between them.

in the temperature of the fluid transported in them. Another example of TDPU occurs when the pipe experiences fluid loading during multiphase turbulent flow, or coating degradation, which may affect the extent of energy leakage from the waveguide to the surrounding media.

A source of time independent parameter uncertainty (TIPU) occurs when the geometry of the pipe is not uniform in cross section or wall thickness due to poor manufacturing tolerances, leading to a waveguide with wave propagation characteristics different from those used by the forward model. A second example of TIPU occurs in array element position due to small shifts that may occur in the location of the transducer at the time of the array installation on the surface of the pipe. All of these uncertainties will cause discrepancies between the model predictions and the physical measurement that can affect the convergence of the inversion and lead to significant errors in reconstruction called artifacts. It is therefore essential to provide robust strategies to mitigate the effect of these unavoidable uncertainties.

Besides the parametric uncertainties, another source of complexity results from the nonlinear nature of the inverse problem. While the forward problem describing the propagation and scattering of guided waves can be assumed to be linear, the inverse problem is nonlinear due to the multiple scattering and refraction effects [41]. An example of the difference between linear and multiple scattering is shown in Fig. 1.2. In Fig. 1.2(a) and Fig. 1.2(b)

the point scatterers are shown to produce scattered waves excited by the transmitted wave being incident upon them. Fig. 1.2(c) shows that the waves produced by the scatterers will not only depend on the wave excited by the transmitter but also the multiple scattering between them, which is represented by the secondary scattered wave shown as dotted arcs. This means Fig. 1.2(c) is not a superposition of the linear scattering shown in Fig. 1.2(a) and Fig. 1.2(b).

In some imaging problems the inverse problem can be linearized by adopting simplifications in the forward model such as the Born approximation [42]. The linearization leads to reconstructions which are the convolution of the exact state of the structure with the so-called point spread function (PSF). The PSF can then be used to characterize the performance of the inversion regardless of the properties of the structure being imaged with metrics such as the resolution and contrast. On the other hand, such a general characterization is not possible when the inversion is nonlinear. Therefore, it is necessary to define more specialized metrics applicable to narrower ranges of material and structural properties within the applications of interest.

The aim of this thesis is to undertake an investigation of the theoretical and practical aspects of GWT to address these raised issues. Specifically, this encompasses four main objectives:

- Introduce a framework for high resolution under the limited view offered by the ring arrays mounted on a pipe
- Introduce a method to ameliorate the effects of both time dependent and independent parametric uncertainties
- Introduce a new criterion characterizing the ability of the GWT implementation given in this thesis to produce accurate reconstructions
- Study the attainable performance of GWT for practical monitoring scenarios

The overall approach is based on a combination of theoretical, numerical and experimental tasks. These aims will be laid out in further detail in the following sections.

1.1.1 High Resolution GWT

Central to achieving accurate WTL reconstructions is the availability of a suitable set of ultrasonic signals that encodes all the information required to reconstruct the WTL map within the desired level of accuracy. To obtain all the information of interest, it is important to perform the ultrasonic measurements so that they can yield independent or complementary data whilst minimizing the degree of redundancy. Such a set of measurements will be referred to as a complete dataset.

For a selected guided mode and frequency of operation, which corresponds to a wavelength, λ, the completeness of the dataset depends on the number and spatial locations of the source and receiver transducers. According to the Nyquist criterion, spacing the transducers of the receiver array by less than $\lambda/2$ apart leads to spatial oversampling of the wavefield that results in redundant information. Based on a reciprocity argument, redundant information is also obtained when the sources of the transmit array are spaced less than $\lambda/2$ apart. Therefore, the most effective spatial sampling condition is obtained when the spacing between transducers is $\lambda/2$ which produces the minimum number of transducers required to capture all the information encoded in the wavefield.

Besides the spacing between transducers, ultrasonic signals collected must be excited from a sufficiently diverse set of viewing angles. Ideally, the region of interest should be insonified from every possible angle and each time the resulting wavefield sampled all around the same region. In the absence of noise and parametric uncertainties, this ideal full view configuration would lead to a unique solution to the inverse problem and hence an exact reconstruction of the WTL map.

For GWT applications, the spatial sampling along the aperture is limited by the size of the transducers used to excite and detect the guided waves relative to the outside circumference

of the pipe being inspected. The diameter of the transducers is dictated by the wavelength, of the guided wave mode selected. To achieve optimal radiation efficiency, the diameter should be equal to half the wavelength.

In addition, the full view configuration is not possible, when inspecting a section of pipe length with two ring arrays as discussed earlier. To recover some of the missing viewing angles, it can be observed that a wave pulse fired from a source acts like a two-dimensional (2-D) point source propagating outward and forming circular wave fronts. In a pipe, this circular wavefront is made up of wave-paths including the axial and circumferential directions, and a continuum of helical wave-paths. The method introduced in this thesis is based on the observation that for a given transmit–receive transducer pair there exists infinite helical wave-paths that connect the transmitter to the receiver each corresponding to a different number of turns around the pipe. Thus, it follows that the higher the order of the helical path, the larger the number of turns around the pipe and hence the better the ray coverage in the circumferential direction.

1.1.2 Parametric Uncertainties

TIPU, as previously stated, are errors in the input parameters of the forward model that cause distortions in the reconstruction of the state of the waveguide. Some of these errors can be alleviated by using differential measurements rather than absolute ones. Therefore, instead of attempting to retrieve the absolute state of the waveguide, the inversion is aimed at determining the change of the state of the waveguide. The change is measured by comparing the reference state represented by the so-called baseline measurements to the current state represented by the most recent measurements.

The advantage of using the differential measurements comes from the idea that TIPUs are present in both the baseline and current measurements, and since they are the same, they cancel out by the differential approach.

The differential approach is not effective in addressing the TDPU such as those produced

by temperature variation. In order to minimize the impact of temperature variations this thesis introduces a compensation technique that adjusts the baseline measurements to match the temperature of the current measurements. This approach is based on the observation that due to the spatial diversity of the array measurements, a temperature change affects the array measurements with a precise pattern determined by the relative distances between transducers.

1.1.3 New criterion for accuracy of GWT

Due to the nonlinear nature of GWT there is no analogy to the performance criterion of the PSF width in linear imaging methods. The forward model used in this thesis is based on ray theory. The limitation on the applicability of ray theory to serve as an accurate representation of wave propagation has been shown to be based on the size of the scattering objects relative to the size of the first Fresnel zone [43–45]. However, one of the assumptions made in developing this criterion is that the contrasts of the scattering objects are small. In addition, the wavefront healing phenomenon is regarded as a further cause of resolution degradation in ray tomography [46–48]. Wavefront healing can be considered by using the geometrical diffraction theory of Keller [49]. Moreover, accounting for geometrical diffraction becomes a necessity when realizing that ray theory supports this type of diffraction. This thesis introduces a new criterion which incorporates both ray and geometrical diffraction, in order to predict the accuracy of CRT based reconstructions.

1.1.4 GWT performance study

The performance of GWT refers to its ability to accurately size and characterize the extent of corrosion and erosion damage in pipes. Unlike linear inversions, an evaluation of performance cannot be given independent of the defect shape and size in the case of GWT, due to its nonlinear nature. Therefore, a large scale parametric study based on numerical simulations will be carried out. The study will test the accuracy of GWT over a range of test

configurations and defect morphologies. Pipes of different diameters and wall thicknesses will be considered along with various separation distances between the transmit and receive arrays, as well as numbers of elements per array. Accuracy will then be studied as a function of pipe, defect, and array parameters. The objective is to obtain guidelines that indicate the performance of GWT under various monitoring scenarios.

1.2 Outline

This thesis investigates and extends the ability of GWT to accurately reconstruct WTL maps in pipes. A framework for implementing GWT which incorporates higher-order helical modes in order to increase the amount of information characterizing damage in the pipe is presented. Ultimately this results in increased accuracy of the reconstructions. Effective methods for the amelioration of errors due to parametric uncertainties are also presented. A novel criterion to predict the ability of GWT to accurately reconstruct the maximum WTL is introduced, and validated against simulated data with both full view circular arrays, and limited view parallel linear arrays. Finally, an investigation of the parametric effects on GWT performance is carried out, and reported as a guide for the implementation of GWT.

In Chapter 2 a review of guided waves is undertaken. Links between guided wave propagation in pipes and plates are made, and a justification for approximating guided waves in pipes as those in plates is given. The applicability of this approximation relies on a sufficiently small ratio of pipe wall thickness to pipe radius.

A method for the implementation of GWT is presented in Chapter 3. The description contains a method of virtually extending the linear arrays using the higher-order helical modes. A simulated example of the increased accuracy that results from the consideration of higher-order helical modes is also given.

Parametric uncertainties are addressed in Chapter 4. A method for TIPU compensation, based on a differential approach is reviewed. This method is used in all reconstructions in this

thesis. The method for TDPU compensation based on the minimization of a cost function is discussed, and subsequently applied to the TDPU of thermal variation, and experimental results given.

In Chapter 5 a new criterion of accuracy is in introduced. This comes about naturally by reconciling the geometrical diffraction theory of Keller [49], wavefront healing [46–48], and ray theory. The result is a limit on the contrast that can be reconstructed by GWT based on the width of the contrast support. The criterion is tested by evaluating the errors in reconstruction of a series of fast and slow inclusions of multiple widths, and contrast values. The results show that the criterion defines a space for slow inclusions in width and contrast where defects are accurately reconstructed. Counterintuitively, there is no similar limit observed for the case of fast inclusions.

This new criterion has important implications on the implementation of GWT studied in this thesis due to all damage in pipes being characterized as slow contrasts within the GWT algorithm. Chapter 6 serves as a performance review of GWT based on evaluations of the error in maximum WTL reconstructions, as a function of pipe, defect, and array parameters. In addition, the criterion introduced in Chapter 5 is applied as a filter so that errors observed are not due to the defects whose width and contrast are outside of the criterion.

A summary of conclusions are presented in Chapter 7, as well as a review of potential future research.

Chapter 2

Guided waves

To understand guided waves, it is best to first review an example from optics. Consider the problem of transmitting a binary message over a long distance. By turning a light bulb on and off, one could transmit a binary message that could be received in any direction. However, from very far away, it may be difficult to receive the message because of the loss of signal strength due to the spreading of energy over the wavefront. While useful, this method would not be reliable for sending long range communications.

In order to overcome this challenge, fiber optic cables have been developed as waveguides which channel optical energy along their length with very little loss of signal strength. A simple fiber optic cable has an internal glass core, which is surrounded by a cladding material. To create the guided wave, light is sent into the glass core with some angle of incidence, shown as θ_i in Fig. 2.1. At the boundary between the core and the cladding, some of the light is reflected at an angle θ_r, and some light is transmitted through the boundary into the cladding at an angle θ_t, in accordance with Snell's law, given as

$$k_1 \sin(\theta_i) = k_1 \sin(\theta_r) = k_2 \sin(\theta_t), \tag{2.1}$$

where

$$k = \frac{\omega}{c} = \frac{2\pi f}{c} = \frac{2\pi}{\lambda}. \tag{2.2}$$

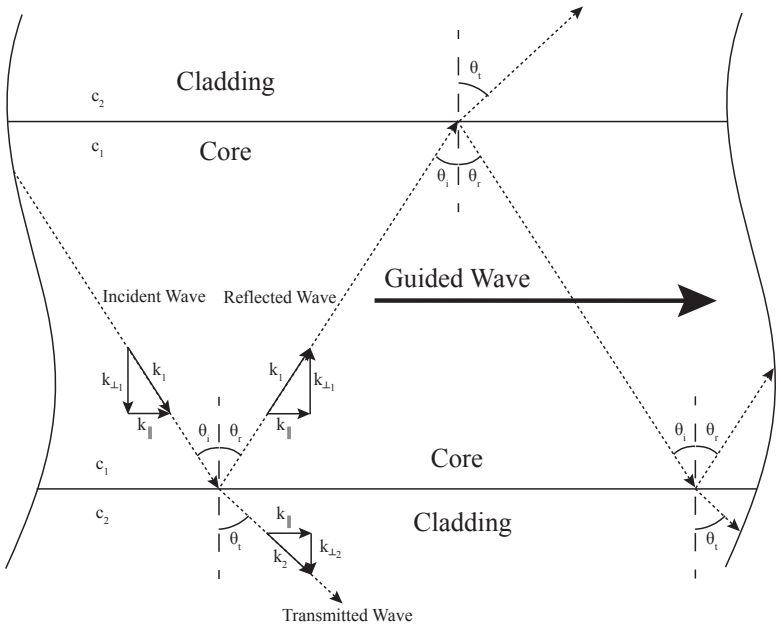

Figure 2.1: A section of fiber optic cable is shown. The multiple reflections in the core result in the generation of a guided wave.

The angles of incidence, reflection and refraction (shown as transmission) at the boundary will be such that each of their wavenumber components parallel to the boundary will be equal [50, p. 316]. In Eq. (2.1), k refers to a spatial angular frequency termed the wavenumber, which is a function of the propagation velocity in the medium, c, and the angular frequency of the wave, ω, as in Eq. (2.2). Angular frequency is a multiple of temporal frequency, f, by 2π. Finally, θ refers to the angle of the wave propagation direction relative to the direction normal to the boundary between the two materials.

The vector k, can be represented as,

$$k^2 = k_{\parallel}^2 + k_{\perp}^2 = \frac{\omega^2}{c^2}, \tag{2.3}$$

where it has been decomposed into the component of the wave that is parallel to the boundary, $k_{\parallel}$, and the component that is normal to the boundary, $k_{\perp}$. Snell's law shows that both the incident and reflected waves have $k_{\parallel}$ in the same direction and equal in value. As a result, the two interfering waves form a new wave mode that propagates parallel to the interfaces.

Using the definition of k as ω/c, the effective velocity of propagation along the waveguide is termed the phase velocity, given by

$$c_{ph} = \frac{\omega}{k_{\|}}. \tag{2.4}$$

In addition, by properly selecting the angle of incidence and the core/cladding materials, a scenario in which no energy is transmitted to the cladding, termed total internal reflection, can be achieved. The result is a wave with minimal energy loss whose net propagation is along the length of the cable. In this way, the light transmitted through the fiber optic cable is said to be a guided wave. The benefit of this is a reliable stream of binary data that is received much further away than would be possible using the light bulb alone.

In the case of elastic waves, the optical wave advancing from a light bulb is analogous to a source emitting bulk waves in an unbounded isotropic solid medium, which is described by the Navier governing equation, given as

$$(\lambda' + \mu')\nabla\nabla \cdot \mathbf{u} + \mu'\nabla^2\mathbf{u} + \rho\mathbf{f} = \rho\ddot{\mathbf{u}}, \tag{2.5}$$

in [50, p. 274]. In Eq. (2.5), $\mathbf{u}$ describes a displacement vector field in an appropriate three-dimensional (3-D) coordinate system. In this equation, ∇ represents the gradient operator, and ∇^2 represents the Laplacian. The material particle acceleration field is noted as $\ddot{\mathbf{u}}$. The constant ρ refers to the material density of the medium, and $\mathbf{f}$ refers to the body force vector field. Finally, the first and second Lamé constants, λ' and μ' are related to the Young's modulus, E, and Poisson's ratio, ν, according to

$$\lambda' = \frac{E\nu}{(1+\nu)(1-2\nu)}, \text{ and } \mu' = \frac{E}{2(1+\nu)}. \tag{2.6}$$

The two types of bulk waves that are supported by an elastic medium are termed longitudinal (L) and shear (S) waves. The L waves are characterized by their displacement polarization (direction) being in the same direction as their wave propagation. Conversely,

S waves displacement polarization is orthogonal to the direction of their wave propagation. For this reason, the Helmholtz decomposition is given by

$$\mathbf{u} = \nabla\phi + \nabla \times \mathbf{\Psi}, \text{ where } \nabla \cdot \mathbf{\Psi} = 0. \tag{2.7}$$

This relation represents the displacement field as a superposition of the L wave component (the gradient of a scalar, $\nabla\phi$), and the S wave component (the curl of a zero divergence vector, $\nabla \times \mathbf{\Psi}$) [51, p. 25].

It can be shown that by substituting Eq. (2.7) into Eq. (2.5) and neglecting the body forces, the result is two separate wave equations,

$$\nabla^2\phi = \frac{1}{c_L^2}\ddot{\phi}, \tag{2.8}$$

and

$$\nabla^2\mathbf{\Psi} = \frac{1}{c_S^2}\ddot{\mathbf{\Psi}}, \tag{2.9}$$

where

$$c_L^2 = \frac{\lambda' + 2\mu'}{\rho}, \text{ and } c_S^2 = \frac{\mu'}{\rho}. \tag{2.10}$$

Equations (2.8) and (2.9) govern the L and S waves independently in an infinite solid medium. The velocity of the L and S waves propagation is given in terms of Lamé constants in Eq. (2.10).

In the case where L or S waves interact with a boundary, mode conversion may occur. Mode conversion refers to the generation of both L and S waves reflected and transmitted from a boundary when an L or S wave is incident upon the boundary. The propagation directions of the mode converted waves are related using Eq. (2.1). Note that the S waves generated from an incident L wave will have a polarization in the plane defined by the normal to the surface and the direction of the incident wave. In addition, an incident S wave with polarization orthogonal to the surface normal will not mode convert.

Just as in the fiber optic example, elastic bulk waves can also be guided by reflection from boundaries. Additionally, many engineering structures present themselves as waveguides, such as plates, pipes or rods. This makes inspection of such structures using guided waves a natural choice. Of course in the case of elastic guided waves the interest is no longer in transmitting binary data, but rather, transmitting a single wave pulse through the structure in order to detect the presence of damage. In the following sections, a review of guided waves in structures relevant to GWT will be carried out.

2.1 Guided waves in plates

The flat plate waveguide is a bit different than the fiber optic cable in geometry, but in principle, the same rules will apply. The boundaries support the reflections of bulk waves from the surfaces of the plate. The propagation directions of these reflections are again governed by Eq. (2.1). In this case, the plate is subject to traction free conditions given by

$$\boldsymbol{\sigma}^t = \mathbf{0}, \text{ and } \boldsymbol{\sigma}^b = \mathbf{0}, \tag{2.11}$$

where $\boldsymbol{\sigma}^t$ and $\boldsymbol{\sigma}^b$ refer to traction vectors given at the top and bottom surfaces. These boundary conditions in conjunction with Snell's law determine the characteristics of the guided waves that can propagate in the plate.

2.1.1 Shear horizontal waves

Similar to the fiber optic example, guided waves result from a superposition of the up and down reflecting bulk waves. As the name suggests, shear horizontal (SH) guided waves originate from the reflection of S waves with a polarization that lies in a direction that is parallel to both surfaces of the plate, and orthogonal to the direction of wave propagation, as shown in Fig. 2.2. Due to the polarization of the S waves, no mode conversion will occur. Thus, the y direction is chosen as the direction of displacement polarization, and the

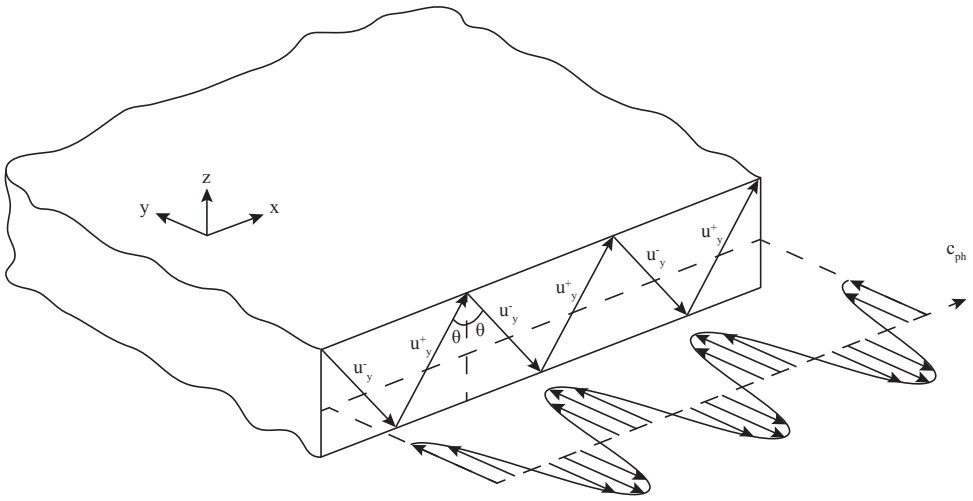

Figure 2.2: An example of SH guided wave propagation in an infinite plate is shown. The dotted plane is the mid-surface of the plate, in which a slice of the displacement distribution is shown. The reflected S waves propagation directions are shown as u_y^+ and u_y^-, and the SH direction is shown as c_{ph}.

x direction as being parallel to the propagation direction.

The displacement field of an SH guided wave can be expressed as,

$$u_y(x, z; t) = Am_y(z)e^{i(k_\parallel x - \omega t)}, \tag{2.12}$$

where, A is an arbitrary amplitude, and $m_y(z)$ describes the distribution of particle displacement in the y direction through the thickness of the plate termed a mode shape. The complex exponential factor describes the harmonic relationship between time, t, and propagation along the x direction. This harmonic relationship is termed the phase propagation factor. Just as in the fiber optic cable example, $k_\parallel = \frac{\omega}{c_{ph}}$, is the guided mode wavenumber.

Consider that $k_\perp$ will define the mode shape by determining its number of oscillations. Thus, k and $k_\perp$ of the S waves will determine the guided propagation characteristics $k_\parallel$ and by extension c_{ph}. In order to find $k_\perp$, the partial wave method [51, p. 107] is employed by representing the multiple reflections of the bulk waves as one up and one down reflecting S wave. These two partial waves must satisfy the traction free boundary conditions given in Eq. (2.11).

Due to the polarization of the S waves, only one shear stress component of the boundary condition is required, given by the Hooke's law relation

$$\sigma_{zy} = \mu' \frac{\partial u_y}{\partial z}. \tag{2.13}$$

The polarization also reduces Eq. (2.9) to

$$\nabla^2 u_y = \frac{1}{c_S^2} \ddot{u}_y. \tag{2.14}$$

The partial wave solutions to the simplified wave equation (2.14) are defined as

$$\begin{aligned} u_y^+(x,z;t) &= A^+ e^{i(k_\parallel x + k_\perp z - \omega t)}, \\ u_y^-(x,z;t) &= A^- e^{i(k_\parallel x - k_\perp z - \omega t)}, \end{aligned} \tag{2.15}$$

where u_y^+ is the up reflected bulk wave, and u_y^- is the down reflected bulk wave, as represented in Fig. 2.2.

Substituting each partial wave given in Eq. (2.15) into the Hooke's law given by Eq. (2.13) gives the partial waves contribution to the surface shear stresses as, σ_{zy}^{t+}, σ_{zy}^{t-}, σ_{zy}^{b+} and σ_{zy}^{b-}, where the superscripts t and b respectively refer to the top and bottom surfaces, and as before $+$ and $-$ refer to the component's origin as either an up or down reflecting partial wave. The summation of these components at the top and bottom surfaces together with the boundary condition from Eq. (2.11), gives

$$\begin{aligned} \sigma_{zy}^t &= \sigma_{zy}^{t+} + \sigma_{zy}^{t-} = 0, \\ \sigma_{zy}^b &= \sigma_{zy}^{b+} + \sigma_{zy}^{b-} = 0. \end{aligned} \tag{2.16}$$

Reformulating Eq. (2.16) as a matrix equation yields

$$\begin{Bmatrix} 0 \\ 0 \end{Bmatrix} = \begin{bmatrix} d^{t+}(\theta) & d^{t-}(\theta) \\ d^{b+}(\theta) & d^{b-}(\theta) \end{bmatrix} \begin{Bmatrix} A^{+} \\ A^{-} \end{Bmatrix} e^{i(k_{\parallel}x-\omega t)} = \mathbf{D}\ \boldsymbol{a} e^{i(k_{\parallel}x-\omega t)}, \tag{2.17}$$

where the $d(\theta)$ can be thought of as a directional component of the stress contribution in terms of the incident/reflected angle, θ, the partial wave of origin, and the boundary with which it interacts. In order for Eq. (2.17) to admit a non-trivial solution ($\mathbf{a} \neq \mathbf{0}$), the determinant of $\mathbf{D}$ must vanish, i. e.

$$|\mathbf{D}| = 0. \tag{2.18}$$

Since $k_{\perp} = k\cos(\theta)$, this can be thought of as an equation in $k_{\perp}$. It is termed the characteristic, or secular equation. It is shown in [51] that it admits a countably infinite set of solutions,

$$k_{\perp}^{n} = \frac{n\pi}{d} \text{ where } \begin{cases} n \in \{0, 2, 4, ...\} \text{ for symmetric modes,} \\ n \in \{1, 3, 5, ...\} \text{ for antisymmetric modes.} \end{cases} \tag{2.19}$$

These correspond to the n modes of the SH guided waves. Each SH mode will from here on be noted using a subscript n to refer to its order (e.g. SH_n is the n-th order SH mode). An example of the SH_1 and SH_2 mode shapes are shown in Fig. 2.3.

Equation (2.19) gives $k_{\perp}^{n}$ as a integer number of half oscillations that make up the mode shape present in the thickness of the plate, d, where the even n give symmetric modes and the odd give antisymmetric modes. This leads to each mode having its own relationship to c_{ph}. In order to determine this relationship, Eqs. (2.19) and (2.4) are rearranged and substituted into Eq. (2.3) yielding

$$\frac{\omega^2}{c_S^2} = \frac{\omega^2}{c_{ph}^2} + \left(\frac{n\pi}{d}\right)^2. \tag{2.20}$$

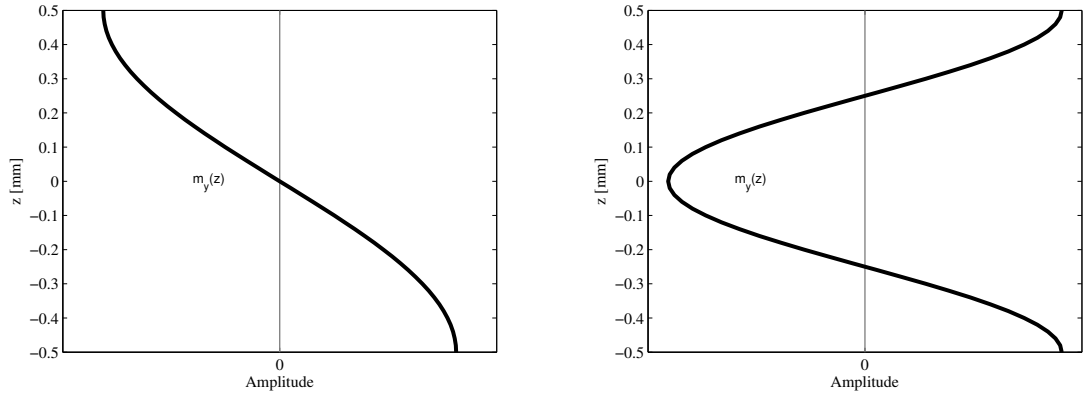

Figure 2.3: The mode shapes of SH_1 and SH_2 are shown in (a) and (b) respectively at a frequency-thickness product of 5 MHz-mm in a steel plate 1 mm thick. These have been normalized by power flow in the direction of guided wave propagation.

Solving Eq. (2.20) for c_{ph} results in

$$c_{ph} = \frac{2c_S fd}{\sqrt{4(fd)^2 - n^2 c_S^2}}, \tag{2.21}$$

which gives the phase velocities for all SH_n.

The first six phase velocity curves for a steel plate are shown in Fig. 2.4(a). An interesting result is that the phase velocity is dependent on the frequency-thickness product, $f \cdot d$, rather than the frequency and thickness independent of one another. It should also be noted that for each of the higher-order modes (i. e. $n > 0$) there exists a frequency-thickness product where the phase velocity becomes infinite. These are termed cutoff frequency-thickness products. Below these cutoffs, the energy flow of the modes vanishes and the mode becomes nonpropagating.

For a given thickness, d, the phase velocity decreases with frequency. As a consequence, the higher frequency components of a wave pulse tend to travel at a lower speed than the low frequency components. This can cause significant pulse distortion as the slow frequencies trail behind the fast ones. Under these conditions the velocity at which the pulse propagates

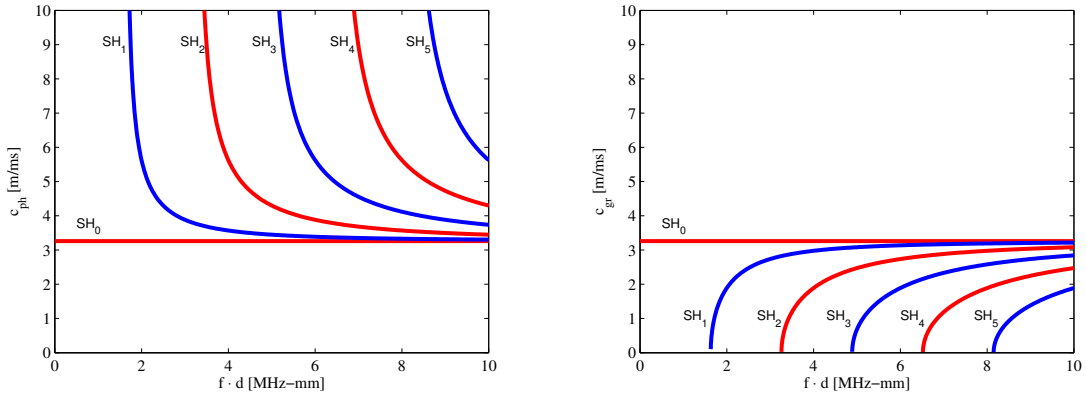

(a) (b)

Figure 2.4: The phase velocity (a) and group velocity (b) dispersion curves of SH waves in a steel plate are shown. The red curves refer to the symmetric modes, and blue curves refer to the antisymmetric modes. In both cases, the subscripts refer to the mode order n.

is given by the so called group velocity,

$$c_{gr} = \frac{\partial \omega}{\partial k_{\|}}, \tag{2.22}$$

which refers to the velocity of the center of gravity of the pulse envelope. The group velocity dispersion curves corresponding to the modes shown in Fig. 2.4(a), are given in Fig. 2.4(b).

2.1.2 Lamb waves

Lamb waves are another type of guided wave that are supported in plates subject to the same traction free boundary condition given in Eq. (2.11). They are the result of a superposition of the L and S waves whose displacements adhere to a plane strain condition, given by

$$u_y = \frac{\partial}{\partial y} = 0. \tag{2.23}$$

Thus the displacement occurs only in the plane formed by the chosen propagation direction, x, and the normal to the surfaces of the plate. This means that the L and S waves will mode convert at the boundaries.

The solution form for Lamb waves is given by,

$$\begin{Bmatrix} u_x(x,z;t) \\ u_z(x,z;t) \end{Bmatrix} = A \begin{Bmatrix} m_x(z) \\ m_z(z) \end{Bmatrix} e^{i(k_\parallel x - \omega t)}. \tag{2.24}$$

This equation includes an arbitrary amplitude A and two mode shape terms, $m_x(z)$ and $m_z(z)$. The mode shapes and dispersion curves can be solved by the partial wave method, as was done in the review of SH guided waves. The multiple reflections are represented by a pair of up and down reflecting partial waves for each of the L and S waves that propagate in the xz plane.

Due to the plane strain condition, the traction free boundary condition will only involve the corresponding shear and normal stresses at the surfaces of the plate. This boundary condition is given as

$$\begin{Bmatrix} \sigma^t_{zz} \\ \sigma^t_{zx} \\ \sigma^b_{zz} \\ \sigma^b_{zx} \end{Bmatrix} = \mathbf{0}. \tag{2.25}$$

In addition, this boundary condition now implies that $\mathbf{D}$ will be a four by four matrix, in which each element represents the contribution from each partial wave to a particular surface stress component. In this case, the characteristic equation yields the Rayleigh-Lamb equation [52–54] , given as

$$\frac{tan(k_{\perp S}d/2)}{tan(k_{\perp L}d/2)} = -\left[\frac{4k_{\perp L}k_{\perp S}k_\parallel^2}{(k_{\perp S}^2 - k_\parallel^2)^2}\right]^{\pm 1} \tag{2.26}$$

where

$$k_{\perp L}^2 = \frac{\omega^2}{c_L^2} - k_\parallel^2, \text{ and } k_{\perp S}^2 = \frac{\omega^2}{c_S^2} - k_\parallel^2. \tag{2.27}$$

In Eq. (2.26) the $+1$ exponent of the right hand side yields an equation that gives the symmetric modes (S_n) while the -1 exponent gives the antisymmetric modes (A_n), where

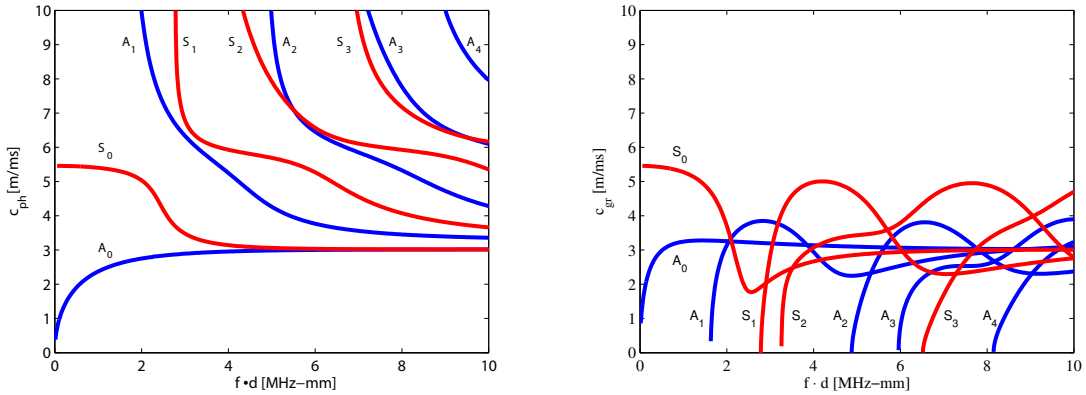

(a) (b)

Figure 2.5: The phase velocity (a) and group velocity (b) dispersion curves of Lamb waves in a steel plate are shown. The red curves refer to the symmetric (S_n) modes, and blue curves refer to the antisymmetric (A_n) modes. The subscripts n refers to the mode order.

the subscript, n, refers to the mode order. Also, in Eq. (2.27), $k_{\perp L}$ and $k_{\perp S}$ refer to the corresponding L and S bulk wavenumber components that are in the direction normal to the plate surfaces. Due to nonlinearity, this equation is only solvable by numerical methods. Such a procedure is outlined in [51, p. 110]. DISPERSE is a software package that implements such numerical methods for the analysis of guided waves, and is used to produce the dispersion curves and mode shapes shown in the present review [55].

The symmetric and antisymmetric Lamb wave dispersion curves are shown in Fig. 2.5. Many of the same features that were present in the SH dispersion curves are observed in this case as well, such as the dispersion curves dependence on the frequency-thickness product, and the existence of cutoff frequency-thickness products.

The mode shapes corresponding to A_0 and S_0 are shown in Fig. 2.6. These modes are termed the fundamental flexural and extensional modes respectively.

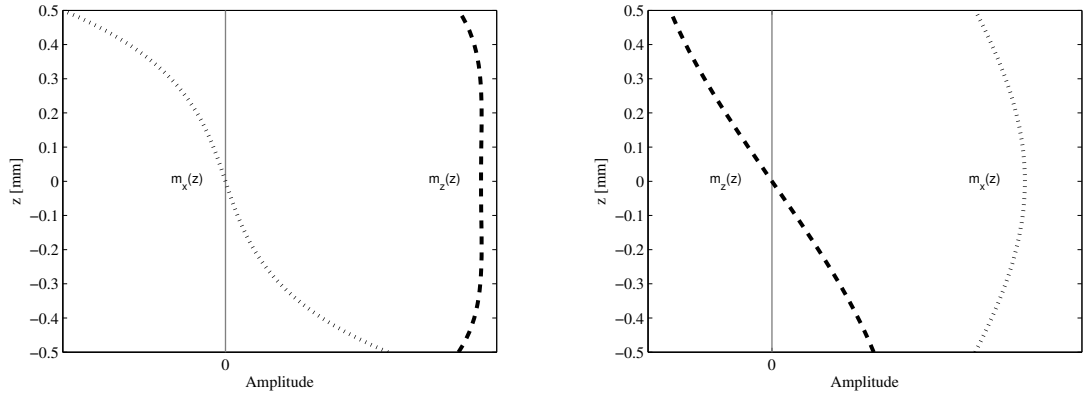

(a) (b)

Figure 2.6: The mode shapes of A_0 and S_0 are shown in (a) and (b) respectively at a frequency-thickness product of 1.4 MHz-mm in a steel plate 1 mm thick. These have been normalized by power flow in the direction of guided wave propagation.

2.2 Guided waves in pipes

As before, guided waves in pipes result from a superposition of bulk waves reflecting between the two cylindrical surfaces of the pipe. The boundary conditions are given by

$$\boldsymbol{\sigma}^i = \mathbf{0}, \text{ and } \boldsymbol{\sigma}^o = \mathbf{0}, \tag{2.28}$$

where $\boldsymbol{\sigma}^i$, and $\boldsymbol{\sigma}^o$ refer to the inner and outer surface traction vectors. Using these boundary conditions, dispersion curves for all axial and circumferential guided waves in pipes can be solved for via the partial wave method. The form of $\mathbf{D}$ for the different classes of axial and circumferential guided waves are given in [50, 51, 56, 57].

Reconsidering guided waves in the plate, the propagation direction is assumed to be in the x direction for both SH and Lamb waves. In the case of the pipe, modes similar to the SH and Lamb modes will propagate in both axial and circumferential directions. This could be conceptualized as wrapping the plate into a pipe by transforming either the x or y axis of the plate into a ring. In the following sections, comparisons between the guided modes in pipes and plates will be made to show the validity of approximating guided pipe modes as

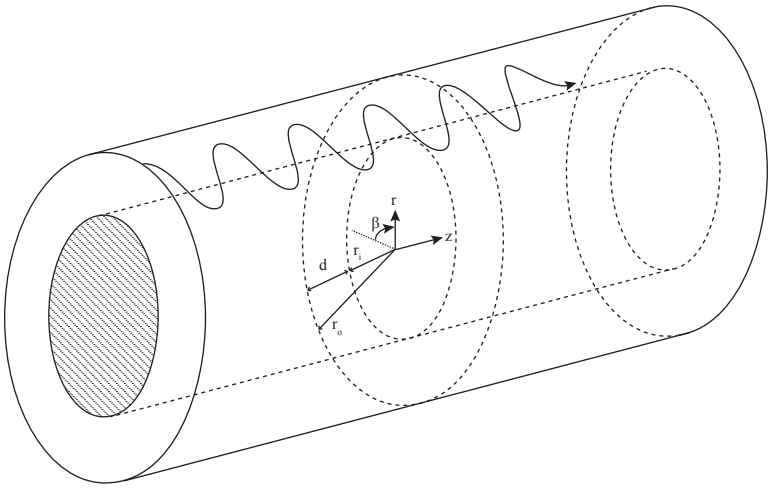

Figure 2.7: A section of pipe is shown with a representation of an axial guided wave propagating along the z direction of the cylindrical coordinate system.

guided plate modes when the ratio of pipe wall thickness to the inner radius is small [58].

2.2.1 Axial guided waves

Axial guided waves are characterized by their propagation direction being along the axial dimension of the pipe, as shown in Fig. 2.7, where the z axis is chosen as the propagation direction in terms of the cylindrical coordinate system shown. The axial guided waves are divided into three classes of modes: pure torsional, $\mathrm{T}(0,q)$, longitudinal, $\mathrm{L}(0,q)$, and flexural, $\mathrm{F}(p,q)$, as done in [59]. The circumferential order, p, corresponds to the number of cycles of variation of the displacement field around the circumference, while the radial order, q, describes the displacement distribution through the thickness of the pipe, just as the mode order did in plates. When the circumferential order is zero, the modes displacement is axially symmetric, and the classes $\mathrm{T}(0,q)$ and, $\mathrm{L}(0,q)$ are obtained.

The general displacement field solution for the axial guided waves is given as

$$\begin{Bmatrix} u_r(r,\beta,z;t) \\ u_\beta(r,\beta,z;t) \\ u_z(r,\beta,z;t) \end{Bmatrix} = A \begin{Bmatrix} m_r(r) \\ m_\beta(r) \\ m_z(r) \end{Bmatrix} e^{ip\beta} e^{i(k_\parallel z - \omega t)}. \tag{2.29}$$

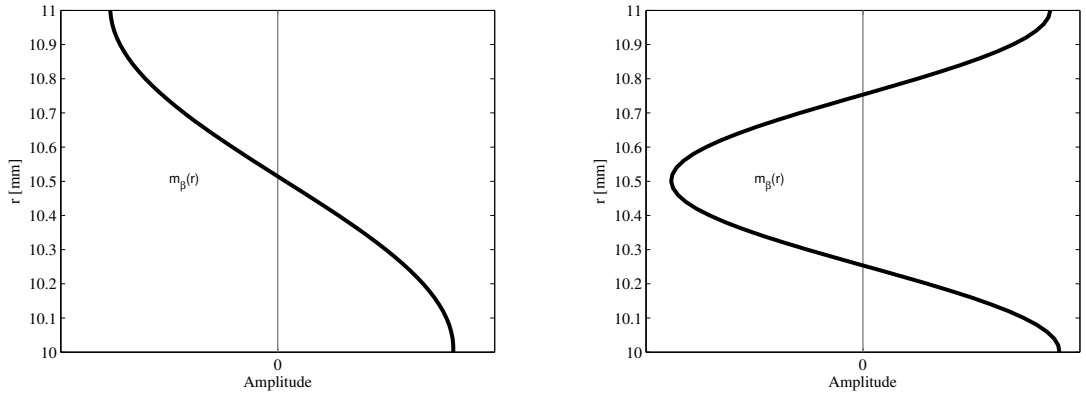

Figure 2.8: The mode shapes of T$(0,2)$ and T$(0,3)$ are shown in (a) and (b) respectively at a frequency-thickness product of 5 MHz-mm in a steel pipe with 10 mm inner radius and 1 mm wall thickness. These have been normalized by power flow in the direction of guided wave propagation.

In this equation, A is an arbitrary amplitude, $m_r(r)$, $m_\beta(r)$, and $m_z(r)$ are the mode shapes corresponding to each of the cylindrical coordinates, p represents the circumferential order, and $k_\parallel$ describes the wavenumber of propagation along the z axis. The dispersion characteristics of each mode class are obtained by imposing the traction free boundary condition given by Eq. (2.28). In the case of the pipe, the characteristic equation (2.18) is an implicit transcendental function of $\frac{d}{\lambda}$ and $\frac{fd}{c_S}$. The roots of (2.18) can be determined by fixing $\frac{d}{\lambda}$ and solving for $\frac{fd}{c_S}$, or vice versa, as proposed by Gazis in [56, 58]. The DISPERSE software package is used in this review to generate dispersion curves and mode shapes of axial guided waves in pipes [55].

T$(0,q)$ pipe modes have only a single displacement component that is orthogonal to both the surface normal direction, and direction of propagation. Thus, $u_r(z)$ and $u_z(z)$ vanish, which simplifies the displacement field given in Eq. (2.29) to

$$u_\beta(r,z;t) = Am_\beta(r)e^{i(k_\parallel z-\omega t)}, \tag{2.30}$$

which represents a pure twisting motion. The similarities between T$(0,q)$ and SH modes are

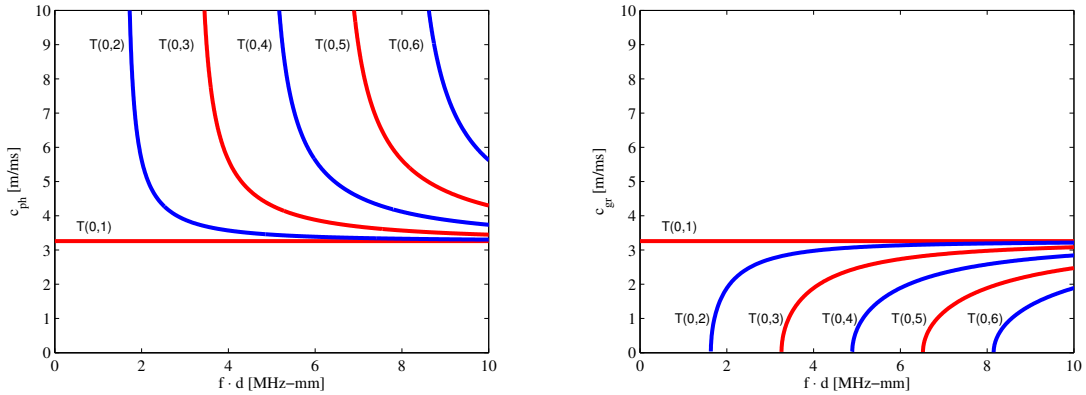

(a) (b)

Figure 2.9: The phase velocity (a) and group velocity (b) dispersion curves of $\mathrm{T}(0,q)$ in a steel pipe with 10 mm inner radius and 1 mm wall thickness are shown. The red curves refer to the symmetric modes, and blue curves refer to the antisymmetric modes.

apparent when comparing the mode shapes of each in Fig. 2.8 and Fig. 2.3, and the phase velocity dispersion curves of each shown in Fig. 2.9 and Fig. 2.4.

The $\mathrm{L}(0,q)$ displacements have no component in the circumferential direction, which reduces the displacement field given in Eq. (2.29) to

$$\begin{Bmatrix} u_r(r,z;t) \\ u_z(r,z;t) \end{Bmatrix} = A \begin{Bmatrix} m_r(r) \\ m_z(r) \end{Bmatrix} e^{i(k_\parallel z - \omega t)}. \tag{2.31}$$

Similar to Lamb waves, the $\mathrm{L}(0,q)$ modes result from the outward and inward L and S waves reflecting between the surfaces of the pipe. The mode shapes of $\mathrm{L}(0,1)$ and $\mathrm{L}(0,2)$ in Fig. 2.10 appear to be similar to those of the A_0, and S_0 in Fig. 2.6. There is also agreement between the respective dispersion curves shown in Fig. 2.11 and Fig. 2.5.

Unlike the $\mathrm{T}(0,q)$ and $\mathrm{L}(0,q)$ classes, $\mathrm{F}(p,q)$ has a full 3-D displacement solution as given in Eq. (2.29). Due to the circumferential order, p, having a minimum of one, all of the displacement components will vary sinusoidally, around the circumference, where the circumferential order gives the number of oscillations. This leads to a situation in which some radial orders of the $\mathrm{F}(p,q)$ modes will converge to the SH modes and others will converge to

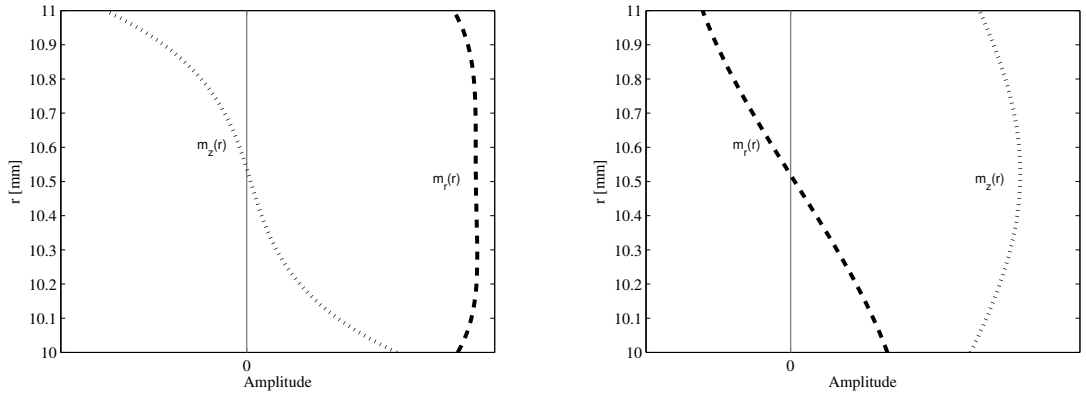

Figure 2.10: The mode shapes of $L(0,1)$ and $L(0,2)$ are shown in (a) and (b) respectively at a frequency-thickness product of 1.4 MHz-mm in a steel pipe with 10 mm inner radius and 1 mm wall thickness. These have been normalized by power flow in the direction of guided wave propagation.

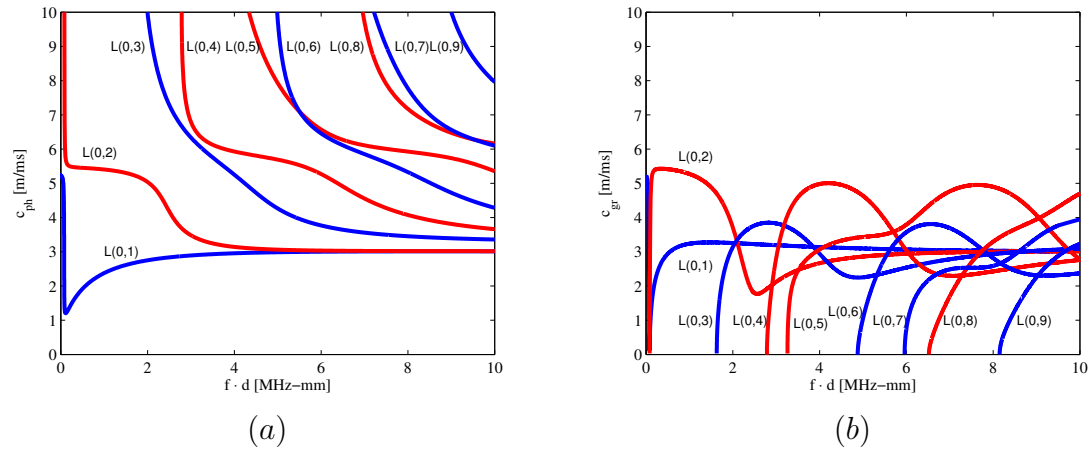

Figure 2.11: The phase velocity (a) and group velocity (b) dispersion curves of $L(0,q)$ in a steel pipe with 10 mm inner radius and 1 mm wall thickness are shown. The red and blue curves refer to the symmetric and antisymmetric modes respectively.

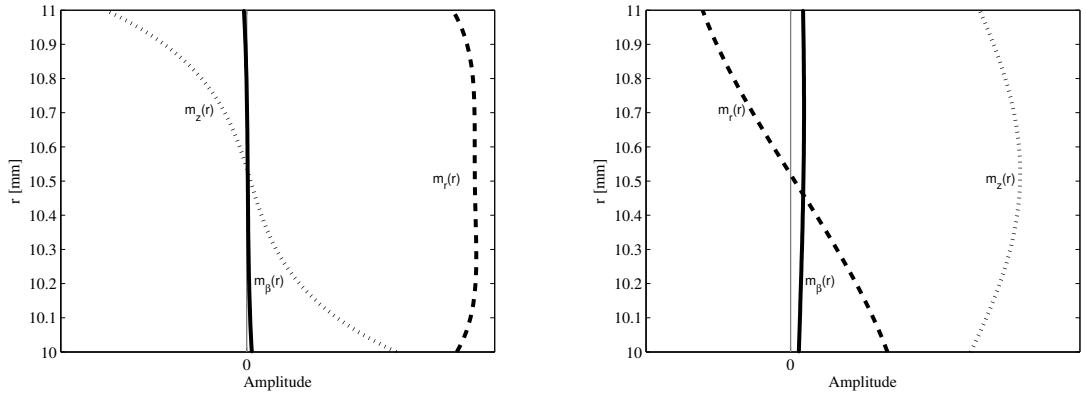

Figure 2.12: The mode shapes of F$(1,1)$ and F$(1,3)$ are shown in (a) and (b) respectively at a frequency-thickness product of 1.4 MHz-mm in a steel pipe with 10 mm inner radius and 1 mm wall thickness. These have been normalized by power flow in the direction of guided wave propagation.

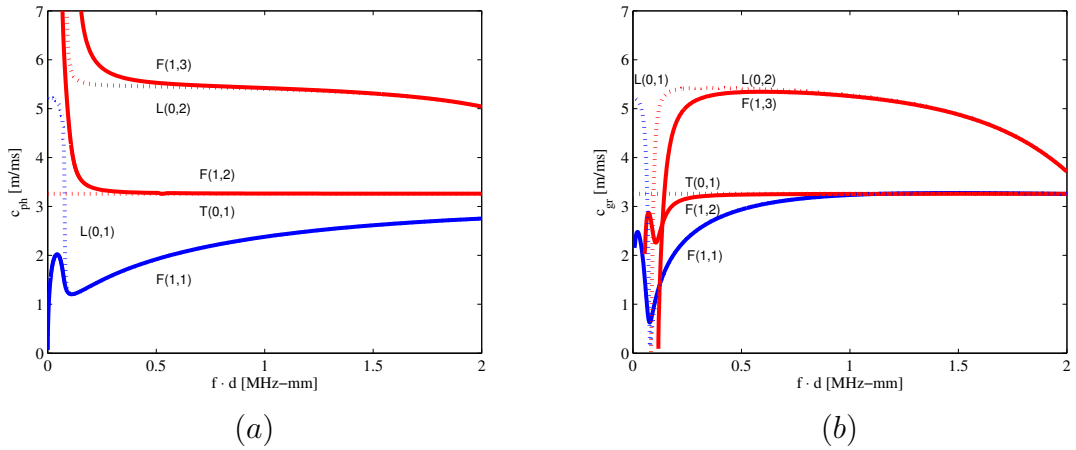

Figure 2.13: The phase velocity (a) and group velocity (b) dispersion curves of F$(1,q)$ in a steel pipe with 10 mm inner radius and 1 mm wall thickness are shown for $q = \{1,2,3\}$. The L$(0,1)$, T$(0,1)$, and L$(0,2)$ dispersion curves are also shown for comparison.

the Lamb modes.

In Fig. 2.12, the mode shapes of F(1, 1) and F(1, 3) are shown. Notice that the maximum amplitude of $m_\beta(r)$ is much smaller than those of the other mode shapes. When comparing the more dominant $m_r(r)$ and $m_z(r)$ mode shapes of this figure with those shown for L(0, 1) and L(0, 2) in Fig. 2.10 or A_0 and S_0 in Fig. 2.6, good agreement is observed in both cases. Additionally, when comparing the dispersion curves shown in Fig. 2.13 it is clear that the F(p, q) modes converge to the T($0, q$) or L($0, q$) modes, who in turn converge to the corresponding plate modes for high frequency-thickness products.

In the present review of axial guided waves, it has been observed that each guided mode in a pipe will have an analogy to a guided plate mode. However, it is necessary to understand why the similarity between the pipe and plate modes dispersive characteristics exists. The mode shapes in plates are made up of sinusoids, while mode shapes in pipes are composed of Bessel functions [50, p. 476]. For large frequency-radius products, and small ratio of wall thickness, d, to inner radius, r_i, given as

$$\eta = \frac{d}{r_i}, \tag{2.32}$$

the Bessel functions will approximate the sinusoids well [56, 60]. Because the characteristic equation is composed of the same terms as the mode shapes, the solution of the dispersion curves will also depend on the ratio of wall thickness to inner radius [51, 56, 58], as well as the frequency-thickness product. The effect of this is that for a pipe of given dimensions, the low frequency-thickness products correspond to a disagreement between the dispersion curves of the pipe modes and their plate analogs. In addition, increased circumferential order is shown in [57, 58] to increase the range of low frequency-thickness products for which there is poor agreement between dispersive properties of plates and pipes. Given these facts and the previous observations, it is concluded that it is reasonable to approximate the axial guided waves in pipes by their plate counter parts when the ratio of pipe wall thickness to

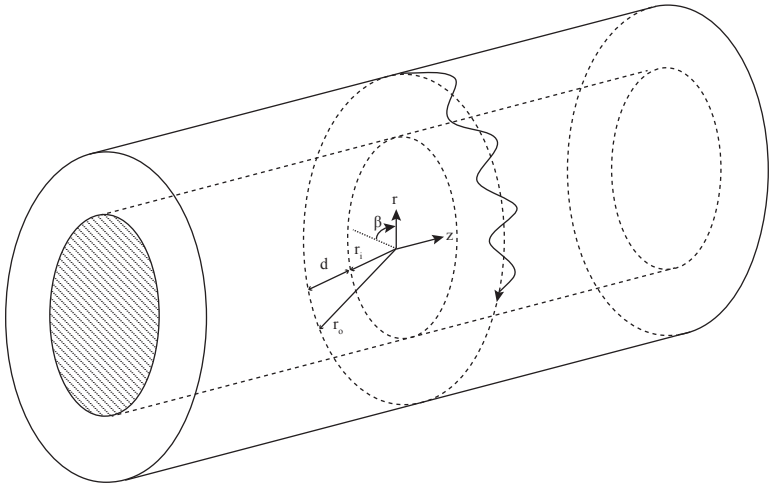

Figure 2.14: A section of pipe is shown with a representation of a circumferential guided wave propagating in the β direction of the cylindrical coordinate system.

internal radius is small ($\eta \leq 0.1$), and the frequency-thickness product used is above of the region where the dispersion curves diverge.

2.2.2 Circumferential guided waves

Circumferential guided waves propagate in the $z = 0$ plane, and follow a circular path defined by the inside and outside boundaries of the pipe, as shown in Fig. 2.14. The solution form given in Eq. (2.29) is still valid, but now $k_{\|}$ is set equal to zero to eliminate propagation in the z direction. This leads to the incorporation of the exponential that contained the circumferential order into the phase propagation factor, which results in the new solution form given by

$$\begin{Bmatrix} u_r(r,\beta;t) \\ u_\beta(r,\beta;t) \\ u_z(r,\beta;t) \end{Bmatrix} = A \begin{Bmatrix} m_r(r) \\ m_\beta(r) \\ m_z(r) \end{Bmatrix} e^{i(k_\circ r_o \beta - \omega t)}. \tag{2.33}$$

What was previously the circumferential order p in the axial guided wave solution is now termed the angular wavenumber, and it is the product of the circular wavenumber, $k_\circ$, and outer radius of the pipe, r_o [57]. The circular wave number is analogous to $k_{\|}$ from the previous cases, but now it is related to the propagation of a guided wave around the

circumference.

In the case of the shear horizontal type circumferential modes (CSH), the displacement is limited to u_z, as shown in Fig. 2.14. The circumferential Lamb symmetric (CLS) and antisymmetric (CLA) modes abide by the plane strain, given as

$$u_z = \frac{\partial}{\partial z} = 0. \tag{2.34}$$

Again, each mode has a corresponding mode order, n, which is noted as subscript of the specific mode (e.g. CLA_0 is the zero order CLA mode). The dispersion curves and mode shapes of the CSH, CLS, and CLA are solved again by the partial wave method as in the case of axial guided waves, and thus the convergence towards the guided plate modes is similar. Also, it is shown in [61, 62] that the dispersion curves of the circumferential guided modes are universal for any pipe with common ratio of wall thickness to inner radius. A complete derivation of CSH, CLS, and CLA is given in [57]. Similar to the axial dispersion curves, there is disagreement between the dispersion curves of the circumferential guided waves and those of the plate for low frequency-thickness products, and good agreement elsewhere, as is stated by Rose in [51, p. 157], and shown in [61, 62].

2.3 Mode selection for GWT

While reviewing guided waves, it was observed that there are many guided wave modes that are available to be used to detect WTL in plates and pipes. In previous applications of GWT to flat plates it has been shown that guided wave scattering by wall thinning can be described through an acoustic model based on the dispersion characteristics of Lamb waves [34, 36]. The phase velocity of Lamb waves depends on the product of signal frequency, with plate thickness. This dependence is shown in Fig. 2.5. For a selected mode and frequency, it is postulated that the interaction of the probing guided wave with a region of reduced wall thickness can be modeled as the perturbation experienced by an acoustic pressure wave

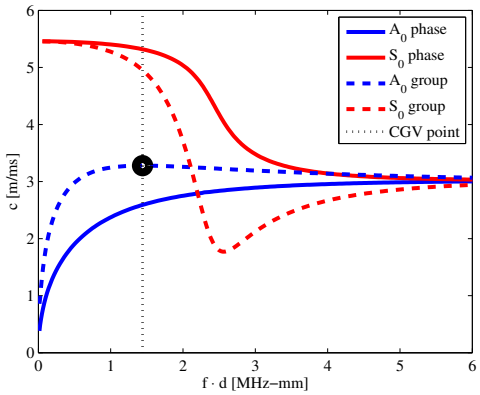

Figure 2.15: The fundamental flexural (A_0) and extensional (S_0) phase velocity and group velocity dispersion curves of Lamb waves in a steel plate are shown. The large black dot shows the maximum of the A_0 group velocity. The dotted black vertical line shows that the maximum occurs at $f \cdot d \approx 1.4$ MHz-mm, which is termed the CGV point.

propagating in a medium with non-uniform sound speed. The sound speed distribution is derived from the defect depth profile by evaluating the frequency-thickness product at each point inside the defect and determining the corresponding phase velocity from the mode dispersion curve. For instance, the A_0 mode slows down as it enters the defect since its phase velocity dispersion curve increases with frequency-thickness monotonically. Thus, for a wave pulse of known frequency traveling in a plate, a measurement of the traveltime and path length can be used to find the group velocity, and by extension determine the thickness. In practice, to make use of dispersion one would use a narrow band pulse (i. e. a pulse consisting of a tight grouping of frequencies) so that each frequency component of the signal travels at approximately the same velocity, and thus the pulse distortion effect is minimized. This allows a simple measurement of traveltime to be used to indicate the presence of WTL.

Complications arise for some frequency-thickness products which support the propagation of multiple modes with nearly the same velocity. For instance, when considering the A_0 and S_0 modes propagating in a plate, their phase velocities tend to the same asymptotic value as the frequency-thickness product increases, as shown in Fig. 2.15. In addition, for

high frequency-thickness product values many different modes can propagate simultaneously leading to complex waveforms containing multiple overlapping wave pulses. In order to avoid multiple modes of propagation occurring, one solution is to excite the zero order modes, below the cutoff frequency-thickness product with the smallest value. Thus, the low frequency-thickness product region of the zero order modes is focused on.

Assuming that all pipes analyzed will have a sufficiently low ratio of thickness to inner radius such that their dispersive characteristics can be approximated by those in a plate leaves only SH_0, A_0, and S_0 as candidate guided waves to be used in GWT. The benefit of WTL corresponding to a change in phase or group velocity is lost for the SH_0 mode, because its phase velocity is independent of frequency. For this reason it will not be appropriate for GWT. Moving on, the A_0 and S_0 modes are dispersive, and thus their group and phase velocities will be sensitive to changes in wall thickness. In addition, A_0 and S_0 have different group and phase velocities for lower frequency-thickness products, such that they should not overlap. For these reasons, A_0 and S_0 are both viable guided wave modes for the detection of WTL.

When comparing the A_0 and S_0 dispersion curve characteristics in the low frequency-thickness product region, it is important to keep in mind the intended use of the selected mode as a probe to detect WTL. This makes it imperative to choose a mode that links thickness to phase or group velocity with the greatest amount of sensitivity possible. Given this, it is noticed when comparing the phase velocity dispersion curves, shown in Fig. 2.15, that the S_0 phase velocity curve plateaus as the frequency-thickness product approaches zero. This implies a loss of sensitivity to WTL for deep defects. Conversely, the A_0 has an increasing slope as frequency-thickness product decreases. Thus, the sensitivity of A_0 to WTL will be greater than that of S_0.

Furthermore, Fig. 2.15 shows that the A_0 phase velocity curve is monotonically increasing, in a frequency-thickness product region where its group velocity is at a maximum (around 1.4 MHz-mm in steel) and with fairly constant value over a range of frequency-thickness

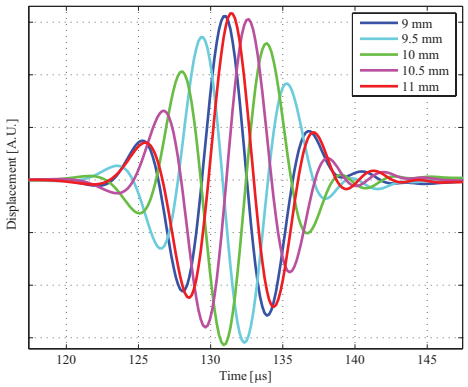

Figure 2.16: The effect of dispersion on a three-cycle Hann-windowed A_0 wave pulse with 160 kHz center frequency that has propagated 400 mm is shown in plates of different thicknesses. Because each of the frequency-thickness products shown are near the CGV point, the envelope of the pulse is relatively stable for different plate thicknesses.

products. The frequency-thickness product that corresponds to the maximum A_0 group velocity is the CGV point which is a key concept defined in the previously mentioned CGV method [27]. The benefit of operating at a frequency-thickness product region near the CGV point is observed in Fig 2.16. It shows a pulse that has propagated 400 mm from the source to the receiver for various plate thicknesses and the same frequency. In spite of the change in plate thickness, the wave group is received at the same time, with nearly the same envelope. However, the phase of the signal changes significantly with respect to the change in plate thickness. Ultimately, operating at the CGV point has the effect of allowing the arrival time of the pulse to be predicted without knowledge of the actual wall thickness, and minimizing the pulse distortion due to dispersion.

Up to this point, the pipes have been analyzed as if they were in a vacuum, but their intended use in pipelines will have them transmitting oil or gas. In the case of gas transmission, the vacuum approximation is appropriate due to the low impedance of gas compared to steel, but when transmitting oil, the effect of liquid loading must be considered. The guided waves are said to *'leak'* energy into fluid, as a result of the boundary conditions between the fluid and the pipe surface. Both A_0 and S_0 have displacement in the direction normal to the surface, shown in Fig. 2.6. This displacement causes a wave to be generated in the liquid,

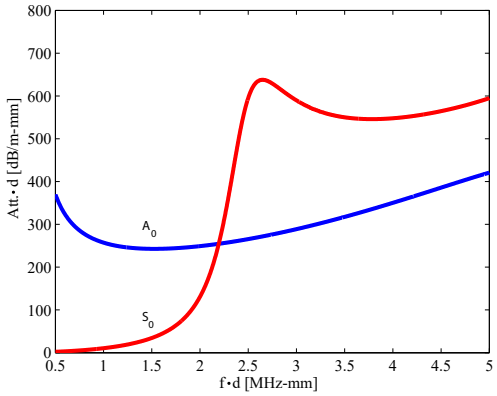

Figure 2.17: The fundamental flexural (A_0) and extensional (S_0) attenuation dispersion curves of Lamb waves in a 1 mm thick steel plate bounded by a water half space above, and vacuum half space below are shown. In the region near the CGV point ($f \cdot d \approx 1.4$ MHz-mm) the attenuation of A_0 is significantly higher than that of S_0.

which results in the loss of energy of the guided wave. The attenuation curves of A_0 and S_0 for a steel 1 mm thick plate with a water half space on one side, and vacuum on the other are shown in Fig. 2.17. It is clear that the attenuation value of A_0 is larger than that of S_0 at the CGV point. Nevertheless, the benefits of the superior sensitivity of A_0 to wall thickness cannot be ignored, and so it is chosen as the mode which will be used as the probing wave in the following implementation of GWT.

2.4 Summary

This chapter has reviewed the properties of guided ultrasonic wave propagation in plates and pipes, as well as their relationship to one another. It has been observed, that the dependence of curvature with propagation direction causes anisotropy since phase and group velocity vary with curvature. However, when the thickness is small compared to the inner radius of the pipe ($\eta \leq 0.1$) the velocity dependence on curvature is negligible and the acoustic sound speed map can be approximated using phase velocity values of Lamb waves propagating in plates. The dependence of dispersion curves on the frequency-thickness product provides

a means to determine wall thickness from the measured phase velocity of a mode. Due to dispersion and the presence of multiple propagating modes, guided wave signals can be highly complex. It is therefore necessary to identify suitable inspection parameters that limit the adverse effects of such complexity. The use of the fundamental flexural mode (A_0) at an operating frequency-thickness product near the CGV point provides an optimal configuration that maximizes sensitivity to WTL whilst minimizing the effect of group velocity dispersion and limiting the presence of unwanted high order propagating modes.

Chapter 3

Theory of high resolution GWT in pipes

3.1 Theory

In order to reconstruct wall thickness maps from guided wave transmission signals, it is necessary to formulate an inverse problem which can interpret the information contained in the ultrasonic waveforms and translate it into a representation of the defect's geometry. To this end, a forward model is used to describe how the probing waves interact with the defect and to provide the inversion scheme with the *'key'* to decode the defect geometrical information from the measured ultrasonic signals. The forward model and inversion scheme are discussed next.

3.1.1 Forward model

The aim of this section is to model the propagation of guided waves between the transducers of the transmit and receive arrays. For this purpose it is observed that a pipe can be represented by the surface of a circular cylinder, Σ, and a function $d(P)$ providing the wall thickness, d, at any point, P, on Σ. In the 3-D Euclidean space with Cartesian coordinates

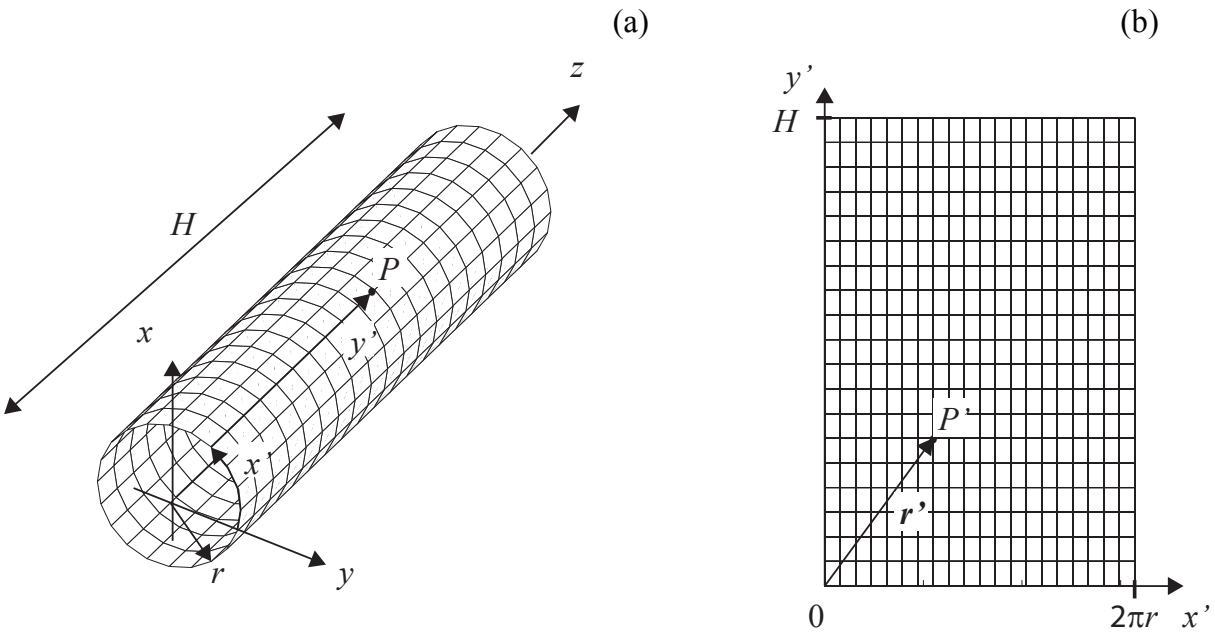

Figure 3.1: Coordinate systems used to form the parameterization of a circular cylinder. (a) 3-D physical space; (b) 2-D acoustic domain.

$\{O, x, y, z\}$, the position of P is uniquely determined by a vector, $\mathbf{r} \in \mathbb{R}^3$, of coordinates (x, y, z). In order to provide 2-D representation of guided wave propagation and scattering, the 3-D surface can be unwrapped using the parametric equations

$$x = r \sin \frac{x'}{r}, \; y = r \cos \frac{x'}{r}, \; z = y', \quad \forall (x', y') \in [0 \quad 2\pi r] \times [0 \quad H] \tag{3.1}$$

where r is the average pipe radius across the thickness and H is the length of pipe section as shown in Fig. 3.1. Equations (3.1) are written with reference to the Cartesian coordinate system $\{O', x', y'\}$, in which the position of a point P' is uniquely determined by the vector $\mathbf{r}' \in \mathbb{R}^2$ of coordinates (x', y'). Moreover, they map a point $P' \in [0 \quad 2\pi r] \times [0 \quad H]$ onto one and only one point $P \in \Sigma$. In a more compact vectorial notation Eqs. (3.1) can be expressed as

$$\mathbf{r} = \mathbf{r}(\mathbf{r}') \quad \forall \mathbf{r}' \in \Omega, \tag{3.2}$$

where $\Omega = [0 \quad 2\pi r] \times [0 \quad H]$. Note that throughout the chapter the prime sign is used to refer to quantities in the 2-D domain.

The acoustic model is formulated assuming that the influence of wall thinning on the propagation of guided waves can be modeled by a phase velocity field defined as

$$c(\mathbf{r}) = c_{ph}[f \cdot d(\mathbf{r})], \quad \forall \mathbf{r} \in \Sigma, \tag{3.3}$$

where $c_{ph}(\cdot)$ is the dispersion function of the selected Lamb mode and $d(\mathbf{r})$ is the thickness distribution along the pipe. As a consequence, the velocity field in the 2-D domain is obtained by assigning to each point $P' \in \Omega$ the value of phase velocity associated with its corresponding point $P \in \Sigma$ i. e.

$$c'(\mathbf{r}') = c_{ph}\{f \cdot d[\mathbf{r}(\mathbf{r}')]\}, \quad \forall \mathbf{r}' \in \Omega. \tag{3.4}$$

The velocity field in Eq. (3.4) is then used to define a 2-D acoustic medium in which guided wave scattering reduces to acoustic scattering described by a scalar potential $\phi(x', y', f)$ solution to the inhomogeneous Helmholtz equation [63]

$$\nabla^2\phi(x', y', f) + k_0^2\phi(x', y', f) = -4\pi O_H(x', y', f)\phi(x', y', f), \tag{3.5}$$

where $k_0 = 2\pi f/c_0'$ is the background wavenumber dependent on the background velocity $c_0'(f) = c(fd_0)$, with d_0 being a reference thickness, e.g. the thickness of the undamaged pipe. $O_H(x', y', f)$, is the object function given by

$$O_H(x', y', f) = \frac{k_0^2}{4\pi}\left[\left(\frac{c_0'(f)}{c'(x', y', f)}\right)^2 - 1\right], \tag{3.6}$$

and is the acoustic representation of the WTL; $O_H(x', y', f)$ vanishes outside the damage area. The high-frequency asymptotic form of Eq. (3.5) leads to the ray theory of geometrical

acoustics described by the eikonal equation

$$\left(\frac{\partial \tau}{\partial x'}\right)^2 + \left(\frac{\partial \tau}{\partial y'}\right)^2 = O_e^2(x', y'), \tag{3.7}$$

where the function $\tau(x', y')$ is the traveltime of the acoustic wave to point (x', y') and the object function $O_e(x', y')$ is now defined as the slowness

$$O_e(x', y') = \frac{1}{c'(x', y')}, \tag{3.8}$$

where $c'(x', y')$ can refer to the phase velocity at the center frequency of the wave pulse or its group velocity at the same frequency depending on whether the propagation of the signal phase or energy is to be considered.

The parametric representation (3.1) and Eqs. (3.5) and (3.6) or their asymptotic counterpart (3.7) and (3.8), constitute the mathematical expression of the forward model. The model can be used to describe guided wave propagation from the transducers of the transmit array to those of the receive array. With reference to Fig. 3.2(a) the two arrays can be represented by two closed curves Γ_T and Γ_R, each of length L, and delimiting a section of pipe with lateral surface σ. Using the coordinate system (x', y') shown in Fig. 3.2(a), σ maps onto the 2-D domain $\Omega = [0 \quad L] \times [0 \quad D]$, where D is the distance between Γ_T and Γ_R.

Guided wave propagation from a point source T to a point receiver R on the pipe is modeled by solving Eq. (3.5) in the Ω domain for a point source T_0' and a receiver R_0', T_0' and R_0' being images of T and R, respectively. As an example, the direct wave-path from T to R, Γ_0, can be obtained by applying mapping (3.2) to wave-path Γ_0' which in the Ω domain joins T_0' and R_0'. In the absence of damage, the velocity model is uniform, $c'(\mathbf{r}') = c_0'$, and therefore Γ_0' is the straight segment joining T_0' to R_0'; this path results in the shortest traveltime of both phase and group and thus satisfies Fermat's principle. Applying the isometric mapping (3.1) to Γ_0' leads to a helical wave-path Γ_0 with the same length as Γ_0' and therefore resulting in the shortest traveltime from T to R.

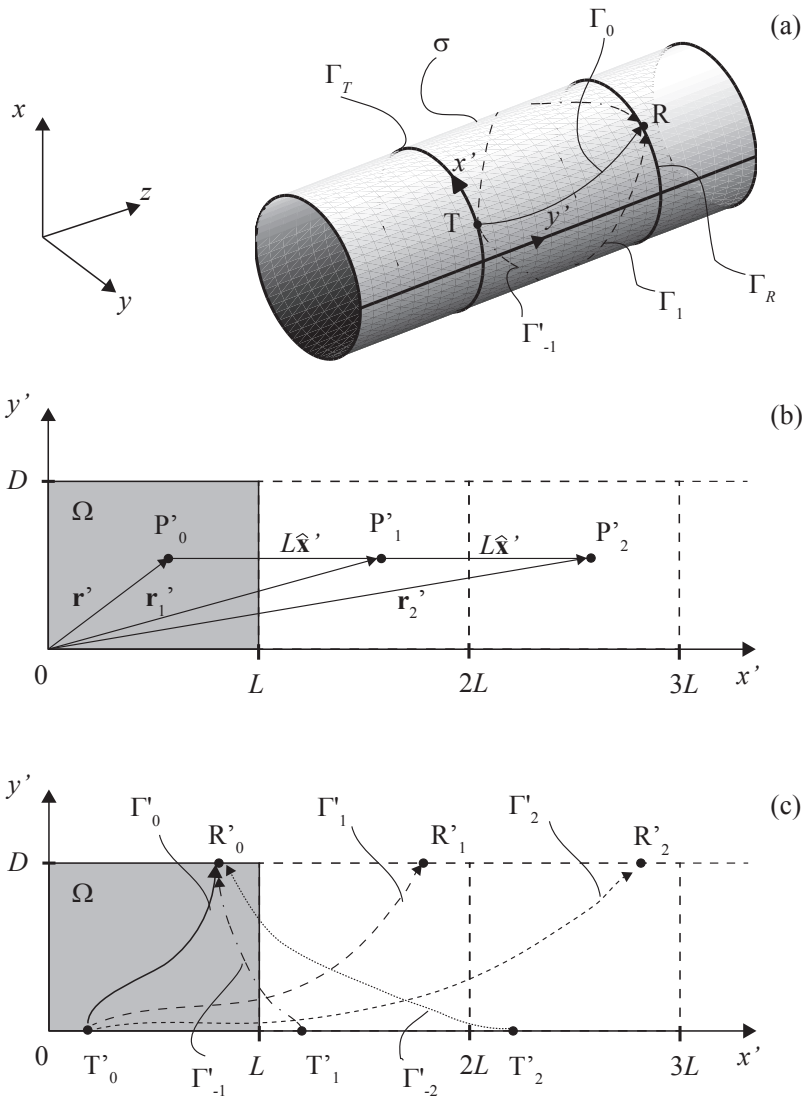

Figure 3.2: Replication method used to describe wave-paths wrapping around a pipe. (a) 3-D physical model showing the position of a point source (T) and receiver (R) and the corresponding first three wave-paths Γ_0, Γ_1, and Γ_{-1}; (b) Extended acoustic domain Ω_∞ showing the dependence of $\mathbf{r}'_n$ on $\mathbf{r}'$ for the first two replicas; (c) Acoustic wave-paths corresponding to the guided wave-path on the surface σ.

In order to describe the higher-order helical modes, it is sufficient to extend the Ω domain to infinity by connecting replicas of Ω. As a result, for any point $P' \in \Omega$ with position vector $\mathbf{r}'$ there exist an infinite number of points in the extended domain Ω_∞, with the point P'_n

belonging to the n-th replica being defined by the position vector

$$\mathbf{r}'_n = \mathbf{r}' + nL\hat{\mathbf{x}}', \tag{3.9}$$

where $\hat{\mathbf{x}}'$ is the unit vector parallel to the x'-axis as illustrated in Fig. 3.2(b). Equation (3.9) is used to extend the object function

$$\tilde{O}(\mathbf{r}'_n) = O(\mathbf{r}'_n - nL\hat{\mathbf{x}}'), \tag{3.10}$$

and to define a new parametric representation $\tilde{\mathbf{r}} : \Omega_\infty \to \sigma$ as

$$\tilde{\mathbf{r}}(\mathbf{r}'_n) = \mathbf{r}(\mathbf{r}'_n - nL\hat{\mathbf{x}}'), \tag{3.11}$$

where $\mathbf{r} : \Omega \to \sigma$ is the one-to-one mapping introduced earlier (3.2). By definition, mapping $\tilde{\mathbf{r}}(\mathbf{r}'_n)$ is no longer injective as infinite points in the Ω_∞ domain correspond to the same point on the surface σ.

As illustrated in Fig. 3.2(c), all the higher-order helical modes can be modeled considering the infinite replicas of T'_0, T'_n, and R'_0, R'_n, that can be generated from T'_0 and R'_0 with Eq. (3.9). As a result, the portion of the signal transmitted from T and measured at R and corresponding to the wave-path undergoing n turns around the pipe, Γ_n, can be obtained by solving (3.5) in the Ω_∞ domain with a point source in T'_0 and a point receiver in R'_n. The wave-path Γ_n is obtained by applying mapping (3.11) to the wave-path, Γ'_n, that joins T'_0 in R'_n in Ω_∞. Similarly, the wave-path Γ'_{-n} joining T'_n to R'_1 maps onto the wave-path Γ_{-n} that wraps n-times around the pipe but in the opposite direction of Γ_n. It should be observed that with the indexing used in this chapter the wave-path $\Gamma'_{\pm n}$ is obtained using transducer pairs whose relative distance along the $\hat{\mathbf{x}}'$ axis is comprised between $(n-1)L$ and $(n+1)L - L/N$ where it is assumed that $n > 0$ and the transmit and receive arrays consist of N equally spaced transducers each. Since a full turn corresponds to a relative distance

along the $\hat{\mathbf{x}}'$ axis equal to L, $\Gamma'_{\pm n}$ is associated with wave-paths that perform between $n-1$ and n full turns plus a fraction up to $(N-1)L/N$. In the remainder of this chapter, the expression n-th order helical mode is used to refer to the family of wave-path $\Gamma'_{\pm n}$.

An explicit expression can be given for the path lengths in the presence of a uniform velocity model. In this case the paths Γ'_n and Γ'_{-n} are straight segments and the path length of the n-th order mode from the q-th transmitter to the p-th receiver can be expressed as

$$\Gamma_n(p,q) = D\sqrt{1+\left(\frac{L}{D}\right)^2\left(n+\frac{p-q}{N}\right)^2}, \tag{3.12}$$

where n can now be any integer number.

3.1.2 Virtual arrays

The replication process described by Eq. (3.9) and used to expand the Ω domain is central to the resolution enhancement of GWT by higher-order helical modes. It can be observed that neglecting higher-order helical modes is equivalent to considering acoustic wave propagation in the Ω domain where there are N transmitters and N receivers. However, if the information associated with the helical modes up to order m ($|n| \leq m$) is included, the domain Ω has to be replicated m times to describe these higher-order wave-paths. As a result, also the transmit- and receive-arrays are replicated m times leading to two *'virtual'* arrays each with $N \times (m+1)$ transducers and greater aperture $L \times (m+1)$. Hereafter, the N-element arrays in the Ω domain are referred to as the physical arrays.

Although including higher-order modes increases the effective aperture of the physical arrays, some of the information yielded by the replication process is redundant. The redundant components can be examined by formatting the virtual array data into a square information matrix $\mathbb{U}$ of dimension $N(m+1) \times N(m+1)$ whose ji-th entry is the information associated with the signal traveling from the i-th transmitter to j-th receiver of the virtual arrays. Here, information refers to one or more characteristics of the signal such as the traveltime

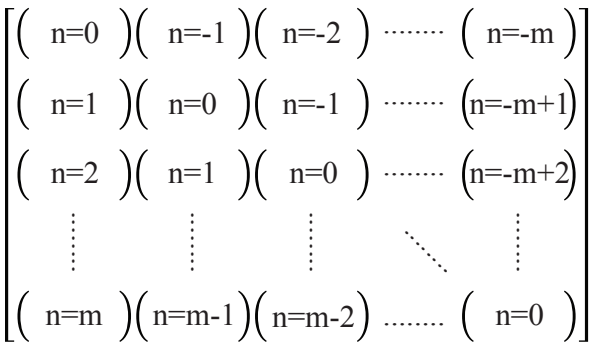

Figure 3.3: Block structure of the information matrix. The sub-matrices have dimension $N \times N$ and correspond to different combinations of the sub-apertures of the transmit and receive virtual arrays.

or a complex Fourier component at a selected frequency. Due to the structure of the Ω_∞ domain, the matrix has a block structure formed by $N \times N$ sub-matrices each containing all the transmit-receive combinations that can be formed with N-element sub-apertures of the transmit and receive virtual arrays. In general, the sub-matrix in the j-th block row and i-th block column corresponds to the $i-1$ replica of the physical transmit array and the $j-1$ replica of the physical receive array and is associated with a specific order n as shown in Fig. 3.3. The sub-matrix on the top-left corner is obtained considering the transmit and receive physical arrays only. The matrix therefore contains the same information that would be available if the higher-order helical paths were neglected, i. e. $n = 0$. The other sub-matrices along the leading diagonal also correspond to $n = 0$ since they represent the information obtained when transmitting and receiving with the n-th replicas of the physical transmit and receive arrays. The first block column of $\mathbb{U}$ includes the matrices obtained transmitting with the physical transmit array and receiving with all the replicas of the physical receive array. Each of the following columns is obtained by switching the transmit array to the next replica and leads to a total of $2m+1$ independent block matrices as shown in Fig. 3.3. As a result, the total number of independent information entries is $N^2(2m+1)$ which is greater than the information available without considering the high-order helical modes by a $(2m+1)$ factor. This additional information is exploited to ameliorate the resolution of GWT.

3.1.3 Inversion

The purpose of the inversion is to reconstruct the WTL map from the data contained in the information matrix $\mathbb{U}$. The numerical formulation of the inverse problem starts from the discretization of the propagation domain into a grid of nodes where relevant field functions such as the wave potential, $\phi(\mathbf{r}')$, or traveltime, $\tau(\mathbf{r}')$, are defined. For a grid containing l nodes, $\phi(\mathbf{r}')$ and $\tau(\mathbf{r}')$ can be represented by $l \times 1$ vectors, $\boldsymbol{\phi}$ and $\boldsymbol{\tau}$, so that the i-th entry of each vector defines the corresponding field function at the i-th node of the grid. Similarly, the object function $O(\mathbf{r}')$ can be represented by a $p \times 1$ vector of parameters, $\mathbf{o}$. For instance, assuming that $O(\mathbf{r}')$ is uniform inside each element of the grid, the i-th entry of $\mathbf{o}$ will correspond to the average value of $O(\mathbf{r}')$ inside the i-th element. Re-arranging the columns of the matrix $\mathbb{U}$ into a single vector $\mathbf{u}_m$, the inverse problem attempts to find the solution $\mathbf{o}$ to the set of nonlinear equations

$$\mathbf{u}_m = \mathbf{F}(\mathbf{o}), \tag{3.13}$$

where $\mathbf{F}$ represents the forward model either described by the Helmholtz equation (3.5) or the eikonal equation (3.7) depending on the desired level of accuracy. Once $\mathbf{o}$ is determined, the spatial distribution of the guided wave phase velocity, $c'(\mathbf{r}')$, is obtained by inverting Eq. (3.6). From $c'(\mathbf{r}')$ the residual wall thickness is found from the phase velocity dispersion curve of the selected guided mode which is used to map the values $c'(\mathbf{r}')$ to the corresponding $f \cdot d(\mathbf{r}')$ products and hence $d(\mathbf{r}')$ since the frequency is fixed. The most critical step in this process is the solution of the inverse problem (3.13) which is ill-posed in the sense of Hadamard [64]. The ill-posedness is a consequence of the instability of the inverse problem due to the solution not being a continuous function of the input data [41]. As a result, small errors in the data caused by noise and other experimental uncertainties can lead to large artifacts in the reconstructed object function. Moreover, under the limited view configuration the solution is not unique meaning that different defect geometries can correspond to the

same measured dataset [38].

Since the introduction of regularization methods for ill-posed problems by Tikhonov in 1963 [65], inversion of wave data has extensively been studied in many fields with major advances in geophysics and optics made possible by progress in computer power. To illustrate the main aspects of the inversion it can be observed that the forward problem defined by Eq. (3.5) can be expressed as

$$\boldsymbol{\phi} = \mathbf{G}_H(\mathbf{o})\mathbf{f}, \tag{3.14}$$

where $\mathbf{f}$ is an $l \times 1$ vector representing point sources at the nodes of the grid and $\mathbf{G}_H$ is the set of approximate Green's functions so that the ij-th entry of $\mathbf{G}_H$ is the field observed at the i-th node when a point source radiates from the j-th node, see for instance [66]. Importantly, Green's functions are calculated in the inhomogeneous background and take into account the distortion that the wavefront radiating from the source undergoes as it travels through the inhomogeneous medium defined by $\mathbf{o}$. A similar expression is obtained under the ray approximation where the solution to the eikonal equation (3.7) can be represented as

$$\boldsymbol{\tau} = \mathbf{G}_e(\mathbf{o})\mathbf{o}. \tag{3.15}$$

$\mathbf{G}_e$ contains the lengths of the ray paths to all the nodes of the grid from a single source position since under the eikonal model the object function is defined as the slowness. In particular, the ij-th entry of $\mathbf{G}_e$ is the length of the ray segment intersecting the j-th element and reaching the i-th node. Finally, it should be emphasized that the dependence of $\mathbf{G}_e$ on $\mathbf{o}$ is included to account for ray bending due to refraction effects in non-homogeneous media.

The forward models provided by Eqs. (3.14) and (3.15) can be used to predict the Fourier components and traveltimes measured by the arrays for a known object function and lead to a synthetic data vector, $\mathbf{u}_s$. The objective of the inversion is to determine the vector $\mathbf{o}$

by minimizing the residual between the measured and predicted data

$$\delta \mathbf{u} = \mathbf{u}_m - \mathbf{u}_s, \tag{3.16}$$

This is usually achieved in a least-squares sense minimizing the cost function based on the L^2-norm of the residual

$$E(\mathbf{o}) = \frac{1}{2}\delta \mathbf{u}^T \delta \mathbf{u}^*, \tag{3.17}$$

where the superscripts T and $*$ refer to the matrix transpose and complex conjugate, the latter being irrelevant when considering traveltimes. The minimization requires the use of iterative techniques such as gradient, Newton, or Gauss-Newton methods [67]. Among these, gradient methods are more computationally efficient when the number of parameters in $\mathbf{o}$ is large, and therefore they are widely used in inverse scattering problems. In particular good convergence rates are obtained with the nonlinear conjugate gradient method which starts from an initial guess of the object function $\mathbf{o}_0$ and defines the object function at the $k+1$ iteration step as

$$\mathbf{o}_{k+1} = \mathbf{o}_k + \alpha_k \boldsymbol{\delta}_k, \tag{3.18}$$

where α_k is the step size obtained from a line search that minimizes the cost function $E(\mathbf{o})$ along the descent direction $\boldsymbol{\delta}_k$ i. e.

$$\alpha_k = \arg\min_{\alpha}\{E(\mathbf{o}_k + \alpha \boldsymbol{\delta}_k)\}. \tag{3.19}$$

In the steepest descent method, $\boldsymbol{\delta}_k$ is chosen to be opposite to the gradient of the cost function, i. e. $\boldsymbol{\delta}_k = -\nabla E(\mathbf{o}_k)$. On the other hand, more rapid convergence is obtained using

a different descent direction given by

$$\boldsymbol{\delta}_{k+1} = -\nabla E(\mathbf{o}_{k+1}) + \beta_k \boldsymbol{\delta}_k, \tag{3.20}$$

where β_k is the conjugate gradient update parameter. Various formulas for β_k have been proposed [68], in this implementation the Fletcher-Reeves formula

$$\beta_{k+1} = \frac{\|\nabla E(\mathbf{o}_{k+1})\|^2}{\|\nabla E(\mathbf{o}_k)\|^2}, \tag{3.21}$$

is adopted. Each iteration step requires knowledge of the partial derivatives $\partial E/\partial o_i$ which form the gradient ∇E. Direct computation of the derivatives is highly inefficient since the large number of parameters in $\mathbf{o}$ would require the computation of a vast number of forward models. However, this is not necessary as the gradient can be calculated by back-projecting the residual $\delta\mathbf{u}$.

When using the full wave model (3.14), the gradient is derived from the wavefield generated by N virtual sources coincident with the receiver positions and with the amplitude of the i-th virtual source proportional to the conjugate of the residual δu_i^* [69]. The conjugation of the residual is equivalent to the time reversal operation [70] in the time domain thus implying that the residual is back-propagated into the medium. Similarly, under the ray approximation, the gradient is evaluated by back-projecting the residual along the rays that join the source to the receivers as in the filtered back-projection method [42] used in computerized tomography. As a result, calculation of the gradient can be achieved with the computation of a single forward model for both the full wave and ray based models.

The block diagram shown in Fig. 3.4 summarizes the steps involved in the iterative solution to the inverse problem. At the beginning of the iteration, an initial guess for the object function map, $\mathbf{o}_0$, is passed to a forward solver that predicts the synthetic dataset $\mathbf{u}_s$ using the finite element or finite difference method to calculate the matrix $\mathbf{G}_H$ in Eq. (3.14) or ray tracing techniques to obtain $\mathbf{G}_e$ in Eq. (3.15). The synthetic and measured data are

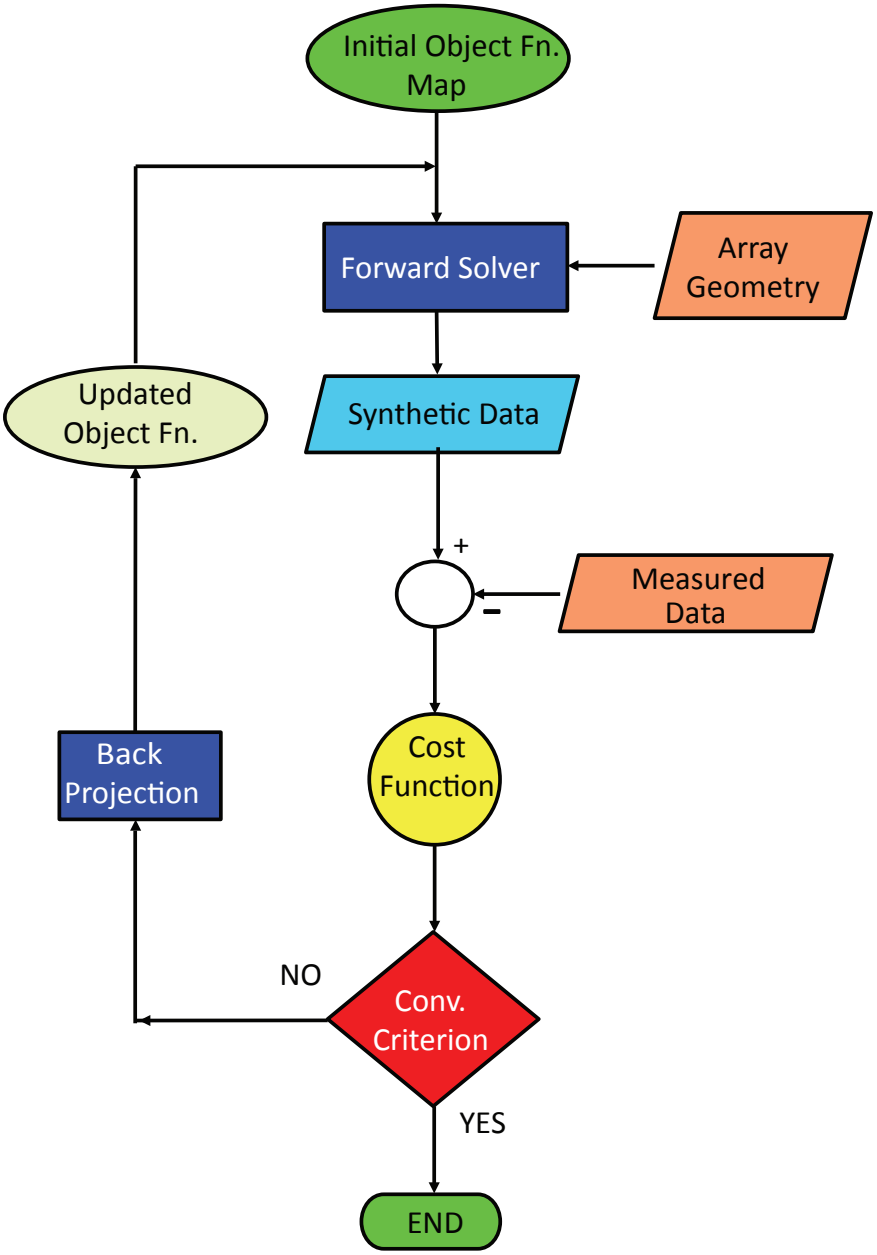

Figure 3.4: Block diagram of the iterative algorithm used to solve the inverse problem.

then used to compute the residual $\delta\mathbf{u}$ and evaluate the cost function E. If E does not meet the convergence criterion, the object function is updated computing its gradient ∇E and using the recursive expressions (3.18)-(3.21) until convergence is achieved. The convergence criterion is typically based on a threshold level applied to the cost function or its slope. Here, the latter is used as discussed at the end of Sec. 3.2.

To address the instability of the inverse problem and ensure the convergence of the iteration the cost function in Eq. (3.17) is modified by adding a regularization correction

$$E_{reg}(\mathbf{o}) = \frac{1}{2}\delta\mathbf{u}^T\delta\mathbf{u}^* + \frac{1}{2}\gamma^2\|\mathcal{D}\mathbf{o}\|^2, \tag{3.22}$$

where γ is a regularization parameter and $\mathcal{D}$ is a weighting operator. If $\mathcal{D}$ coincides with the identity operator the minimization of Eq. (3.22) is equivalent to the damped least-squares minimization.

For the GWT problem considered in this chapter additional regularization is sought based on the prior knowledge that corrosion and erosion damage can only cause the wall thickness to decrease and that the object function is replicated across the aperture of the virtual transmit- and receive-arrays according to Eq. (3.10). The first type of regularization is achieved by imposing phase velocity extrema. The phase velocity of a Lamb wave is a monotonic function of the $f \cdot d$ product as shown in Fig. 2.5 (a). For a Lamb mode whose phase velocity is an increasing function of $f \cdot d$, such as the A_0 mode, a WTL can only cause a reduction in phase velocity. In this case the regularization condition is $c'(x', y', f) \leq c'_0(f)$. Conversely, for a mode whose phase velocity decreases with $f \cdot d$, such as the S_0 mode, the regularization condition is $c'(x', y', f) \geq c'_0(f)$. Phase velocity extrema translate into object function extrema using Eq. (3.6) or (3.8) and can be imposed as search constraints in Eq. (3.19).

The second type of regularization is dependent on the maximum order of helical modes, m, used for the inversion. As discussed in Secs. 3.1.1 and 3.1.2 to account for all the helical modes up to the m-th order, the $\Omega = [0 \quad L] \times [0 \quad D]$ domain has to be expanded by adding m replicas leading to the extended domain $\Omega_e = [0 \quad mL] \times [0 \quad D]$. If l is the number of nodes used to discretize Ω, the total number of nodes in Ω_e is $l_e = (m+1)l$. Therefore from Eq. (3.10) $\mathbf{o}$ has the cyclic structure

$$\mathbf{o}_i = \mathbf{o}_{i+nl}, \quad 1 \leq i \leq l \quad 0 \leq n \leq m. \tag{3.23}$$

Condition (3.23) is imposed when updating the object function in Eq. (3.18).

In concluding this section it is observed that the resolution of the images obtained through the solution of the inverse problem is dependent on whether the inversion is based on the eikonal equation of ray theory or the more accurate Helmholtz equation. In the former case the inversion is referred to as traveltime tomography or curved ray tomography (CRT) [71], whereas in the latter instance as full-wave tomography (FWT). The resolution of CRT is dictated by the width of the first Fresnel zone, $\sqrt{\lambda a}$, where λ is the wavelength of the probing signal and a the average distance between transmit-receive pairs [72]. As a result, the resolution of CRT is typically lower than that achievable with full-wave tomography which can yield resolution as high as $\lambda/2$ or even greater if super resolution techniques are used [73]. Despite the lower resolution, CRT is currently the most widely used inversion technique in geophysical prospecting owing to its robustness and computational efficiency. In fact, CRT can invert data from relatively sparse arrays while FWT requires wavefields to be sampled at spatial intervals not greater than $\lambda/2$ according to Nyquist's criterion [74]. The Nyquist criterion can be difficult to meet in practical pipe monitoring configurations due to the transducer physical dimensions that limit the maximum number of transducer elements along a single ring array. In addition, the *'goodness'* of the object function initial guess is less critical on the convergence of CRT than FWT - in CRT the uniform sound speed model associated with the undamaged pipe is used as the initial guess. As a result, FWT and other more recent methods e.g. [36] use the reconstruction from CRT as the initial guess for the iteration. Finally, the eikonal equation can be solved using advanced ray tracing algorithms which are several orders of magnitude faster than the finite difference or element schemes used to solve the Helmholtz equation [75]. For these reasons the rest of the studies in this thesis will focus on CRT however it is understood that the results can be translated to FWT and other methods accounting for diffraction effects.

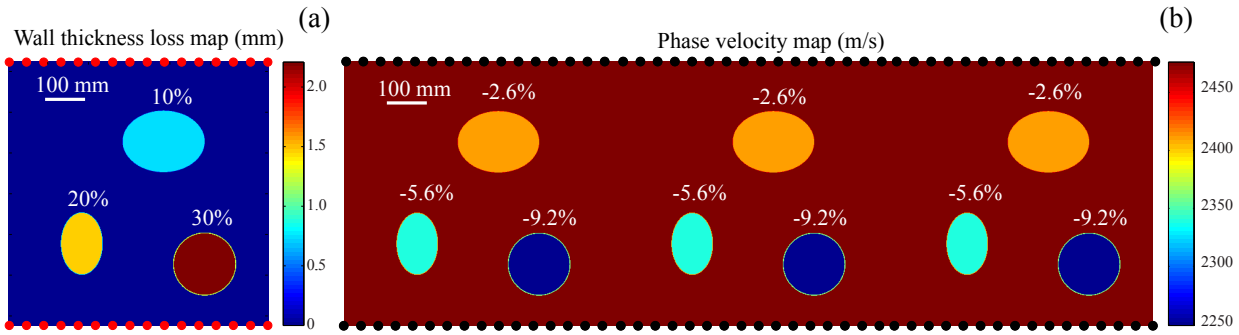

Figure 3.5: Model used for the numerical simulations. (a) WTL map; % values indicate wall loss relative to thickness; (b) Phase velocity model containing two replicas; % value indicate the phase velocity contrast. The red and black dots represent the position of the transducers of the transmit and receive arrays.

3.2 Numerical example

This section illustrates how the accuracy of maximum WTL estimations is improved by using the extended aperture of the virtual arrays. To simulate experimental datasets, a schedule 40, 8" diameter steel pipe with 215.50 mm outer diameter and 7.37 mm wall thickness was modeled using a two-dimensional acoustic finite difference (FD) model that solves the coupled first-order linear acoustic propagation equations, rather than the second-order wave equation given by Eq. (3.5) in the time domain. This formulation of FD uses first order finite differences in space and time carried out over a standard Yee grid [76].

The model contained one circular and two elliptical defects with depths ranging from 10 to 30% of the wall thickness with the absolute depth values given in Tab. 3.1 and the other geometrical characteristics shown in Fig. 3.5(a) which represents the unwrapped pipe. The

		Two		One		No	
	Nom.	Replicas	Error	Replica	Error	Replicas	Error
	(mm)	(mm)	%	(mm)	%	(mm)	%
10% Defect	0.74	0.80	0.85	0.70	-0.50	0.59	-2.00
20% Defect	1.47	1.30	-2.36	1.20	-3.72	0.93	-7.38
30% Defect	2.21	2.24	0.39	2.02	-2.59	1.51	-9.51

Table 3.1: Nominal and reconstructed defect depths for different numbers of replicas.

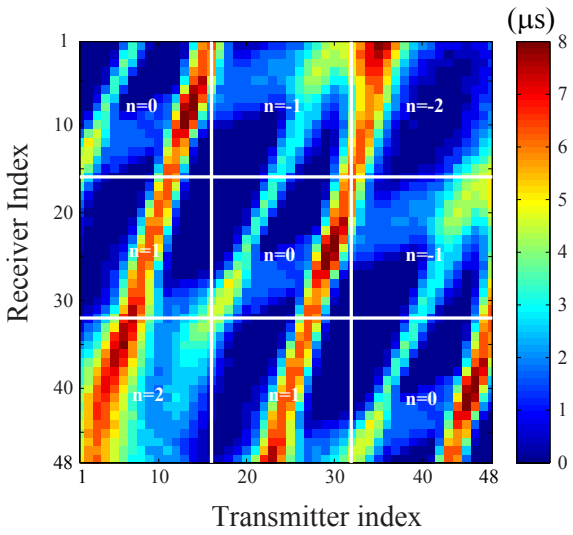

Figure 3.6: Simulated time delay matrix from the acoustic model in Fig. 3.5.

transmit- and receive-arrays each consisted of 16 transducers and were 646.50 mm apart which corresponds to three pipe diameters. The source transducers excited a five-cycle, Hann-windowed wave pulse centered at 160 kHz, i. e. $f \cdot d = 1.18$ MHz-mm. To simulate the propagation of the A_0 mode, the sound speed of the model background was set to $c_0' = 2476$ m/s which corresponds to the phase velocity of A_0 at $f \cdot d = 1.18$ MHz-mm according to the dispersion curves shown in Fig. 2.5 (a). Similarly, the defects were modeled by regions of lower phase velocity obtained from the corresponding $f \cdot d$ products. In addition, to model helical modes up to the second order two replicas were added leading to the sound speed map shown in Fig. 3.5(b) in which the virtual transmit- and receive-arrays now contained 48 transducers each. The domain was discretized into a grid of size 4668×1556 square elements 0.44 mm in size which corresponds to about 1/35th of the wavelength of A_0 at the center frequency, and the time step was 0.06 μs. Perfectly matched layers (PMLs) were introduced to suppress unwanted reflections from the edges of the model [77]. To simulate a full dataset the model was run 48 times and each time the wavefield measured at the 48 receivers was stored.

Figure 3.6 shows the traveltime information matrix $\mathbb{U}$ obtained by applying the zero-

crossing method to the time domain waveforms obtained from the FD simulations. The simulations did not include signal dispersion and therefore it was sufficient to track the position of the zero crossing closest to the signal envelope maximum. In reality due to dispersion, the signal phase moves relative to the envelope and ambiguity may arise when the phase shifts by more than one period. However, in continuous monitoring the ambiguity is overcome by continuously tracking the zero crossing as the defect depth increases.

Each pixel in the image corresponds to a particular transmit-receive pair with the color scale indicating the phase traveltime differences between the *'current'* signals measured in the presence of damage and the *'baseline'* signals measured for the undamaged structure. The dark blue pixels therefore correspond to wave-paths that do not intersect the defects while the dark red ones indicate the wave-paths most affected by the presence of damage. Due to the presence of two replicas in the model [see Fig. 3.5(b)], the matrix exhibits the block structure introduced in Sec. 3.1.2. Moreover, three sets of patterns similar to those observed in CT are present and correspond to the signatures from the three defects.

The traveltime matrix is used as an input for the iterative inversion scheme described in Sec. 3.1.3 based on the ray approximation and illustrated in the block diagram of Fig. 3.4. The image plane was discretized with a regular grid of square element 8 mm in size which is significantly coarser than the discretization used to simulate the measurements with the full-wave equation. The forward model was based on the shortest path ray tracing method [75] which provides the first-arrival traveltimes as well as the geometry of the ray paths - the latter is used for the back-projection within each iteration step.

The iteration starts using a uniform sound speed model $c_0' = 2467$ m/s as the initial guess. Figure 3.7(a) shows the reconstruction at the end of the first iteration which for convenience has been displayed as a map of WTL. Although the reconstruction provides an indication of the presence of the deepest defect the estimated maximum depth is grossly underestimated. As the iteration progresses, the maximum depth estimation improves and also the shapes of the shallower defects begin to be visible. After 18 steps the iteration converges to the map

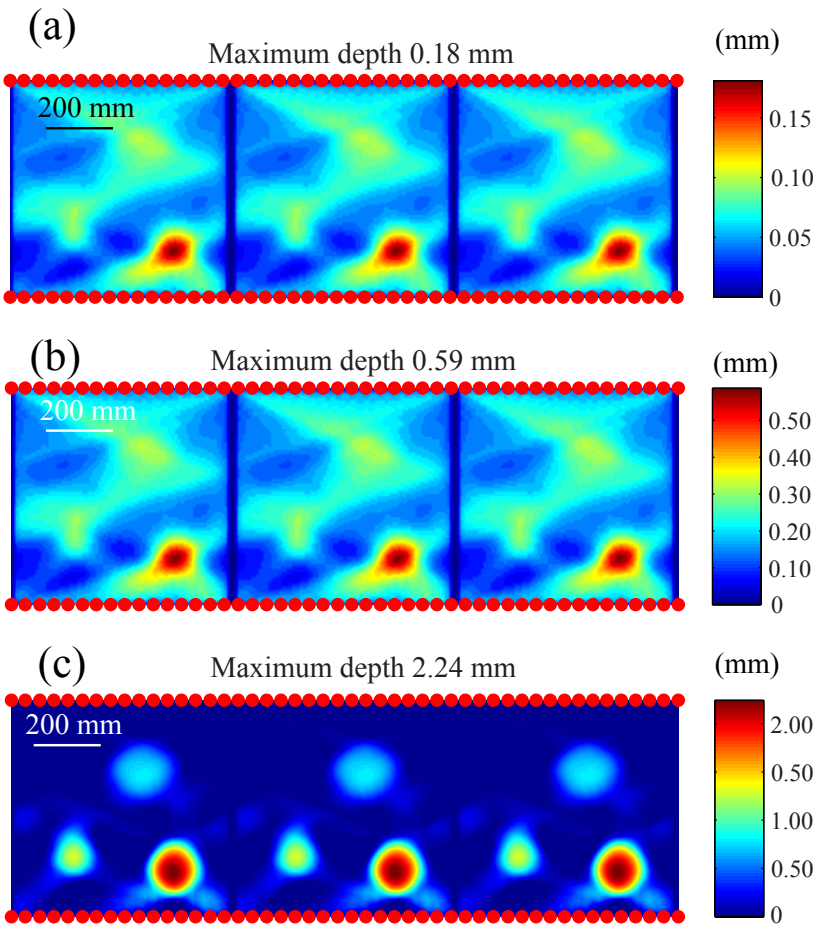

Figure 3.7: Examples of reconstructed WTL map at different steps of the iterative inversion: (a) At the end of the first step; (b) End of the third step; (c) End of iteration.

shown in Fig. 3.7(c) which provides accurate estimations of the defect depths as shown in Tab. 3.1 where also the depth estimation error relative to the wall thickness is given. For the deepest and shallowest defects the reconstruction overestimates the depth by less than 1%. On the other hand, the depth of the 20% defect is underestimated by 2.36%. This greater error is mainly due to shadowing effects from the neighboring defects combined with the orientation of the defect.

To examine the benefit of the replication process, Fig. 3.8 compares the reconstructions obtained considering two replicas as before, Fig. 3.8(a), one replica Fig. 3.8(b) and without replicas Fig. 3.8(c), the latter corresponding to the case in which higher-order helical modes

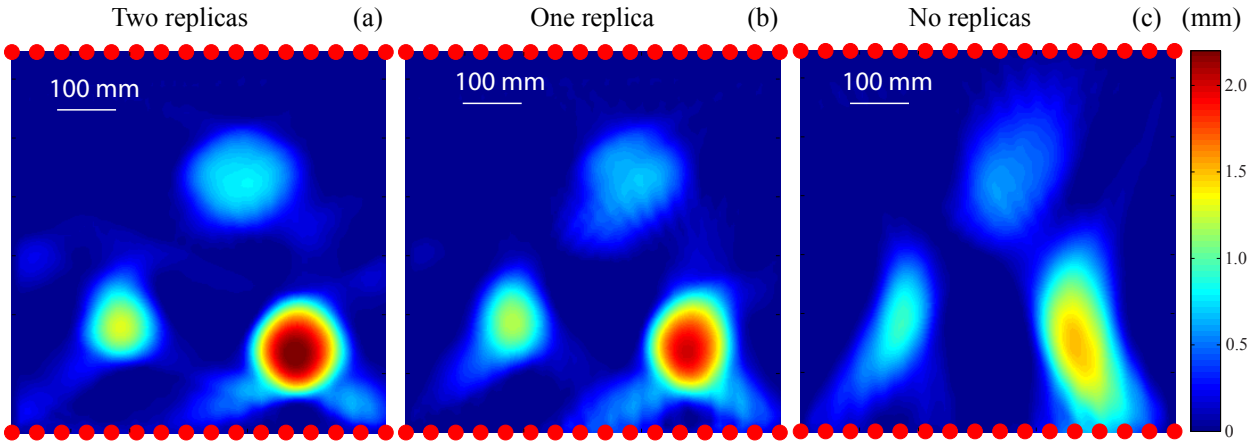

Figure 3.8: Benefit of higher-order helical modes. WTL maps obtained: (a) Using up to the second order helical modes; (b) Up to the first order; (c) Only considering the direct wave-paths.

are neglected. As expected, the larger aperture afforded by the virtual arrays over two replicas leads to the best reconstruction in terms of defect shapes and most importantly depth estimates, see Tab. 3.1. Without replicas, the defect shapes are highly distorted and the maximum depth is underestimated by almost 10%. The shape distortion is a well known consequence of the limited view problem that causes X-shaped artifacts radiating from the defect [78]. When the array aperture is small the artifacts are large and smear the defects as shown in Fig. 3.8(c). However, as the aperture increases the artifacts become weaker and cause little image distortion as shown in Fig. 3.8(a).

3.3 Conclusion

A general inversion method has been introduced to ameliorate the resolution of GWT by exploiting helical modes that circle around the pipe multiple times. It has been shown that the information carried by the modes that wrap around the pipe up to m times can be used to increase the effective array aperture by a $m + 1$ factor, thus leading to superior ray coverage and hence improved wall thickness estimation accuracy. Numerical simulations showed that using up to the second order helical modes is sufficient to reduce the maximum

depth estimation error from -10% to under 0.5% of the wall thickness.

Chapter 4

Parametric Uncertainties

In addition to the reconstruction errors caused by the limited view problem, another source of error can be attributed to uncertainties in the parameters of the forward model. These are termed parametric uncertainties, and refer to differences between parameters of the experimental setup and corresponding simulation parameters, such as pipe geometry, array geometry, assumption of background sound speed, etc.

This chapter introduces a twofold approach that is aimed at addressing both time independent parametric uncertainties (TIPUs) and time dependent parametric uncertainties (TDPUs). The approach is validated using experimental data obtained under conditions reproducing those encountered in field applications. The choice of experimental validation instead of numerical testing is dictated by the complexity of the numerical models that would be required to simulate the experimental conditions. Importantly, the fully 3-D nature of the simulations required limits the range of cases that can be studied due to excessive computational burden.

4.1 Experimental setup

Full-scale experimental validation was conducted on a schedule 40, 8" diameter (215.50 mm outer diameter and 7.37 ± 0.05 mm wall thickness) carbon steel pipe of 3000 mm length. Two

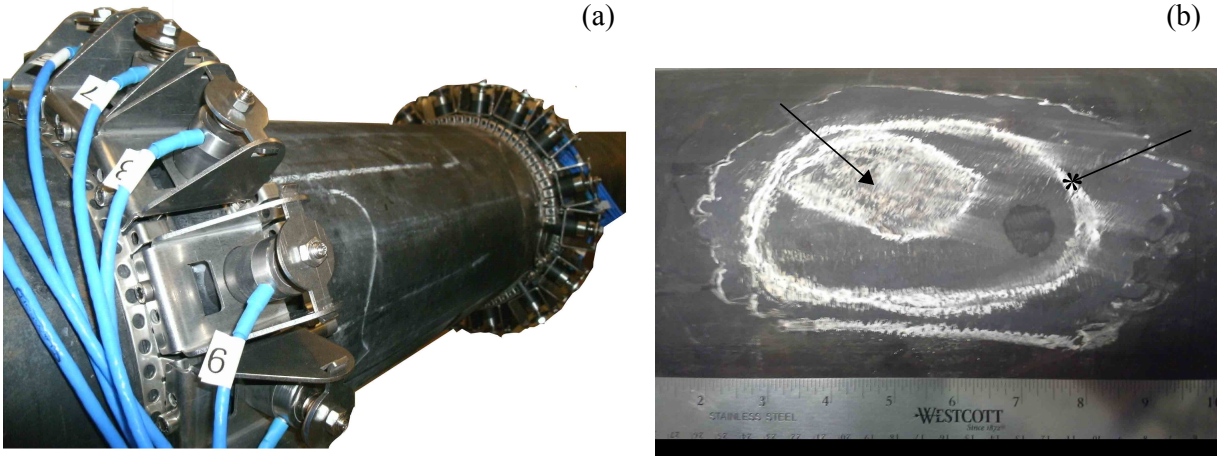

Figure 4.1: Experimental setup: (a) An 8" diameter pipe is instrumented with two ring arrays each containing 16 EMAT transducers; (b) Detail of the defect consisting of a deeper region pointed by the arrow and smooth transition zone starting along the contour indicated by the star arrow.

ring arrays of ultrasonic transducers were mounted 505 mm apart around the pipe center to minimize the effect of end reflections. Each array consisted of 16 Electromagnetic Acoustic Transducers (EMATs) held in position by a flexible metallic fixture clamped around the pipe as shown in Fig. 4.1(a). A major advantage of EMAT transducers is that they do not require direct contact to the pipe thus avoiding the need for couplant or bond layers. These are known to introduce signal instabilities with conventional piezoelectric transducers due to thermal sensitivity of the coupling medium and its material degradation with time. For optimal stability the transducers were spring loaded to ensure that the lift-off distance was not affected by structural vibrations. The transducers are designed for selective excitation and reception of the A_0 mode and minimize the coherent noise that would result from the propagation of S_0 in the same frequency range [28, 79]. The transducers were driven by a custom-made, 32-channel array controller which acquired the 16×16 transmit-receive combinations based on the electronic architecture described in [79]. The transducers were excited with a three-cycle wave pulse centered at 160 kHz. For each transmit-receive pair 256 averages were performed and the resulting signals were digitalized at 3 MHz sampling

(a) (b)

Figure 4.2: Temperature control setup: (a) The heater consists of four strands of heat tape wrapped helically around a 90 mm diameter, 2000 mm length steel pipe; (b) The insulated pipe/transducer setup is shown.

rate.

An irregular corrosion patch was simulated by manually angle grinding an area inside a rectangle that was 100 mm wide in the circumferential direction and 200 mm long in the axial direction, Fig. 4.1(b). The edges of the defect provided a gentle and smooth transition towards a smaller deeper region 50×50 mm^2 in size. A 20 MHz, fingertip probe 1/8" (3.2 mm) diameter was used to estimate the maximum defect depth which was found to be 0.78 mm or 10.6% of the wall thickness. Although the thickness measurement could be reproduced within $\pm$ 5 μm, the initial wall thickness was not know with the same level of precision, indeed due to loose manufacturing tolerance point-by-point wall thickness variations of $\pm$ 50 μm were observed on the intact pipe. This uncertainty should therefore be applied to the maximum depth estimation.

To investigate thermal stability, an internal heater consisting of a 90 mm diameter, 2000 mm length steel tube with four strands of heat tape wound in a helical pattern over its entire length was held concentric to the pipe, as shown in Fig. 4.2(a). A control system passed current through the heat tapes at regular intervals and for adjustable duty times that

allowed the temperature of the pipe to be continuously varied from room temperature up to 400°C. Shell insulation was applied to the pipe exterior to limit heat dissipation. The insulated experimental setup is shown in Fig. 4.2(b).

4.2 Mitigation of TIPU

TIPU result from poor manufacturing tolerances of the pipes and positioning errors of the array transducers. To address TIPUs a differential approach is proposed that is aimed at reconstructing the state of the pipe relative to a reference state rather than the absolute condition. The reference state is that of the pipe at the time of installation of the array system. Letting $\mathbf{u}_m^b$ be the dataset vector corresponding to the baseline state measured at the time of installation, and $\mathbf{u}_m^c$ be the dataset vector associated with the current state of the pipe, the measured differential dataset is defined as,

$$\Delta \mathbf{u}_m = \mathbf{u}_m^c - \mathbf{u}_m^b. \tag{4.1}$$

Previously, inversion was based on a minimization of a cost function E dependent on the residual between the absolute measured dataset and the synthetic one, given by

$$\delta \mathbf{u} = \mathbf{u}_m - \mathbf{u}_s. \tag{4.2}$$

With the differential approach a new residual based on differential measurements is introduced as,

$$\delta \mathbf{u}' = (\mathbf{u}_m^c - \mathbf{u}_m^b) - (\mathbf{u}_s^c - \mathbf{u}_s^b). \tag{4.3}$$

This new residual suppresses the TIPUs since it can be observed that the generic measured

dataset can be expanded as

$$\mathbf{u}_m = \hat{\mathbf{u}}_m + \mathbf{u}_T. \tag{4.4}$$

where $\hat{\mathbf{u}}_m$ is the portion of the measured data vector that would be collected if the experimental setup parameters matched the forward model input parameters exactly, and the portion of the data vector that is a result of the difference between the experimental and forward model setup is, $\mathbf{u}_T$. By neglecting second order effects it can be assumed that $\mathbf{u}_T$ is the same for the baseline and current datasets therefore by substituting Eq. (4.4) in Eq. (4.3) one obtains,

$$\delta\mathbf{u}' = (\hat{\mathbf{u}}_m^c - \hat{\mathbf{u}}_m^b) - (\mathbf{u}_s^c - \mathbf{u}_s^b), \tag{4.5}$$

for which it is seen that the effect of TIPUs have been eliminated.

4.3 Signal pre-processing and temperature TDPU compensation

As explained in Sec. 3.2 the inversion takes as an input the information matrix $\mathbb{U}$ that contains the traveltime differences between the current and baselines signals. In practice this requires the availability of robust methods to estimate the traveltimes from noisy signals and compensate for thermal variations which affect the arrival times. These two aspects are discussed in the next two sections.

4.3.1 Traveltime estimation

Figure 4.3 shows cascade plots of the baseline and current (with defect) signals measured across the 16 elements of the receive array when the sixth element of the transmit array

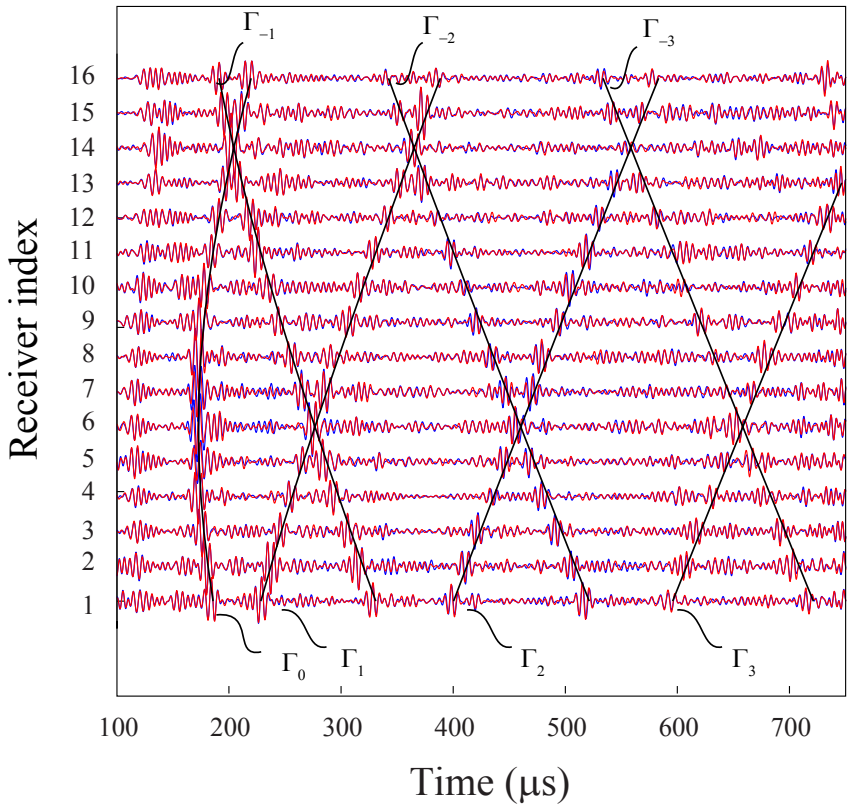

Figure 4.3: Waveforms measured across the transducers of the receive array when source # 6 radiates. The source is aligned with the defect and its effect on the transmitted signals is most evident among the direct arrivals measured with receivers # 5-6. (Red waveforms) baseline signals; (blue waveforms) current signals; (black curves) predicted group traveltimes for different helical paths.

(in line with the defect) is active; both datasets being measured at room temperature. The transducers of the transmit and receive arrays are labeled 1 to 16 in the clockwise direction with the i-th transmitter facing the i-th receiver. Each waveform shows the presence of multiple wavepackets arriving at different times and corresponding to helical modes that have performed up to three full turns around the pipe. The solid black curves are the traveltimes calculated dividing the path lengths in Eq. (3.12) by the group velocity of A_0 at 160 kHz (3270 m/s). The set of wavepackets arriving just after time t=100μs corresponds to a spurious S_0 mode excited by the transmitter together with the A_0 mode.

Recall that for steel, the group velocity dispersion curve of the A_0 mode exhibits a

maximum at the CGV point ($f \cdot d \approx 1.4$ MHz-mm) around which the group velocity remains almost constant with the $f \cdot d$ [27,28]. It was previously observed in Sec. 2.3 that for $f \cdot d$ near the CGV point a change in the plate thickness does not cause a significant group velocity variation. Thus the traveltime of the group is not affected by the presence of damage. This is consistent with Fig. 4.3 which is obtained for $f \cdot d$ =1.2 MHz-mm and where no discernible differences can be observed between the group traveltimes of the current and baseline signals.

In contrast with the group velocity, the phase velocity of A_0 varies almost linearly with the $f \cdot d$ in the same frequency range and indeed enables GWT estimations of depth. As a result, while the shape of the envelope of a transmitted signal is unaltered by the presence of damage, the shape of the signal within the envelope and in particular its phase are sensitive to the depth of the defect [27, 28].

The signal phase change represents the input for the inversion based on the ray model described by Eq. (3.7) with the object function (3.8) defined as the phase velocity slowness at the center frequency of the signal, i. e. 160 kHz.

To illustrate how the signals in Fig. 4.3 are processed to obtain the information matrix $\mathbb{U}$, the helical modes up to the second order are considered, following the numerical example studied in Sec. 3.2. Let $s_{ji}(t)$ be the signal measured with the j-th element of the receive array when the i-th element of the transmit array is active. According to the replication process described in Sec. 3.1.1 the signal will contribute to multiple entries in the $\mathbb{U}$ matrix. These are determined by considering all the replicas of the i-th transmitter and j-th receiver described by Eq. (3.11) with the $s_{ji}(t)$ signal therefore defining the $(j + nN, i + nN)$ entries of $\mathbb{U}$ for $n \in \{0, 1, 2\}$. The allocation of information from the signal to the matrix is performed by considering the distances $D_{j+nN,i+nN}$ between the virtual replicas of the selected transmit-receive pair. In particular, the entry $\mathbb{U}_{j+nN,i+nN}$ corresponds to the wavepacket of $s_{ji}(t)$ arriving at time

$$\tau = \frac{D_{j+nN,i+nN}}{c_{gr}}, \tag{4.6}$$

where c_{gr} is the group velocity. Expression (4.6) is used to center a window that is applied to $s_{ji}(t)$ to extract the wavepacket of interest. If no significant temperature variations occur between the baseline and current measurements, the group arrival is not changed by the presence of damage and the same window can be applied to both the baseline and current signals. In the presence of temperature fluctuations the group velocity in Eq. (4.6) changes and therefore the position of the window needs to be adjusted to the current temperature. To evaluate the phase traveltime the zero-crossing method [80] is applied to the windowed signal and the phase traveltime difference is then estimated by subtracting the zero-crossing point of the baseline signal from the corresponding zero crossing of the current signal.

4.3.2 Temperature compensation

As previously stated, temperature variations can cause changes in the phase traveltime regardless of the occurrence of damage. In metals it is well known that an increase in temperature causes a decrease in the ultrasonic bulk velocities at a rate of about 1 m $s^{-1\circ}C^{-1}$; in mild steel the longitudinal and shear velocity temperature coefficients are -0.88 and -0.71 m $s^{-1\circ}C^{-1}$, respectively [81]. This in turn alters the dispersion characteristics of phase and group velocity in a complex fashion [82] although in the vicinity of the CGV point these relationships are very much simplified [28]. Figure 4.4(a) shows the current signals (with damage) measured at 126°C and the baselines signals measured at room temperature. Although the defect is the same as that of Fig. 4.3, the 100°C temperature difference between the baseline and current measurements leads to clearly visible temporal shifts between wavepackets. The temporal shifts are greater than those caused by the defect itself as it can be seen in Figure 4.4(b) which is extracted from Fig. 4.3. Temperature differentials of 100°C or even greater are likely in practice since pipelines are typically exposed to extreme weather conditions and variations in the temperature of the fluid transported in them.

In order to minimize the impact of temperature variations this chapter proposes a compensation technique that adjusts the baseline measurements to match the temperature of

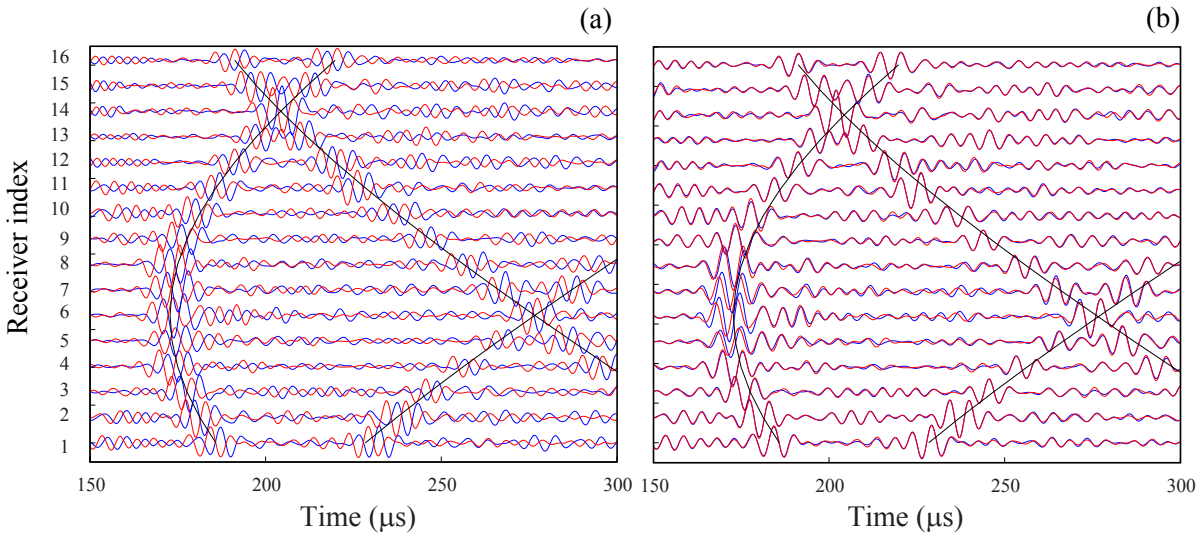

Figure 4.4: Effect of temperature on the measured waveforms when source #6 radiates. (a) Current signals measured at 126°C; (b) Current signals measured at room temperature. In both cases the baseline (red waveforms) is measured at room temperature.

the current measurements. The proposed approach is based on the observation that due to the spatial diversity of the array measurements, a temperature change affects the traveltime matrix with a precise pattern determined by transducer relative distances. Let $\tau^b(\Theta_b)$ be the matrix of phase traveltimes obtained from the baseline measurements at temperature Θ_b and $\tau^c(\Theta_c)$ the matrix of traveltimes obtained from the current measurements at temperature Θ_c; in general $\tau^c(\Theta_c)$ may be affected by the presence of damage. Defining Δc as the phase velocity change due to the temperature difference $\Theta_c - \Theta_b$, the j-i entry of the baseline traveltime matrix at temperature Θ_c is

$$\tau^b_{ji}(\Theta_c) = \tau^b_{ji}(\Theta_b) - \frac{D_{ji}\Delta c}{c^b[\Delta c + c^b]}, \tag{4.7}$$

where as before D_{ji} is the distance between the i-th transducer of the virtual transmit array and the j-th transducer of the virtual receive array, and c^b is the phase velocity at the temperature of the baseline measurements. Assuming that the defect is localized in a confined region of the pipeline section comprised between the two arrays, it can be expected

that the traveltimes of several transmit-receive pairs of the current dataset are not affected by the defect and are only dependent on temperature variations. Under this assumption, Δc, can be estimated by minimizing the residual between $\tau^c(\Theta_c)$ and $\tau^b(\Theta_c)$. This is achieved through a least squares criterion based on the minimization of the cost function

$$C(\Delta c) = \sum_{i=1}^{(1+m)N} \sum_{j=1}^{(1+m)N} [\tau^c_{ji}(\Theta_c) - \tau^b_{ji}(\Theta_c)]^2. \tag{4.8}$$

The value of Δc resulting in a global minimum for the cost function C, $\Delta c^\dagger$, provides the best estimate for the change in phase velocity between the current and baseline temperatures, i. e.

$$\Delta c^\dagger = \arg\min_{\Delta c} C(\Delta c). \tag{4.9}$$

The temperature compensated traveltime difference matrix is then

$$\Delta\tau_{ji} = \tau^c_{ji}(\Theta_c) - \tau^b_{ji}(\Theta_b) + \frac{D_{ji}\Delta c^\dagger}{c^b(\Delta c^\dagger + c^b)}. \tag{4.10}$$

Figure 4.5 compares the traveltime difference matrices obtained before, Fig. 4.5(a), and after, Fig. 4.5(b), temperature compensation for the current dataset measured at 126°C and the baseline measured at room temperature. Before temperature compensation large traveltime differences as high as 10μs are caused by the 100°C temperature differential between the current and baseline dataset, and swamp the signatures from the defect (set of three diagonal patters). On the other hand, the defect signatures are recovered in Fig. 4.5(b) after temperature compensation with the largest traveltimes now being in the region of 1.5μs. Moreover, the traveltime matrix in Fig. 4.5(b) reproduces the same features seen in Fig. 4.5(c) which is the traveltime difference matrix obtained under stable temperature conditions, i. e. both the current and baseline signals are measured at room temperature.

It should be observed that the phase velocity map reconstructed from the temperature

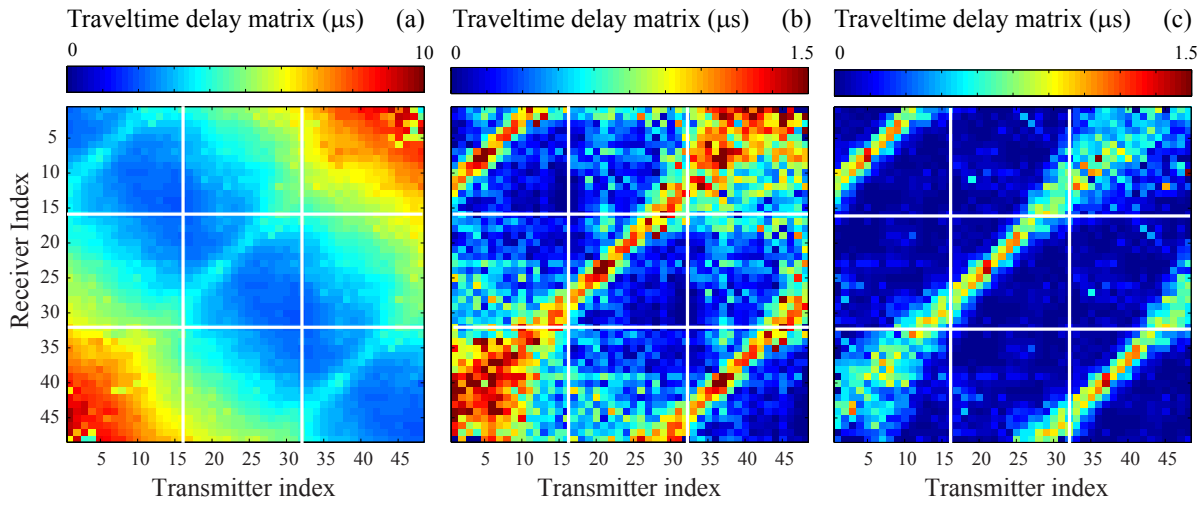

Figure 4.5: Temperature compensation of experimental data: (a) Traveltime delay matrix obtained when the temperature differential between current and baseline measurements is 100°C; (b) Traveltime delay matrix after temperature compensation; (c) Traveltime delay matrix obtained under stable temperature conditions — current and baseline measurements are performed both at room temperature. Note the color scale of the uncompensated matrix is different from the others.

compensated traveltime difference matrix refers to the dispersion curve of the selected mode at the current temperature, $c_{ph}(f \cdot d, \Theta_c)$. As pointed out earlier this is different from the dispersion curve of the same mode at the baseline temperature, $c_{ph}(f \cdot d, \Theta_b)$. Therefore, the defect depth should be determined by inverting the dispersion curve $c_{ph}(f \cdot d, \Theta_c)$. However, to a first order approximation the slope $\partial c_{ph}/\partial(f \cdot d)$ can be assumed to be independent of temperature. As a result depth reconstruction, which is mainly dependent on the velocity contrast rather than the absolute velocity values, can be performed from the dispersion curve measured at the baseline temperature.

4.4 Experimental depth reconstructions

The same inversion algorithm used to process the synthetic data in Sec. 3.2 is now applied to the pre-processed data from Sec. 4.3. Figure 4.6 demonstrates the benefit of using higher-order helical modes (columns) and the effectiveness of the temperature compensation

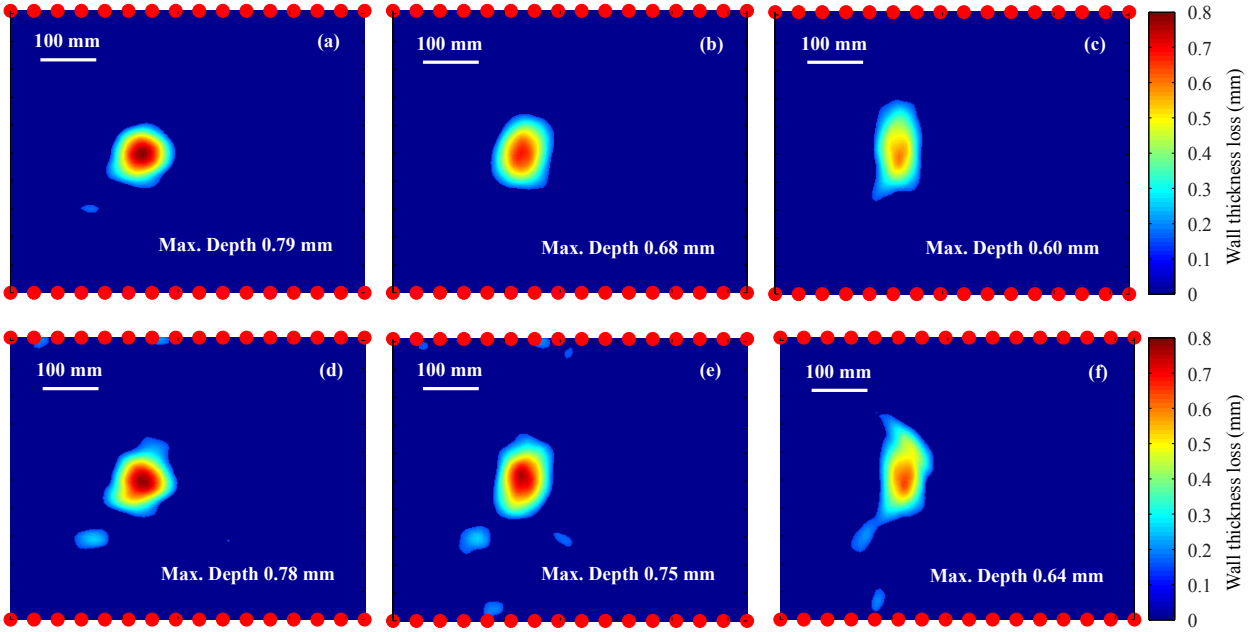

Figure 4.6: WTL maps reconstructed from the experimental data. The maps are obtained by considering up to the second order modes (first column), first order (second column) and direct wave-paths only (third column). The first row uses the data in Fig. 4.5(c) which was measured under stable temperature conditions while the second row is obtained from the temperature compensated data in Fig. 4.5(b). The estimated values of maximum depth are indicated in each image.

method (rows). The WTL maps in the first row, Figs. 4.6(a)-(c), are reconstructed from the traveltime difference matrix obtained under stable temperature conditions and shown in Fig. 4.5(c). As observed with the numerical simulations, including up to the second order helical modes in the inversion leads to a maximum depth estimation of 0.79 mm which compares very well with the defect nominal depth of 0.78±0.05 mm. As fewer helical modes are used in the inversion, Figs. 4.6(b)-(c), accuracy decreases and the maximum depth is underestimated by 0.18 mm when only direct paths are considered. A similar trend is observed when inverting the temperature compensated data in Fig. 4.6(b). When using modes up to the second helical order, the reconstructed maximum depth is 0.78 mm which agrees with the nominal measurement and demonstrates the effectiveness of the temperature compensation method.

Figure 4.7(a) shows the maximum depth estimation of the same defect monitored over

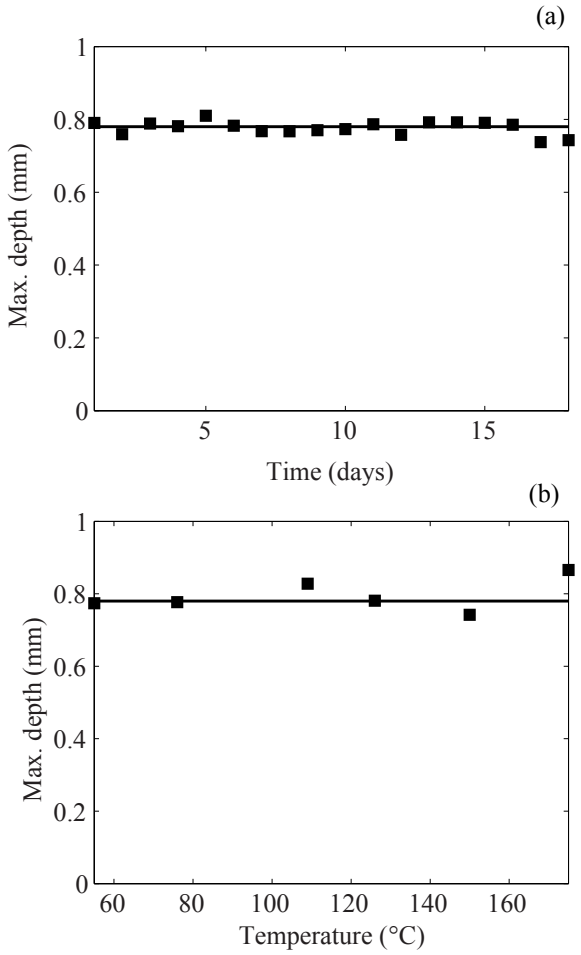

Figure 4.7: Maximum depth monitoring: (a) The pipe is exposed to normal room temperature variations; (b) An internal heater is used to increase the pipe temperature up to 175°C. The horizontal lines indicate the nominal depth measured with a fingertip ultrasonic probe.

a period of one month at room temperature — no insulation was applied to the pipe and temperature randomly varied between 20 and 30°C. Under these conditions the hardware-software system achieved high precision and accuracy, with a mean maximum depth of 0.78 mm and 0.02 mm standard deviation. The performance under more severe temperature variations is shown in Fig. 4.7(b) where the pipe was heated up to 175 °C leading to a temperature differential between the current and baseline measurements of 150 °C. The mean maximum depth was now 0.79 mm with 0.04 mm standard deviation. The increased data scattering is primarily due to small errors in the positioning of the signal windows

applied to the current signals. This is based on an automated routine that adjusts the windows used for the baseline to the current measurements. Overall, the system was still remarkably stable and accurate despite a large temperature swing.

4.5 Discussion of EMATs

It should be stressed that central to the thermal stability of the system is the use of EMAT transducers. In fact, the temperature compensation method introduced in Sec. 4.3 can account for changes occurring in the pipe but cannot compensate for phase instability caused by the transducers. In the experimental study presented in this chapter temporal shifts as small as 0.5 μs corresponding to about 30 deg phase change were measured and used in the inversion. For accurate depth estimation it is therefore essential that the transducer phase is stable within a few degrees especially in the presence of small and shallow defects.

The thermal stability of the EMAT transducers was investigated by monitoring the pitch-catch signal between two transducers mounted on a 200 mm diameter pipe, 12.5 mm wall thickness and spaced 260 mm apart. The signal was monitored for over 100 days and under different thermal cycles as shown in Fig. 4.8(a). For the majority of the test the temperature was cycled between 40 and 250°C with the exception of shorter periods of time when the temperature was held constant at 300, 350, and 400°C. The frequency of the signal (110 kHz) was centered at the CGV point were the true phase of the A_0 mode is independent of temperature [27, 28]. Therefore, at this frequency a change in the true phase of the signal can only be due to thermal instability of the transducers, thus providing a means to decouple transducer effects from changes in the pipe. The true phase of the signal is shown in Fig. 4.8(b). For temperature fluctuations within 200°C the transducers were very stable with phase variations well within ±10 deg. Even when the temperature reached 400°C, the absolute phase change was about 20 deg. Similarly, the amplitude of the signal was remarkably stable throughout the entire temperature range as shown in Fig. 4.8(b). The

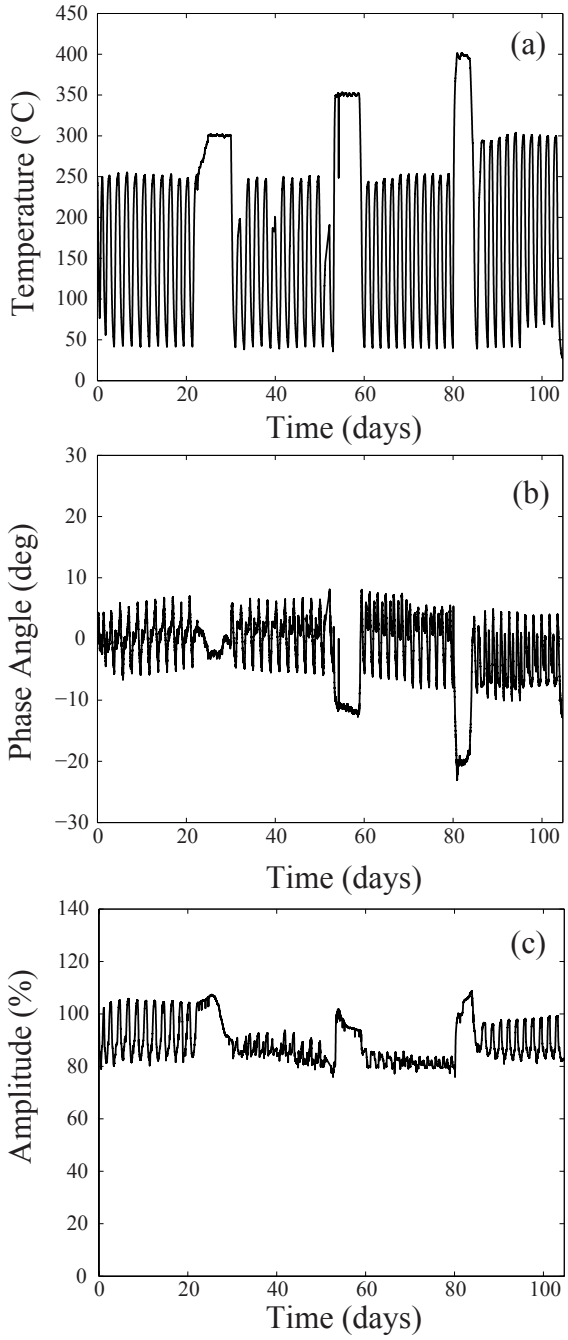

Figure 4.8: Long term monitoring of EMAT transducers under thermal cycling: (a) Applied thermal cycles; (b) True phase; (c) Normalized amplitude.

good thermal stability of the EMAT transducers is largely due to the mechanism of energy transfer from the transducer to the pipe which is based on electromagnetic coupling rather than mechanical as in the case of piezoelectric transducers.

4.6 Conclusion

Mitigation of the TIPU was shown to be possible using a residual based on differential measurements comparing the baseline and current states of the pipe. The baseline and current states correspond to the datasets acquired at the time of monitoring system installation, and the current time respectively. Thus, the benefit of increased accuracy is obtained for the relatively low cost of acquiring the baseline measurements.

To minimize the effects of temperature variations during continuous monitoring, a strategy based on a temperature compensation scheme and the use of EMATs was developed. The former uses the spatial diversity of array measurements to compensate for the changes in phase and group velocity due to temperature variations inside the pipe wall. EMATs on the other hand, avoid the use of mechanical coupling between the transducer and pipe and therefore are intrinsically stable with temperature.

Both the inversion method and the temperature compensation scheme were tested with a full-scale experiment performed on a schedule 40, 8" diameter steel pipe, with an irregularly shaped defect of 0.78 $\pm$ 0.05 mm maximum depth. The pipe was instrumented with two ring arrays each consisting of 16 EMAT transducers. When monitoring the defect at room temperature for about one month GWT yielded a maximum depth estimation of 0.78 $\pm$ 0.02 mm. Accurate readings were also obtained when the pipe temperature was increased to 175°C with an estimated maximum depth of 0.79 $\pm$ 0.04 mm.

Chapter 5

On the accuracy of wave speed reconstructions below the resolution scale of ray tomography

Mapping the speed of mechanical waves traveling inside a medium is a topic of great interest across many fields from geoscience to medical diagnostics. Much work has been done to characterize the fidelity with which the geometrical features of the medium can be reconstructed and multiple resolution criteria have been proposed depending on the accuracy of the wave-matter interaction model used to decode the wave speed map (WSM) from scattering measurements. However, these criteria do not define the accuracy with which the wave speed values can be reconstructed and their use to predict the performance of quantitative WSM can be overpessimistic. This chapter shows that the first-arrival traveltime predicted by the eikonal equation of ray theory can be an accurate representation of the arrival of a pulse first break even in the presence of diffraction and other physical phenomena that are not accounted for by the ray model. As a result, ray-based tomographic inversions can yield wave speed estimations that are also accurate in the case of objects whose characteristic size is smaller than the resolution length of the inversion method provided that the traveltime of

the pulse is estimated from the signal first break.

5.1 Introduction

The non-intrusive characterization of the state of an inhomogeneous medium can be achieved by mapping the speed at which mechanical waves travel within its interior. Wave speed can encode information about both the material and functional properties of the medium offering the possibility of complementing conventional imaging, which provides *shape* information, with quantitative information that better correlates to the state of the medium. Quantitative imaging has far reaching applications in multiple fields. In seismology, the layers that form the structure of the earth, from the inner core to the upper mantle, are characterized based on the contrast of seismic wave speed and mass density across the different interfaces (see, for instance, Nolet [83], Yilmaz [84]). Similarly, in medical diagnostics cancer can be detected by exploiting the sound speed contrast of ultrasonic waves traveling between healthy tissue and malignant masses [85–88]. In industrial applications, the microstructure, state of stress, and the presence of damage in the material of safety-critical structural components can be assessed based on ultrasonic velocity measurements [89, 90]. In addition, wave speed information can be used to characterize the boundaries of the medium when it forms a waveguide. In this case, the speed of the resulting guided wave is dependent on the geometry of the waveguide and changes due to the presence of defects that alter its shape [36, 91].

To form a wave speed map (WSM), the medium is interrogated using multiple sources that launch waves from different angles and at different times. The wavefield excited by each source propagates through the medium and is then detected by multiple sensors outside it. If N sources and M detectors are used, a dataset consisting of $N \times M$ waveforms is measured and constitutes the base to form the WSM using the principles of model based inversion. For this purpose, a physical forward model in the form of a set of differential equations is postulated to describe the interaction of the probing wave with the medium and predict

the synthetic dataset associated with a given WSM. If a linear forward model is applicable, the inversion is conducted by simply applying a linear operator to the measured dataset as in the case of diffraction tomography or the filtered back projection method [42]. However, linear forward models tend to be inaccurate for most applications involving mechanical waves and therefore can lead to significant errors in the reconstructed WSM. To fully account for diffraction, refraction, and multiple scattering effects nonlinear forward models are needed - here nonlinearity refers to the dependence of the wavefield on the mechanical properties of the medium [41]. As a result, also the inversion becomes nonlinear and must be performed through the use of iterative schemes whereby an assumed WSM is adjusted until the residual between the measured and synthetic datasets is minimized.

The accuracy with which wave speed can be estimated is central to the effectiveness of quantitative imaging and is governed by multiple, interconnected factors including the wavelength, λ, of the probing signals, the method of inversion, the availability of a sufficiently diverse set of interrogation angles, and the level of experimental uncertainties and noise. The complex interaction between these factors poses a significant challenge when trying to define general criteria to predict the performance of model based inversion. In this context, resolution is used as the main criterion to characterize the quality of the WSM and refers to the ability of the inversion to discriminate between two closely spaced geometrical features of the medium. However, resolution, which has the units of length, does not provide information about the accuracy of the wave speed estimations. Moreover, a rigorous definition of resolution criteria can only be obtained in the case of linear forward models. For instance, Wolf [92] demonstrated that under the Born approximation, which leads to a linear scattering model, the resolution limit of diffraction tomography is $\lambda/2$; however the limit is no longer valid if multiple scattering effects are taken into account [93, 94]. It is important to observe that in the case of a linear forward model it is possible to establish a link between resolution and wave speed estimation accuracy. This is based on the definition of the point spread function (PSF) which corresponds to the WSM reconstructed for an ideal medium where the

wave speed is everywhere uniform except at one point. Due to the limited resolution of any inversion method, the reconstructed WSM is a blurred disk around that point and whose diameter is proportional to the resolution length of the inversion method. If the medium is interrogated from a sufficiently diverse range of angles, the PSF is space invariant and therefore the reconstructed WSM for an inhomogeneous medium is given by the convolution of the PSF with the true WSM. As a result, if the diameter of the PSF disk is small compared to the spatial scale over which the wave velocity varies, i.e. the resolution is high, the WSM is reconstructed with high accuracy. On the other hand, if the diameter is large, the reconstructed WSM is a smoothed version of the true WSM thus causing errors in the wave speed estimations. While it is tempting to extend this relationship between resolution and accuracy to the case of nonlinear forward models, it must be realized that it is not strictly meaningful to define a PSF for a nonlinear forward model since the result of the inversion cannot be cast in the form of the convolution of the PSF with the true WSM. In other words, the image of a collection of points is no longer the same as the superposition of the images of the isolated points. Therefore, while it is customary to assume that higher resolution leads to higher wave speed accuracy, many instances can be found in the literature where this is not necessarily the case. An interesting example is given by the comparison between full wave inversion (FWI) and ray tomography (RT). The former uses a forward model that describes the wave-medium interaction based on the full wave equation while the latter is based on an approximate asymptotic form of the same equation known as the eikonal equation, which accounts for refraction effects but neglects diffraction and multiple scattering. FWI has now gained widespread use in geophysical exploration owing to its higher resolution compared to the more conventional RT as clearly demonstrated in the seminal work by Pratt [69]. Here, FWI and RT are applied to experimental data measured on a resin block with an inhomogeneous structure consisting of multiple homogeneous layers (uniform wave speed). As shown in Fig. 11 of Pratt [69], FWI leads to a substantial increase in the sharpness of the interfaces between layers compared to RT and hence higher resolution. However, the

reconstructed wave speed within each layer is generally less accurate than that obtained by RT thus demonstrating that the link between resolution and accuracy can break when using nonlinear inversion methods.

Another argument against the validity of the link between resolution and WSM accuracy lies in the observation that resolution criteria do not depend on the level of wave speed contrast within the medium. This is apparent when considering the $\lambda/2$ resolution limit of diffraction tomography or the $\sqrt{\lambda L}$ of RT [45], where L is the source-to-receiver distance. Indeed, both criteria are derived under a weak-perturbation approximation which implies that the wave speed contrast is generally small.

While it would be ideal to reconstruct a WSM with both high resolution and accuracy, in some applications it is sufficient to accurately characterize the range of variation of the wave speed throughout the medium. As an example, life management of pipelines in the oil and gas industry requires knowing the maximum wall thickness loss due to corrosion or erosion rather than knowing the exact defect shape. This translates into how accurately the velocity extrema of guided waves traveling in the pipe wall can be estimated [91].

The objective of this chapter is to investigate whether WSMs can be reconstructed with satisfactory accuracy also when the wave speed varies on a spatial length that is smaller than the assumed resolution scale of the inversion method. The analysis is carried out in the context of traveltime RT for three main reasons. First, the forward model of RT embodies Fermat's least time principle which directly relates to wave speed. Second, previous work by Li and Duric [95] has already shown that RT can achieve resolution beyond $\sqrt{\lambda L}$. Finally, as seen in the case of FWI more sophisticated forward models do not necessarily lead to higher accuracy in practical applications as they become more susceptible to parametric uncertainties which are unavoidable under realistic experimental conditions. This is also the reason why RT is typically more stable than more advanced inversion methods [96].

In Sec. 5.2 the sensitivity kernel theory (SKT) is reviewed to describe the classical interpretation of the encoding of information in traveltime measurements, the definition of

the resolution limit of RT, and the wavefront healing phenomenon. The limitations of the SKT are highlighted in Sec. 5.3 where traveltimes estimated from full wave simulations are compared against the first-arrival traveltimes predicted by the eikonal equation of ray theory. Here, the accuracy of the eikonal traveltimes is studied as a function of wave speed contrast and contrast bounds for its validity are defined. In Sec. 5.4 the accuracy of RT is investigated for the case of objects occupying a spatial scale smaller than $\sqrt{\lambda L}$. Finally, concluding remarks are given in Sec. 5.5.

5.2 The encoding of information in pulse traveltimes

This section studies the mechanisms that govern how information about wave speed contrast is encoded in the measured wave signals. Considering Cartesian coordinates $\{O, x_1, x_2, x_3\}$, ray theory predicts that the traveltime of a wave pulse traveling from a source at $\mathbf{s} \equiv (s_1, s_2, s_3)$ to a point $\mathbf{x} \equiv (x_1, x_2, x_3)$, $\tau(\mathbf{x}, \mathbf{s})$, satisfies the eikonal equation

$$\left[\frac{\partial \tau(\mathbf{x}, \mathbf{s})}{\partial x_1}\right]^2 + \left[\frac{\partial \tau(\mathbf{x}, \mathbf{s})}{\partial x_2}\right]^2 + \left[\frac{\partial \tau(\mathbf{x}, \mathbf{s})}{\partial x_3}\right]^2 = \frac{1}{c(\mathbf{x})^2}, \tag{5.1}$$

where $c(\mathbf{x})$ is the wave speed at point $\mathbf{x}$. RT reconstructs $c(\mathbf{x})$ using as an input the set of $N \times M$ traveltimes extracted from the experimental signals measured for all the possible transmit-receive pairs that can be formed with N sources and M receivers. Clearly, to reconstruct $c(\mathbf{x})$ it is necessary that the $N \times M$ traveltimes encode sufficient information about $c(\mathbf{x})$ or in other words the traveltimes are sensitive to $c(\mathbf{x})$. This leads to the concept of sensitivity kernels which attempt to reconcile ray theory with diffraction theory [97]. In ray theory the propagation of a wave pulse is modeled as a particle traveling along a ray whose path is determined by reflection and refraction laws only. As a result, the traveltime predicted by ray theory is only dependent on the wave speed along the path from the source

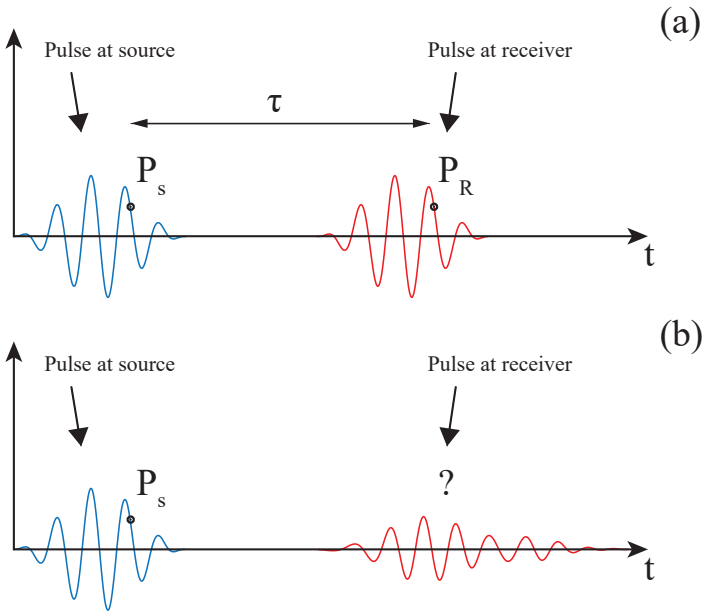

Figure 5.1: Illustration of the effect of pulse distortion on traveltime estimations: (a) when a pulse undergoes a rigid translation traveltime can be estimated by tracking any point in the pulse; (b) due to distortion it is no longer possible to track the same pulse point leading to ambiguity in traveltime estimations.

to the receiver Γ

$$\tau(\mathbf{r}, \mathbf{s}) = \int_{\Gamma} \frac{1}{c(\mathbf{x})} d\Gamma, \tag{5.2}$$

where $\mathbf{r} \equiv (r_1, r_2, r_3)$ represents the position of the receiver. Expression (5.2) implies that the propagation of a wave pulse is equivalent to the rigid translation of the pulse along the path Γ. Under this assumption the traveltime can be estimated from the measured signals by selecting any arbitrary point of the pulse at the source, P_S, and mapping it into the same point of the pulse at the receiver, P_R, as shown in Fig. 5.1(a). However, experimental pulses can experience significant distortion due to diffraction, energy dissipation, dispersion, the presence of overlapping pulses, and the fact that the wavefront is not confined to a ray but rather a full volume around the ray. The distortion of the pulse implies that it is no longer possible to unequivocally map P_S onto the corresponding point P_R of the received pulse, see

Fig. 5.1(b). As a result, the definition of traveltime becomes somewhat arbitrary and has led to a wide range of different traveltime picking techniques, see for instance Ref. [83].

The sensitivity kernel theory (SKT) is developed based on cross-correlation traveltime picking and assumes that the wave speed field can be considered as a small perturbation relative to a reference value, c_0, i. e. $\delta c = c(\mathbf{x}) - c_0$. This allows ray bending to be neglected and wave propagation to be formulated in terms of a perturbation problem in which the absolute traveltime is replaced by the traveltime shift, $\delta\tau$, caused by the velocity perturbation δc. This leads to a new expression for Eq. (5.2)

$$\delta\tau(\mathbf{r},\mathbf{s}) = \int_\Gamma \frac{1}{c_0 + \delta c(\mathbf{x})} d\Gamma - \frac{L}{c_0}, \tag{5.3}$$

where $L = |\mathbf{r} - \mathbf{s}|$ is the distance between the source and receiver. By taking into account diffraction effects based on linearized single scattering models (Born or Rytov) it can be shown that $\delta\tau$ also encodes information about wave speed outside the ray path according to

$$\delta\tau(\mathbf{r},\mathbf{s}) = \int_\Omega K(\mathbf{x},\mathbf{r},\mathbf{s}) \frac{\delta c(\mathbf{x})}{c_0} d\Omega, \tag{5.4}$$

where Ω represents the three-dimensional volume and $K(\mathbf{x},\mathbf{r},\mathbf{s})$ is the sensitivity kernel [98, 99]. From Eq. (5.4), $\delta\tau(\mathbf{r},\mathbf{s})$ is the weighted sum of wave speed contrast δc over a volume around the ray defined by the sensitivity kernel. As shown in Spetzler and Snieder [100] this volume corresponds to the ellipsoid that defines the first Fresnel zone with foci at the source and receiver and whose width is equal to $\sqrt{\lambda L}$.

The width of the sensitivity kernel leads to a resolution criterion for RT. This can be justified by first observing that RT would achieve unlimited resolution if the traveltime measurements were consistent with the forward model given by Eq. (5.3). However, if a uniform contrast perturbation δc occurs over a volume $\delta\Omega$ of size δl much smaller than $\sqrt{\lambda L}$, the measured traveltime is not only dependent on the contrast δc along the ray length δl but it will also depend on the value of δc in similar size volumes, $\delta\Omega'$, outside the ray as shown in

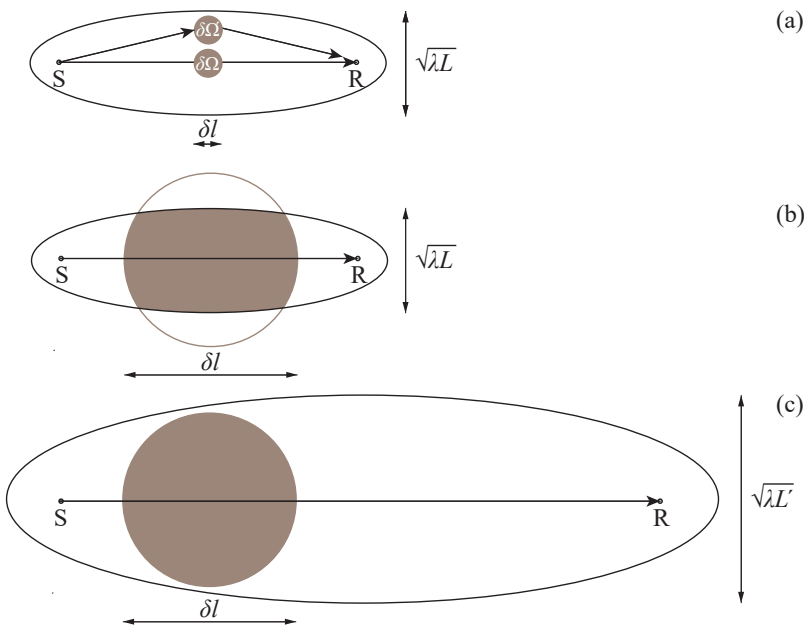

Figure 5.2: Illustration of the role of the sensitivity kernel width, $\sqrt{\lambda L}$, on the resolution of ray tomography and the wavefront healing phenomenon. (a) A uniform sound speed perturbation of size $\delta l < \sqrt{\lambda L}$ occupies a small portion of the kernel volume causing a small change in traveltime and making it dependent on the sound speed contrast in the direction transversal to the ray; (b) A perturbation with $\delta l > \sqrt{\lambda L}$ leads to a traveltime that is only dependent on the sound speed contrast along the ray consistently with ray theory; (c) Increasing the distance of the receiver from the source widens the kernel causing the sound speed perturbation to become increasing smaller relative to the kernel and hence weakening the effect of the perturbation on traveltime.

Fig. 5.2(a). As a result, the measurements are not consistent with the model and since $\delta\Omega$ is small relative to the volume of the sensitivity kernel, the perturbation δc will contribute little to the value of $\delta\tau(\mathbf{r}, \mathbf{s})$, i.e. the measurements will have low sensitivity to δc. Conversely, if $\delta l > \sqrt{\lambda L}$, the traveltime is only dependent on the contrast δc along the *fat* ray element δl, Fig. 5.2(b), which leads to a traveltime value that is more consistent with the model in Eq. (5.3). Moreover, the perturbation now occupies a significant fraction of the volume of the sensitivity kernel which translates into a higher sensitivity of the traveltime measurements. Therefore, $\sqrt{\lambda L}$ defines a resolution length scale such that a uniform perturbation δc occurring in a ball of diameter greater than $\sqrt{\lambda L}$ produces measurable traveltime shifts that are consistent with the forward model of RT and hence can be reconstructed with high

accuracy.

Related to $\sqrt{\lambda L}$ is the so-called wavefront healing phenomenon [101] which causes the traveltime shift induced by δc to weaken as the wavefront propagates away from the volume $\delta\Omega$. As illustrated in Fig. 5.2(c) to detect a wavefield that has propagated a larger distance from $\delta\Omega$ the receiver needs to be moved out compared to the configuration in Fig. 5.2(b). As a result, the increased source-to-receiver distance, L', leads to a larger volume of the sensitivity kernel relative to $\delta\Omega$ which makes the contribution of δc to $\delta\tau(\mathbf{r}, \mathbf{s})$ smaller. Consequently, wavefront healing causes a loss of information and has a negative effect on the performance of RT.

While sensitivity kernels are effective in providing a resolution criterion, their applicability is limited to the case of weak scattering and traveltime estimations based on cross-correlation. In particular, the use of cross correlation can lead to exceedingly conservative resolution predictions. This is because localized (small spatial scale) velocity perturbations manifest primarily as pulse distortions rather than rigid shifts thus making cross correlation ineffective. For instance, Malcolm and Trampert [48] showed that in the case of fast inclusions traveltime estimations based on the first break of the first arrival can help mitigate the effect of diffraction. They also provided a clear illustration of the limitations of cross-correlation in Fig. 5 of Malcolm and Trampert [48] where they compared the wave pulse measured before and after the introduction of a velocity perturbation which induces significant pulse distortion but which is interpreted by cross correlation as a zero traveltime shift.

The single order scattering approximation, neglecting ray bending, and the use of cross-correlation may lead to an overestimation of the width of the sensitivity kernels. Therefore, it is possible that traveltime measurements encode more information than that predicted by the SKT and that this information is accessible provided that different picking methods are used.

5.3 Validity of the ray model beyond $\sqrt{\lambda L}$

This section studies the accuracy of traveltime predictions based on the eikonal equation for cases that are beyond the limits set by the SKT. These cases vary depending on a vast range of parameters including L, λ, the relative contrast field $\mu(\mathbf{x}) = \delta c(\mathbf{x})/c_0$, and the characteristic size, D, of the support of $\mu(\mathbf{x})$. In addition, the traveltime analysis can be affected by the nature of the medium, e.g. elastic solid versus fluid. Here, I consider a two-dimensional acoustic model capable of rapid computation whilst accounting for key refraction, diffraction, and multiple scattering effects based on the full wave equation given by

$$\nabla^2 P(\mathbf{x}) = \frac{1}{c^2(\mathbf{x})} \frac{\partial^2 P(\mathbf{x})}{\partial t^2} + F(\mathbf{x}, t), \tag{5.5}$$

where ∇^2 is the Laplacian, P, represents the pressure field, $c(\mathbf{x})$, is the local sound speed, and $F(\mathbf{x}, t)$ represents the acoustic source. Equation (5.5) is a valid physical model when mass density gradients are negligible and the spatial scale over which $c(\mathbf{x})$ varies is greater than λ. Equation (5.5) is solved using the finite difference (FD) method as discussed in Sec. 3.2. In all simulations the wave is excited by a point source that launches a five-cycle Hann-windowed pulse.

The eikonal equation for the acoustic problem is given by the two-dimensional expression of Eq. (5.1) and is solved using the fast marching method (FMM) [102]. The FMM begins with a start location, and incrementally expands the solution in order of increasing traveltime or expanding wavefront. It should be noted that FMM can provide the first-arrival traveltime while it fails to predict intersecting rays and later arrivals [103].

To estimate traveltimes from the full wave simulations, the instantaneous frequency (IF), which detects the first break of the first arrival [104], is employed. Therefore, for a signal, $s(t)$, the traveltime is estimated by transforming the function $s(t)$ into the instantaneous frequency function, $f(t)$, which is obtained from the Hilbert transform of the signal, $h(t)$,

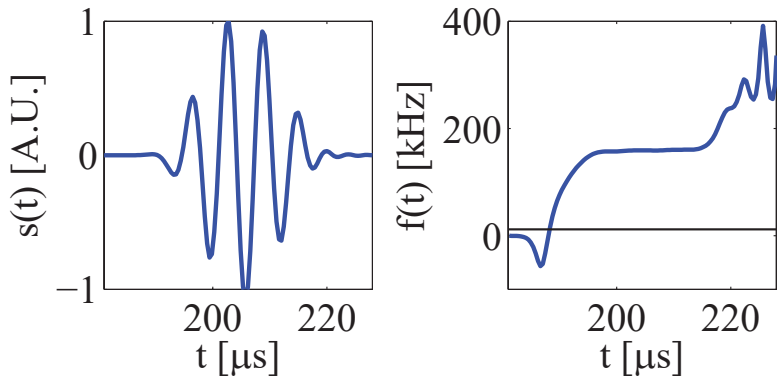

Figure 5.3: Transformation of signal function with center frequency of 160 kHz, $s(t)$ (a) into the instantaneous frequency function (b). The black horizontal line shown in (b) corresponds to the threshold associated with the picked traveltime.

according to

$$f(t) = \frac{1}{2\pi}\frac{d}{dt}(\angle[h(t)]), \tag{5.6}$$

where $\angle$ refers to the phase of $h(t)$, and $\frac{d}{dt}$ is the time derivative. Figure 5.3 shows an example of a signal $s(t)$ (Fig. 5.3(a)) and its corresponding instantaneous frequency function, Fig. 5.3(b). The traveltime, τ, is determined by considering the point in time where $f(t)$ breaks above a prescribed threshold level, shown as the black horizontal line in Fig. 5.3(b).

How accurately the first break can be measured in actual experimental waveforms is dependent on the traveltime picking method, the level of noise, and the shape of the transmitted pulse. These factors are application specific and the optimization of the picking method is the subject of active research [105] and therefore will not be considered in this analysis.

5.3.1 Cylindrical inclusions

This analysis is begun by considering the canonical case of cylindrical inclusions of uniform contrast μ. The length scales are normalized relative to the wavelengths so that the separation distanced between the source and receive transducer is $l = L/\lambda$ and the diameter, D,

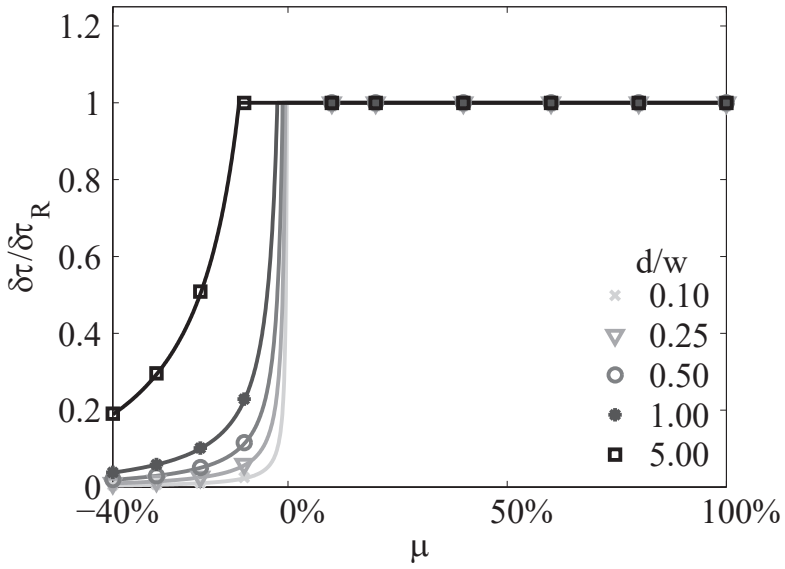

Figure 5.4: Normalized traveltime shifts predicted by the eikonal equation for a homogeneous cylinder immersed in a homogeneous background. The traveltimes are computed for different values of the sound speed contrast μ and for a range of cylinder diameter to width of the sensitivity kernel ratios, d/w. The markers indicated the eikonal predictions while the curves correspond to the analytical expressions given in the text.

of the cylinders is $d = D/\lambda$. The cylinders are placed at the midpoint between the source and the receiver whose distance is fixed at $l = 400$ unless otherwise specified. Therefore, the normalized width of the sensitivity kernel, w, is

$$w = \frac{\sqrt{\lambda L}}{\lambda} = \sqrt{l} = 20. \tag{5.7}$$

Similarly, the traveltime shifts are normalized relative to the ideal traveltime shift that would be observed for the straight refracted ray traveling along the diameter of the cylinder

$$\delta\tau_R = \frac{D}{c_0 + \delta c} - \frac{D}{c_0} = -\frac{D}{c_0}\frac{\mu}{1+\mu} = -Td\frac{\mu}{1+\mu}, \tag{5.8}$$

where, T, is the period of the wave pulse at the center frequency.

Figure 5.4 shows the first arrival traveltimes predicted by the eikonal equation for a

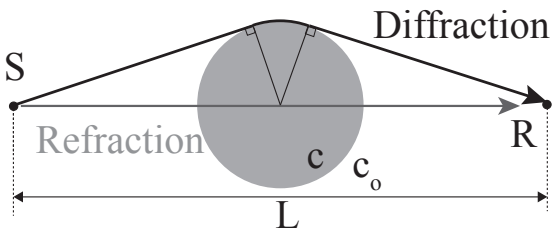

Figure 5.5: Diagram illustrating the refracted and diffracted wave paths observed when a cylinder is placed half way between a source S and a receiver R.

range of slow and fast cylinders with sound speed contrast varying from μ=-40 to +100% and diameters varying from 10 to 500% of the sensitivity kernel width. For fast inclusions ($\mu > 0$), the least traveltime corresponds to a straight ray from the source to the receiver and therefore the eikonal traveltime matches the ideal traveltime shift, i.e. $\delta\tau/\delta\tau_R = 1$. For slow inclusions, the trajectory of the ray switches from the straight ray to the ray tangent to the circular inclusion shown in Fig. 5.5. The transition occurs when the contrast is lower than a critical value μ_{cr} according to

$$\mu < \mu_{cr} = -\frac{\sqrt{(l/d)^2 - 1} + \arcsin(d/l) - l/d}{\sqrt{(l/d)^2 - 1} + \arcsin(d/l) + 1 - l/d} \approx -\frac{1}{1 + 2l/d}, \tag{5.9}$$

where the last identity is valid when $l/d > 10$. Criterion (5.9) is derived by imposing the traveltime equivalence between the two ray paths shown in Fig. 5.5. The traveltime shift associated with the tangent ray, $\delta\tau_D$, is only dependent on the diameter of the inclusion and c_0 while it is independent of μ; its normalized expression being given by

$$\frac{\delta\tau_D}{\delta\tau_R} = -\frac{1+\mu}{\mu}\left[\sqrt{(l/d)^2 - 1} + \arcsin(d/l) - l/d\right] \approx -\frac{1+\mu}{\mu}\frac{1}{2l/d}. \tag{5.10}$$

Equation (5.10) corresponds to the curved branches of the plots shown in Fig. 5.4. Therefore for a given d/l ratio, if $\mu \geq \mu_{cr}$, then $\delta\tau/\delta\tau_R = 1$ and the first arrival traveltime encodes information about the sound speed inside the cylinder, while if $\mu < \mu_{cr}$ the first-arrival traveltime becomes insensitive to the contrast inside the cylinder.

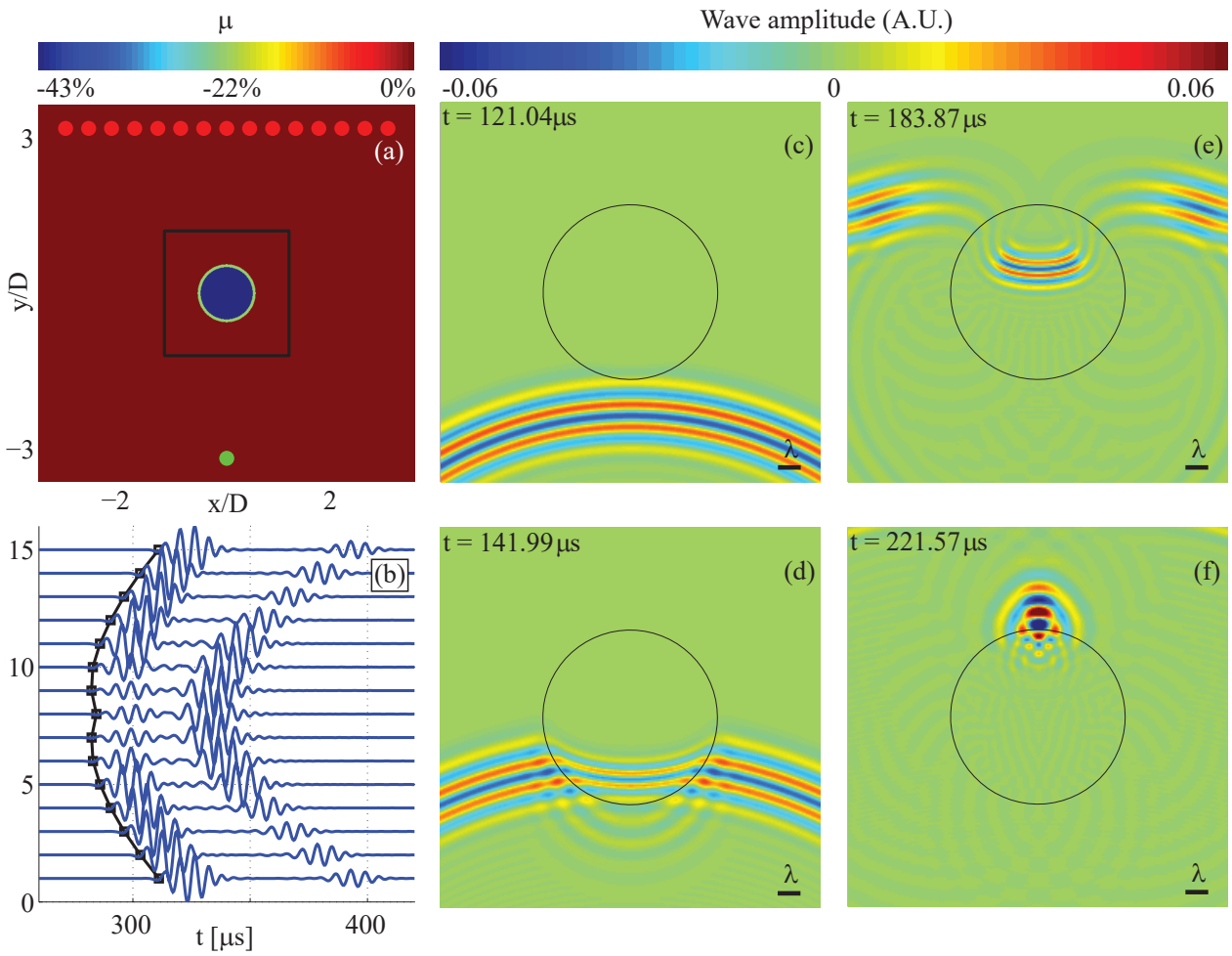

Figure 5.6: Full wave simulation of scattering by a slow cylinder ($\mu = -40\%$) of diameter equal to the width of the sensitivity kernel. (a) diagram showing the position of the cylinder relative to the source and 15 receivers, (b) waveforms measured by the 15 receivers, (c)-(f) snapshots of the wavefield over the rectangular area around the cylinder shown in (a).

The tangent ray path corresponds to a wave diffracted around the cylinder as illustrated in Fig. 5.6 which presents the results of full wave simulations for $\mu = -40\%$, $l = 36$, and $l/d = 6$ or $d/w = 1$. For this configuration $\mu_{cr} = -7.7\%$ which is much larger than the contrast inside the cylinder and therefore it is expected that first arrival will correspond to the tangent ray path. Indeed, the cylinder splits the incident circular wavefront radiating from the source into a fast branch that circles around the inclusion and a slower one that travels inside it, Figs 5.6(c)-(f). Because of the negative contrast, the cylinder acts as a lens

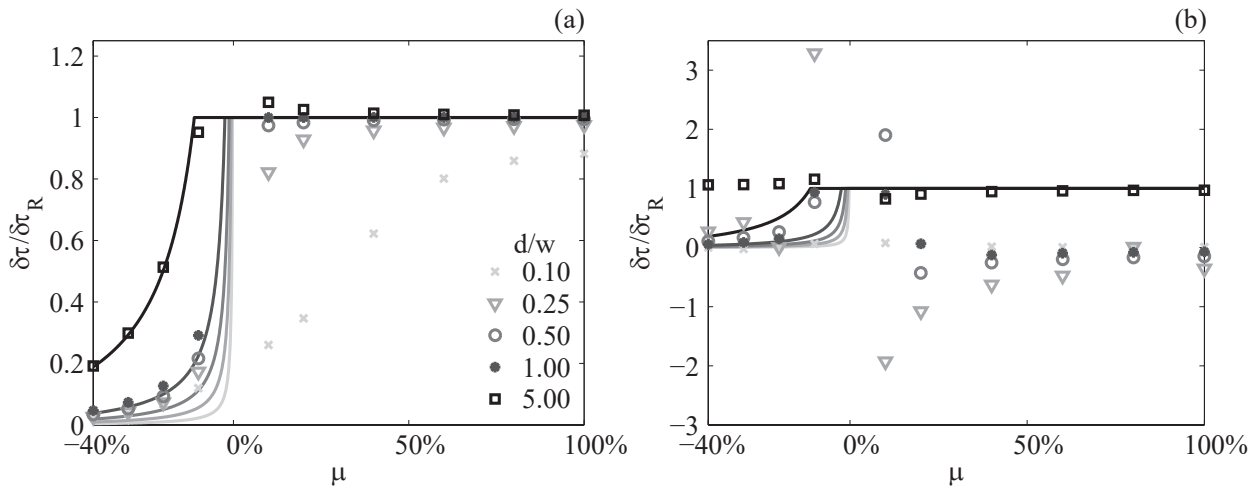

Figure 5.7: Traveltime shifts estimated from full wave simulations using the IF method (a) and the cross-correlation method (b) as a function of contrast, μ, and cylinder diameter to width of the sensitivity kernel ratios, d/w. Note that the vertical scale of (b) is different from that of (a).

which focuses the slow branch onto a point close to the boundary of the cylinder, Fig. 5.6(f), from which the branch continues to propagate as if there were a source at that point. The fast branch is the result of diffraction and corresponds to the tangent ray path shown in Fig. 5.5. This is clearly demonstrated by the agreement between the first arrivals predicted by the eikonal equations (square dots) in Fig. 5.6(b) and the arrivals of the pulses measured by the 15 receivers at the locations shown in Fig. 5.6(a).

To further study the effect of diffraction and wavefront healing, Fig. 5.7(a) shows the normalized traveltime shifts estimated from full wave simulations with the IF method for the same parameter range considered in Fig. 5.4. In contrast with the SKT, the IF traveltimes follow ray theory ($\delta\tau_{IF} \to \delta\tau_R$) also when the diameter of the cylinder is significant smaller than the kernel width. Even for $d/w = 0.1$, $\delta\tau_{IF} \to \delta\tau_R$ when the contrast is sufficiently high. For lower contrast levels, IF begins to underestimate the traveltime shift due to the wavefront healing effect consistently with the SKT which is derived under the small contrast approximation.

The hypothesis considered here is that full wave simulations are consistent with ray

d/w	μ_{cr}	$\mu < \mu_{cr}$	$\mu \geq \mu_{cr}$
0.10	-0.2%	$\mu < -20.2\%$	$\mu \geq 32.9\%$
0.25	-0.6%	$\mu < -9.6\%$	$\mu \geq 10.3\%$
0.50	-1.2%	$\mu < -5.9\%$	$\mu \geq 3.9\%$
1.00	-2.4%	$\mu < -4.8\%$	$\mu \geq 0$
5.00	-11.1%	Any	Any

Table 5.1: Upper and lower contrast bounds for different cylinder diameters relative to the width of the first Fresnel zone as predicted by the criterion in Eq. (5.13).

theory as long as the traveltime is estimated by considering the first break of the wave pulses and that the traveltime difference between the arrivals of the diffracted wave, τ_D, and the refracted wave, τ_R, is larger than half the period of the pulse so as to limit interference effects. A new limit can therefore be introduced as

$$\frac{|\tau_D - \tau_R|}{T} \geq \frac{1}{2}, \tag{5.11}$$

which using Eq. (5.10) for $l/d > 10$ and the definition of μ_{cr} yields

$$\begin{aligned} \frac{d^2}{l} &\geq 1 - 2\frac{\mu d}{1+\mu}, \quad \forall \mu \geq \mu_{cr} \\ \frac{d^2}{l} &< -1 - 2\frac{\mu d}{1+\mu}, \quad \forall \mu < \mu_{cr}, \end{aligned} \tag{5.12}$$

or in terms of the cylinder diameter relative to the kernel width

$$\begin{aligned} \left(\frac{d}{w}\right)^2 &\geq 1 - 2\frac{\mu d}{1+\mu}, \quad \forall \mu \geq \mu_{cr} \\ \left(\frac{d}{w}\right)^2 &< -1 - 2\frac{\mu d}{1+\mu}, \quad \forall \mu < \mu_{cr}. \end{aligned} \tag{5.13}$$

The criterion reduces to the standard RT resolution limit, $d/w \geq 1$, when the contrast vanishes. For a given d/w ratio, the expressions in (5.13) can be used to determine the bounds of contrast that satisfy the criterion. Table 5.1 lists the values of μ obtained from Eqs. (5.13) for the d/w ratios studied in Fig. 5.7. For $d/w = 0.1$, the criterion predicts that

ray theory is valid for negative contrast lower than -20.2% or for positive contrast greater than 32.9%. While this is true for the negative contrast, at $\mu = 32.9\%$ the IF traveltime shift is about 50% lower than the theoretical value, meaning that partial wavefront healing occurs as it can be seen from Fig. 5.7(a). The accuracy of the criterion improves for larger diameter cylinders. As an example, for $d/w = 0.25$ and $\mu = 10.3\%$, the IF traveltime shift is more than 80% of the theoretical ray traveltime shift, i.e. the effect of wavefront healing is much less significant than that predicted by the SKT.

The role of the picking method is illustrated in Fig. 5.7(b) in which the traveltime shifts are now estimated through the cross-correlation method applied to the same full wave simulations used to produce Fig. 5.7(a). It can be observed that for $d/w < 1$ the cross-correlation traveltimes shifts, $\delta\tau_{CC}$, tend to zero for most contrast levels according to the wavefront healing effect predicted by the SKT. On the other hand, for $d/w > 1$, the traveltimes match the first arrivals predicted by ray theory. However for negative contrast, cross-correlation picks the arrival of the slow branch that is refracted through the cylinder according to the phenomenon illustrated in Fig. 5.6 thus leading to $\delta\tau_{CC}/\delta\tau_R \approx 1$. This is because cross-correlation tends to match the shape of the reference pulse to the dominant pulse in the measured waveform. Due to the focusing effect the slow branch is energized at the expense of the fast branch [see the central waveform in Fig. 5.6(b)] causing cross correlation to miss the first arrival.

Cross-correlation severely underestimates traveltimes also when the cylinder diameter is the same as the with of the sensitivity kernel [see $d/w = 1$ in Fig. 5.7(b)] and contrast is positive. This is due to a defocusing phenomenon which causes the refracted waves to have lower amplitude than the diffracted ones. This is demonstrated in Fig. 5.8 which shows the result of full wave simulations as a function of contrast level when $d/w = 1$. For large positive contrast, the first-arrival corresponds to the refracted wave while the second is the pulse diffracted around the cylinder. The latter circles around the cylinder and its arrival is not dependent on the contrast inside the cylinder.

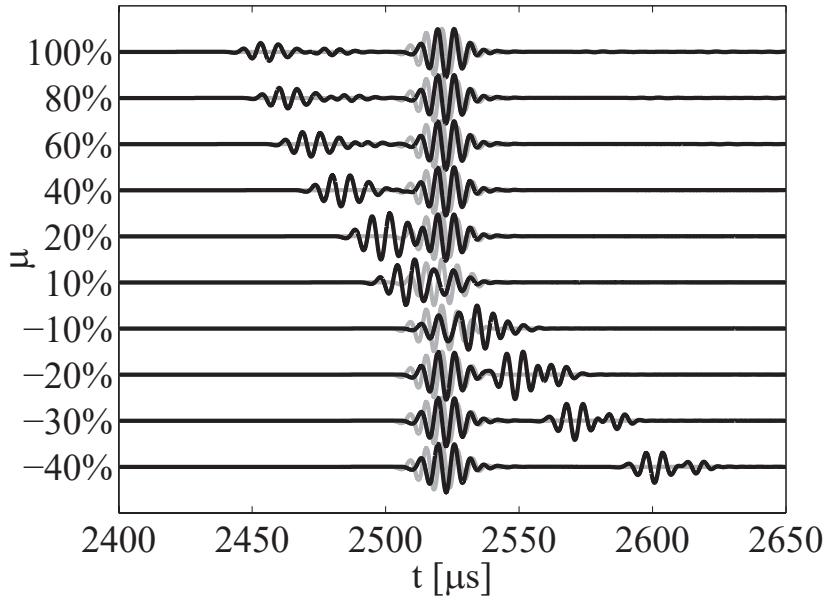

Figure 5.8: Example of defocusing occurring in the presence of positive contrast for a cylinder diameter equal to the width of the sensitivity kernel. The cylinder is centered between a point source and a receiver that are 400λ apart. (gray) baseline signals without the cylinder; (black) signals detected in the presence of the cylinder.

5.3.2 Complex media

In order to study the accuracy of the ray model in the presence of complex inhomogeneous media, consideration is given to a configuration similar to that shown in Fig. 5.6(a) in which an array of aperture 12λ consisting of 60 receivers is placed at a 225λ distance from a source ($l = 225$) and an inhomogeneous region is contained within a circle of diameter equal to the width of the sensitivity kernel ($w = 15$). The array of receivers is centered relative to the source. The inhomogeneous region is shown in Fig. 5.9(a) and is modeled using a contrast map obtained as a sum of Bessel functions, as explained in Appendix A. The contrast is antisymmetric relative to the vertical line joining the source to the center of the array. As a result, the SKT predicts that a receiver at the center of the array would not see any traveltime change since the integral in Eq. (5.4) vanishes. However, this is not true as it can be deduced from Fig. 5.10 which compares the signal simulated with and without the inhomogeneous region for the central receiver. Here, the IF method detects a traveltime

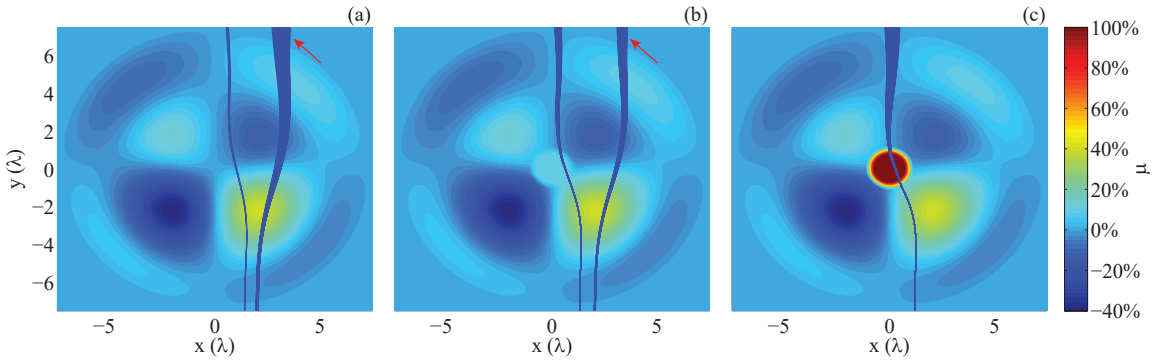

Figure 5.9: Inhomogeneous contrast maps. Map (a) is antisymmetric relative to the $x = 0$ axis and is then modified by adding a cylindrical inclusion of diameter $d = w/8$ with contrast varying from 10% (b) to 100% (c). The ray paths from the source to the receive array are shown for the different contrast levels of the cylinder. Note that the source and receive array are far from the edges of domain shown in the figure.

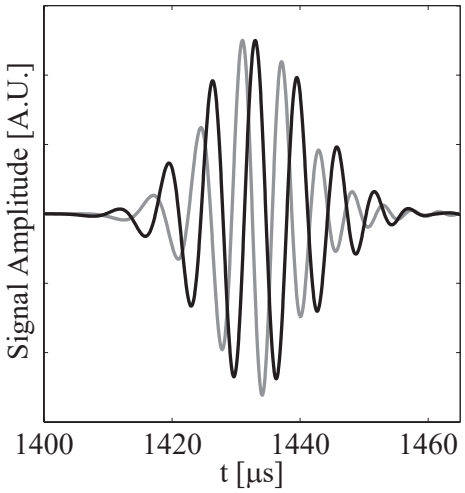

Figure 5.10: Through-transmission signals for the antisymmetric inhomogeneous medium of Fig. 5.9(a). (gray) signal propagated through the homogeneous background; (black) signal through inhomogeneous region.

shift that is -70% of the signal period while cross correlation yields -35%, thus showing that the SKT becomes inaccurate when contrast is not sufficiently small.

To study the effect of different contrast levels a circular inclusion of diameter equal to $w/8$ was introduced at the center of the inhomogeneous region as shown in Figs. 5.9(b) and (c). The contrast of the inclusion was varied from 10 to 80% while the inhomogeneous background

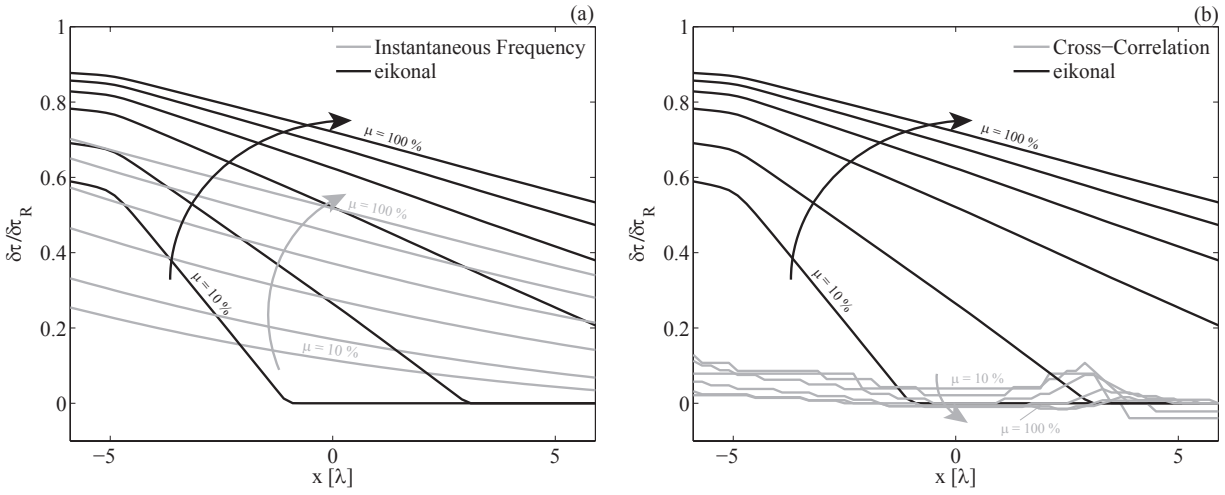

Figure 5.11: Traveltimes shifts measured along the aperture of the receive array for the inhomogeneous models shown in Fig. 5.9. Six different contrast levels of the cylindrical inclusion are simulated: 10, 20, 40, 60, 80 and 100% with the increasing contrast direction being pointed by the arrows. (a) compare the eikonal and IF traveltimes while (b) the eikonal and cross-correlation traveltimes.

was not altered. Negative contrasts were also simulated; however, the rays avoided the cylinder and therefore there was no effect on the received signals. Figure 5.11(a) compares the traveltime shifts predicted by the eikonal model and those obtained from the full wave simulations using the IF method. The traveltime shifts are relative to the inhomogeneous background of Fig. 5.9(a) and are normalized with respect to $\delta\tau_R$ [see Eq. (5.8)]. As observed in Sec. 5.3.1 the difference between the eikonal and IF traveltimes decreases as the inclusion contrast increases. While for high contrast levels the IF data follows a trend similar to that of the eikonal data, at low contrast levels (10 and 20%) the eikonal equation predicts zero traveltime shifts for some of the receivers. This can be explained by considering the ray paths from the source to the 60 receivers shown in Fig. 5.9. When there is no inclusion or the contrast is low, the group of rays pointed by the arrows does not intersect the area of the inclusion and so these rays are not sensitive to its contrast. However, as the contrast of the inclusion increases the rays veer over the inclusion which provides the path of least traveltime and the ray become sensitive to the inclusion contrast. The corresponding IF data obtained

from the full wave simulations do not show this effect due to diffraction. Finally, Figs. 5.11(b) compares the eikonal and cross-correlation data. Due to the complex contrast distribution, the wave pulses are distorted and therefore the accuracy of cross correlation in determining the traveltime shifts degrades and leads to the large discrepancies with the eikonal model. Moreover, since the diameter of the inclusion is 1/8 of the width of the sensitivity kernel, cross correlation significantly underestimates the traveltime shifts compared to the IF method.

5.4 Tomographic reconstructions

In the previous section it has been shown that traveltimes estimated from the signal first break encode more information than that obtained through the cross-correlation methods and that the ray model is more accurate than what the SKT predicts. To translate this result into the accuracy of wave speed reconstructions consideration is given to a full-view tomographic configuration in which the area of interest is enclosed within a circular array of diameter $\Delta = 225\lambda$, consisting of 100 equally spaced point-like transceivers. For such configuration the source-to-receiver distance varies depending on which transducer pair is considered. However, for small objects close to the center of the array it can be assumed that $L = \Delta$ and therefore the width of the sensitivity kernel is still $W = 15\lambda$.

The traveltimes are inverted using the curved ray tomography (CRT) method [71], which accounts for ray bending and therefore performs a fully nonlinear inversion. The forward solver is based on the eikonal equation which is solved with the fast marching method FMM. The WSM is updated using the nonlinear conjugate gradient method as explained in Willey et al. [91]. Since the forward solver is based on the FMM, the inversion adjusts the WSM so that the corresponding first arrivals match the measured traveltimes.

When performing first-arrival CRT it is important to distinguish between the cases of negative and positive contrast. In fact when the contrast is lower than μ_{cr} the first arrivals correspond to the diffracted wave pulses which are insensitive to contrast smaller than μ_{cr}.

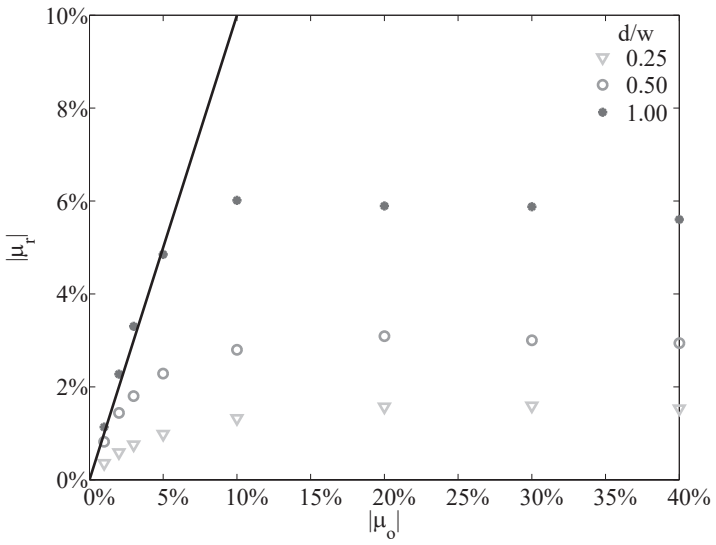

Figure 5.12: Reconstructed minimum contrast versus the nominal contrast of a uniform cylinder for three different cylinder diameter to sensitivity kernel width (d/w) ratios. The absolute values of the negative contrast are shown. The solid line corresponds to $\mu_r = \mu_0$.

This means that for $\mu < \mu_{cr}$, CRT stops updating the contrast map when the contrast reaches a value close to μ_{cr} because reducing the contrast below μ_{cr} does not affect the traveltimes predicted by the FMM. This effect is shown in Fig. 5.12 which provides the absolute value of the minimum reconstructed contrast versus the nominal one for three cylinder diameters, i. e. d/w =0.25, 0.50, and 1.00. Here, the traveltimes forming the input for CRT are calculated using the eikonal equation and therefore the data is consistent with the forward model. Therefore, CRT should achieve accurate reconstructions and all the data points should lie on the solid line $\mu_r = \mu_0$. Instead, it can be observed that for a given d/w ratio and for decreasing contrast (increasing absolute value), the reconstructed contrast begins to diverge from the true contrast and saturates around a constant value that depends on the d/w ratio. The values of contrast where the data in Fig. 5.12 starts to diverge from the true values are consistent with the values of μ_{cr} corresponding to the three d/w cases i.e. -0.8, -1.6, and -3.2%. However, the saturation levels are higher (in absolute terms) than μ_{cr} because the reconstructed cylinder diameters tends to be larger than the true diameter.

Figure 5.13 shows the maximum reconstructed contrast for a homogeneous cylinder as a

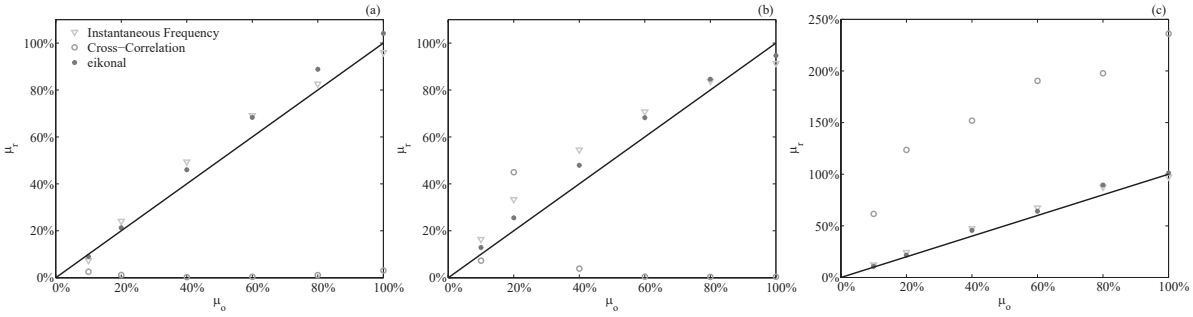

Figure 5.13: Maximum contrast of cylindrical inclusions reconstructed with curved ray tomography (CRT) as a function of nominal contrast. CRT is applied to traveltime data obtained with the eikonal model and from full wave simulations though the IF and cross correlation methods. Different cylinder diameters, d, relative to the width of the sensitivity kernel, w, are considered: (a) d/w=0.25; (b) d/w=0.5; (c) d/w=1.

function of positive nominal contrast, μ, and the cylinder diameter relative to the width of the sensitivity kernel, i. e. $d/w = 0.25$, 0.50, and 1.00. The inversion is applied to traveltime data obtained: (1) from the eikonal solver, (2) with the IF method from full wave simulations, and (3) with the cross-correlation method from full wave simulations. In all the simulations the center of the cylinder is at a 28.125λ distance from the array center to avoid artifacts due to the symmetry of the array relative to its center.

If the inversion achieved unlimited accuracy the data points would lie on the dashed diagonal line, $\mu_r = \mu_0$, and therefore the offset between the data points and the diagonal is representative of the reconstruction error. The error is due to the limited numerical accuracy of the inversion scheme and the approximation introduced by the ray model. The effect of numerical errors is demonstrated when the inversion is applied to traveltime data obtained from the eikonal model. In this case the data satisfies the ray approximation meaning that the forward model used in the inversion provides an exact representation of the data and therefore the inversion should achieved unlimited accuracy. Instead, absolute errors as large as 9% can be seen in eikonal data shown in Fig. 5.13.

The maximum contrast reconstructed from the IF data obtained from the full wave simulations provides results with accuracy similar to that obtained with the eikonal data,

in the worst case scenario the error is 10% of the nominal contrast and is observed for the largest cylinder diameter. Importantly, it can be concluded that accuracy does not degrade for cylinder diameters smaller than the width of the sensitivity kernel. On the other hand, the maximum contrast reconstructed from the cross-correlation data shows large absolute errors as high as 150%. These errors are to be expected since the traveltimes estimated by cross-correlation significantly differ from those predicted by the eikonal model.

It should be stressed that while the accuracy in maximum contrast estimations obtained with the IF data is relatively good, the spatial resolution of the reconstructions is low and leads to significant over estimations of the diameter of the cylinder as it can be seen in Fig. 5.14 which shows diametral cross-section of the contrast profiles reconstructed with CRT. It is therefore important to assess if in the presence of complex media a similar level of accuracy can be obtained. Figure 5.15 refers to the complex medium shown in Fig. 5.9(a) and shows the maximum contrast estimated for a cylinder of diameter $d = 0.25w$ at the center of the model, the corresponding reconstructed contrast profiles are shown in Fig. 5.16. The maximum contrast is estimated within the area of the cylinder and the traveltime shift data is calculated relative to the homogeneous background. Due to the complexity of the model, especially the presence of regions of negative contrast, numerical errors in the inversion lead to increased absolute contrast errors up to -41%, which are comparable to the errors resulting from the IF method. However, the errors are small compared to those obtained with the cross-correlation method which underestimates contrast severely.

5.5 Conclusions

When referring to the performance of wave-based tomographic methods it is common to assume that the accuracy of ray based tomography is limited by diffraction effects that are not accounted for by the ray model and that also cause information loss due to wavefront healing. This chapter has investigated this issue by studying the accuracy of the eikonal

equation as a forward model to predict the traveltimes of signals simulated with the full wave equation. The rationale for this analysis has been that if it were possible to estimate traveltimes from the wave pulses that are consistent with ray theory even in the presence of diffraction effects then a ray-based inversion would yield accurate results.

It has been shown that first-arrival traveltimes estimated from the eikonal equation provide an accurate representation of the propagation of a wave pulse simulated with the full wave equation as long as the traveltime of the pulse is defined based on the pulse first break. Therefore, while the standard sensitivity kernel theory (SKT) predicts that ray theory becomes inaccurate for regions of wave speed contrast over a spatial scale smaller than $W = \sqrt{\lambda L}$, where L is the source-to-receiver separation distance and λ is the wavelength, it was found that ray theory can accurately predict the arrival of the signal first break even for cylindrical objects with diameter as small as $D = W/10$ provided that the contrast is sufficiently large. On the other hand, the eikonal traveltimes significantly differed from the traveltimes extracted with the cross-correlation method. This is because cross correlation is affected by pulse distortion and most importantly by the presence of multiple pulses in the received waveform that result from complex phenomena including diffraction, multiple scattering and ray splitting that are not accounted by the first-arrival ray model. Conversely, the pulse first break is almost immune to these factors.

Whereas the first-arrival traveltimes predicted by the eikonal model are accurate for both positive and negative contrast levels, an important distinction has to be made in the case of negative contrast when considering tomography. In fact, there exists a critical contrast level, μ_{cr}, below which the first-arrival traveltimes predicted by the eikonal equation correspond to the wave pulses diffracted around the region of low contrast. Since these pulses do not travel through the region they do not encode information about its contrast level. As a result, the inversion cannot reconstruct contrast levels below μ_{cr}. This represents the main physical limitation of ray tomography based on first-arrival traveltimes and is dictated by the value of μ_{cr} introduced in this chapter rather than the resolution scale $\sqrt{\lambda L}$.

The possibility of reconstructing contrast maps for objects smaller than $\sqrt{\lambda L}$ has been investigated in the case of positive contrast by considering the accuracy of curved ray tomography (CRT) when evaluating maximum contrast. It has been shown that CRT applied to first arrival data extracted from full wave simulations leads to accuracy which is comparable to the numerical accuracy of the inversion. On the other hand, CRT applied to traveltime data extracted with the cross correlation method provided highly inaccurate estimates as predicted by the SKT. This proves that the effects of diffraction and other physical phenomena that are not accounted for by ray theory can be mitigated by defining the pulse traveltime based on its first break.

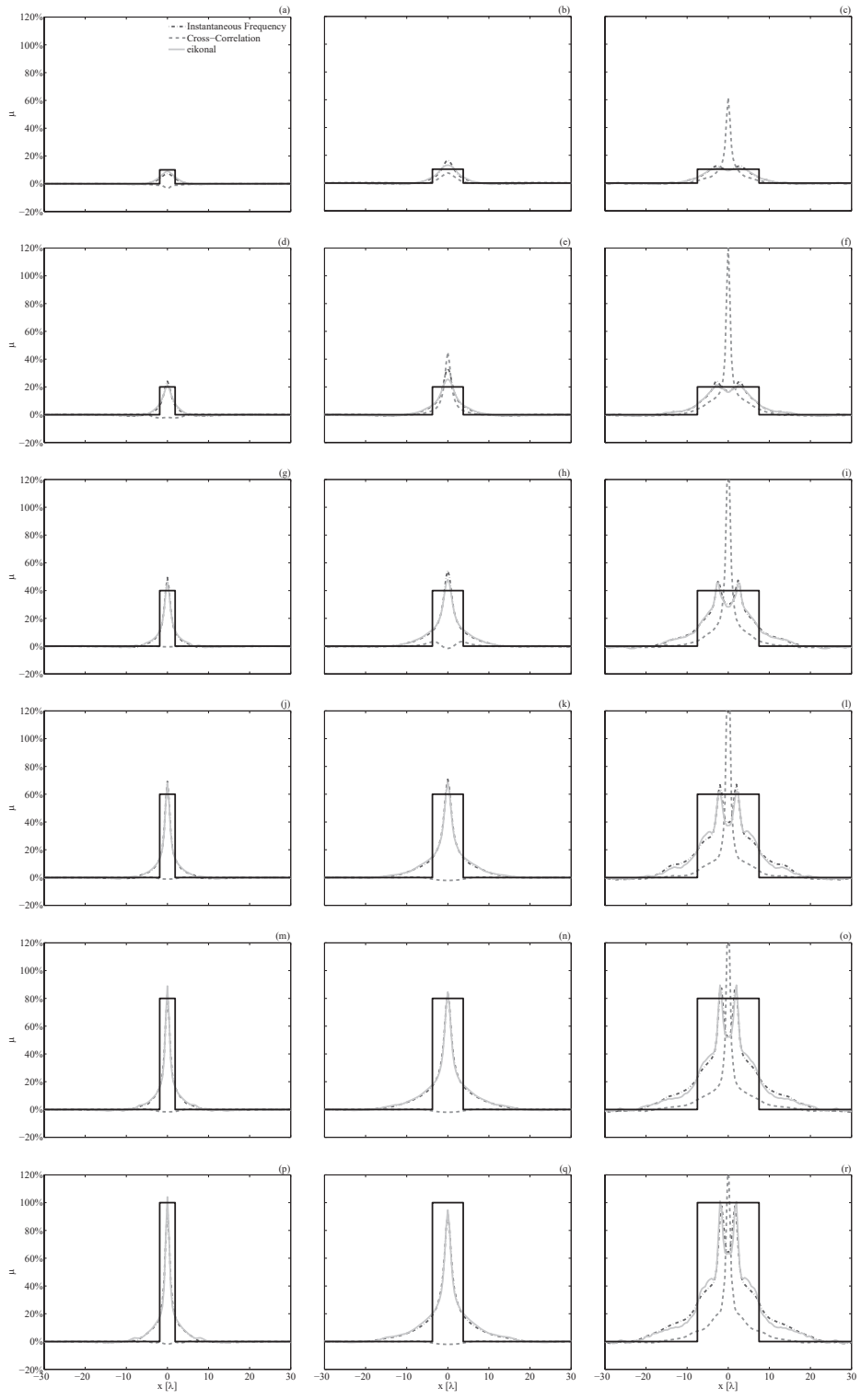

Figure 5.14: Reconstructed contrast profiles corresponding to the data shown in Fig. 5.13. The columns correspond to d/w =0.25, 0.50 and 1.00, while the rows correspond to contrast levels of 10, 20, 40, 60, 80 and 100% from top to bottom. (black solid lines) true contrast profile, (gray curves) CRT applied to eikonal data, (dash-dot curves) CRT applied to IF data obtained from full wave simulations, (dashed curves) CRT applied to cross-correlation data.

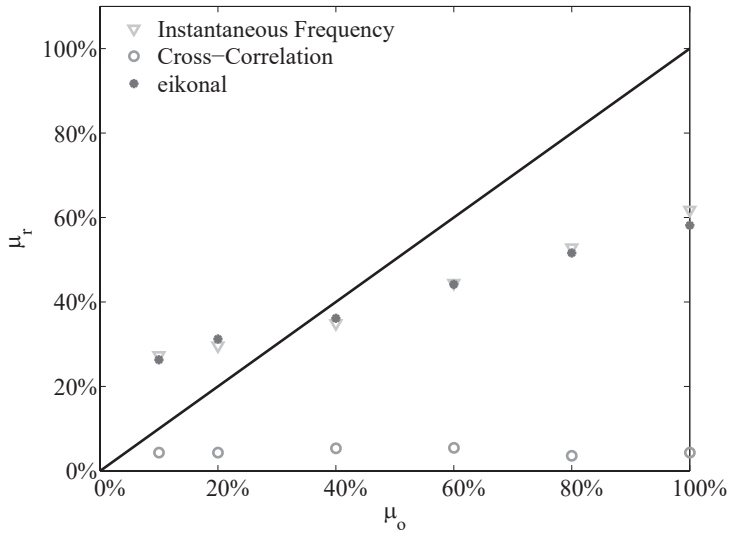

Figure 5.15: Reconstructed maximum contrast for a cylindrical inclusion of diameter d/w=0.25 at the center of the inhomogeneous model of Fig. 5.9(a) as a function of the cylinder nominal contrast. CRT is applied to traveltime data obtained with the eikonal model and from full wave simulations though the IF and cross correlation methods.

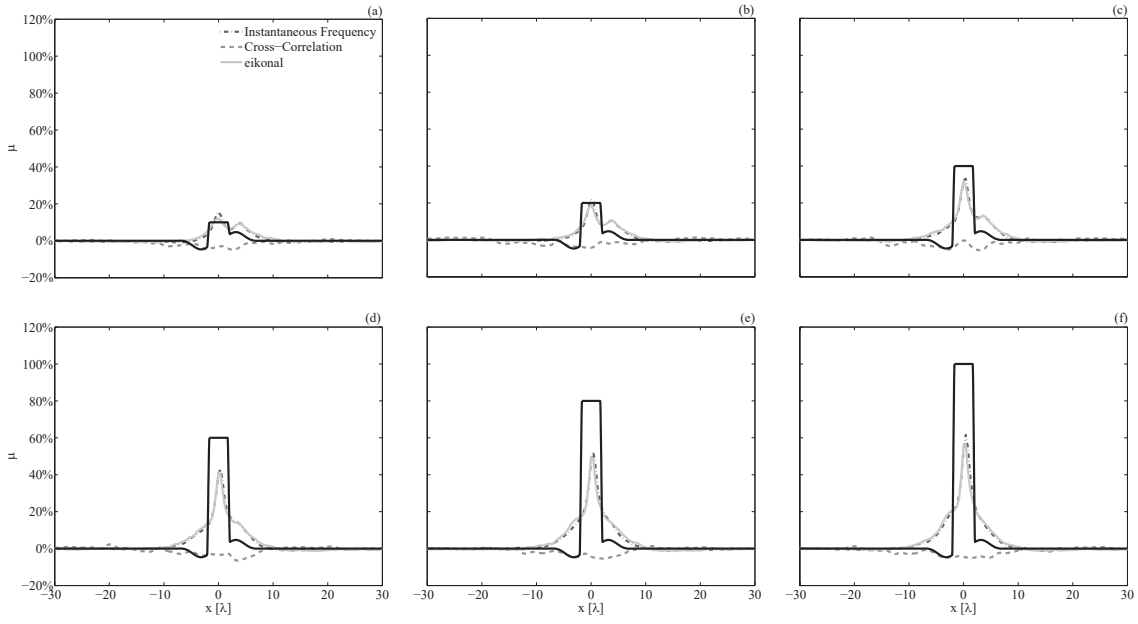

Figure 5.16: Reconstructed contrast profiles along the $y = 0$ axis for the inhomogeneous medium of Fig. 5.9 and for different values of the contrast of the cylindrical inclusion. (black solid lines) true contrast profile, (gray curves) CRT applied to eikonal data, (dash-dot curves) CRT applied to IF data obtained from full wave simulations, (dashed curves) CRT applied to cross-correlation data.

Chapter 6

Performance analysis of GWT

6.1 Introduction

Central to the goal of using GWT as an effective tool in the field, is the task of defining the range of its applicability to pipes, arrays, and defects of varying size. The form of GWT studied in this thesis is based on CRT, which is based on ray theory. Traditionally, the relationship between defect size and the sensitivity kernel width (i.e. the width of the first Fresnel zone [43, 44]) has been the measure by which ray theory is deemed applicable. However, in Chapter 5 the critical contrast criterion, was shown to determine whether the contrast defining an inclusion can be accurately reconstructed.

There was a distinct difference shown in the ability of CRT to reconstruct fast (positive contrast) and slow (negative contrast) inclusions. Fast inclusions were able to be reconstructed with high accuracy for defect width scales significantly smaller than the largest Fresnel zone width in the array. This comparison is reasonable since the defects studied were near the center of the circular full view array where the relevant Fresnel zone widths would be near the largest. For the case of two parallel linear arrays, as in cross borehole tomography or GWT in pipes, the sizes of the Fresnel zone widths that encounter contrast may vary greatly. Thus, there is a need to determine how the critical contrast theory can be

applied for linear limited view arrays.

As previously mentioned, the linkage between thickness and wave speed studied in this thesis is based on the CGV method [27,28]. The CGV method is meant to hold the A_0 Lamb mode group velocity nearly constant by operating in a region of frequency-thickness (centered about the CGV point) where the group velocity curve is relatively flat. This ensures that the A_0 Lamb wave pulses arrive at the same point in time over a range of WTL, which greatly simplifies data processing. The A_0 phase velocity is used to encode defect data in the pulses (i.e. defect data is captured as a pulse phase shift) as it is sensitive to WTL over the same range of frequency-thickness near the CGV point. The A_0 phase velocity curve is monotonically increasing, thus thickness loss corresponds to a decrease in frequency-thickness and phase velocity. This means all defects (i.e. WTL) will be characterized as a slow contrast region. In Chapter 5, it was shown that there is a critical contrast that cannot be surpassed when reconstructing slow inclusions. This leads to a certain saturation level (the critical contrast) that is dependent upon the width normalized by array diameter. Again, the defect width being normalized by array diameter is justified in this case because the defects were near the center of the array, and thus represented a worst case scenario for that particular array configuration. In the case of two parallel linear arrays, multiple path lengths must be incorporated somehow into the calculation of critical contrast.

The critical contrast can be recast in terms of defect depth, δ, relative to the nominal wall thickness, t, using the dispersion curve of A_0. Specifically, the relationship that links the phase velocity to the frequency-thickness product, $f \cdot t$, can be transformed into an equivalent expression that now links δ/t to the phase velocity contrast resulting from the WTL δ - assuming that for δ=0, $f \cdot t$=1.4 MHz-mm which corresponds to the CGV point. This new relationship is given in Fig. 6.1 and shows that the contrasts (its absolute value is shown) remains below 30% for defect depth up to 70% and subsequently increases to 100% for deeper defects. Based on the results from Chapter 5, given a certain defect width, w, and source to receiver separation distance, L, the critical contrast is determined using Eq. 5.9.

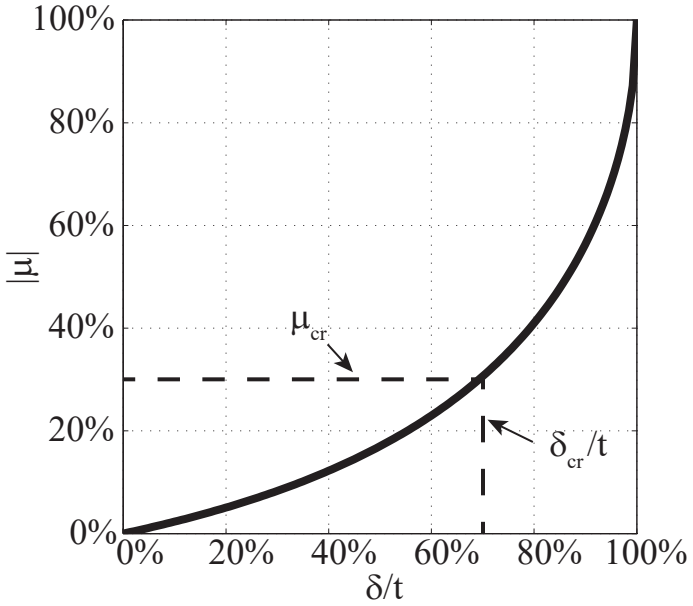

Figure 6.1: Absolute value of the A_0 Lamb wave phase velocity contrast, μ, given the nominal phase velocity coincides with the CGV point (i.e. $f{\cdot}t = 1.4$ MHz-mm), in terms of normalized defect depth, δ/t.

Subsequently, the curve in Fig. 6.1 can be used to determine the corresponding value of the critical defect depth, δ_{cr}, beyond which ray tomography is no longer sensitive to a depth increase. This representation of the critical contrast criterion in terms of defect depth will be referred to as the critical defect depth criterion.

While it is clear that the critical defect depth has implications on the effectiveness of GWT, there are other practical factors that must also be considered, such as pipe, array, and defect sizes. Thus, the focus of this chapter will be to translate the results from Chapter 5 to the case of damage detection (corrosion/erosion) using CRT based GWT in pipes, as well as considering the other practical parameters defining the GWT problem, and its accuracy. The remaining sections of this chapter will be: Sec. 6.2 studying parameters of the GWT problem, containing Sec. 6.2.1 studying pipe parameters, Sec. 6.2.2 studying defect parameters, Sec. 6.2.3 studying array parameters, and Sec. 6.3 containing conclusions.

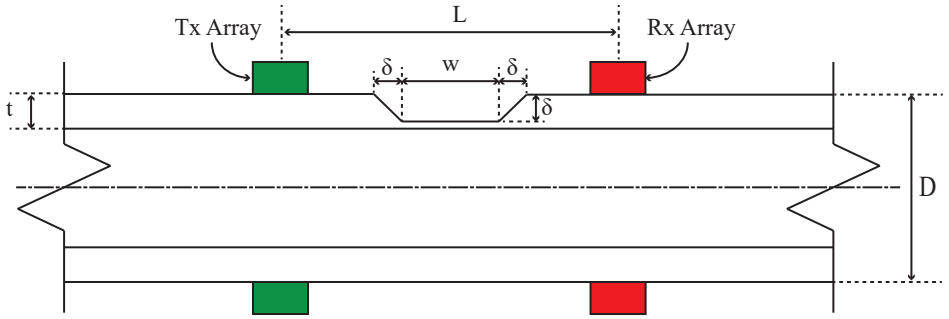

Figure 6.2: Schematic of pipe with arrays and defect profile.

6.2 Study of GWT problem parameters

In this section, the parameters important to GWT are grouped in three categories: pipe (diameter, D, and nominal wall thickness, t), defect (width, w, and depth, δ), and array (separation of ring arrays, L, and number of transducers per array, N). The thickness of each pipe is represented with an equivalent acoustic model, as discussed in Chapter 3. Each modeled defect has a small boundary around them equal in thickness to the defect depth, to provide a smooth transition between nominal and defect thicknesses, as shown in Fig. 6.2. The relationship between the acoustic wave speed and the pipe thickness is dependent on the A_0 Lamb mode phase velocity dispersion curve, as described in Chapter 3.

Three nominal pipe sizes (NPS) are studied: 8" schedule 40, 8" schedule 120, and 16" schedule 40. For each of these, a set of defects of prescribed width and depth are investigated. The studied defect widths, w, will be multiples (1/4, 1/2, 1, and 2) of $\sqrt{\lambda L_{avg}}$ where, L_{avg} is the average straight line distance between sources and receivers (including virtual ones). The studied nominal defect depths, δ, are 5, 10, 20, 30, 50, and 80% of nominal pipe thickness, t. Finally, for each of these combinations, the source and receiver array separation will be studied as multiples (2,3, and 4) of pipe diameter, D, and the number of transducers per array, N. The number of transducers per array, will be such that three levels of array element spacing exist for each pipe diameter. This results in the number of transducers per array for 8" schedule 40 and 120 pipes being 4, 8, and 16, and in the 16" schedule 40 pipe being 8, 16, and 32.

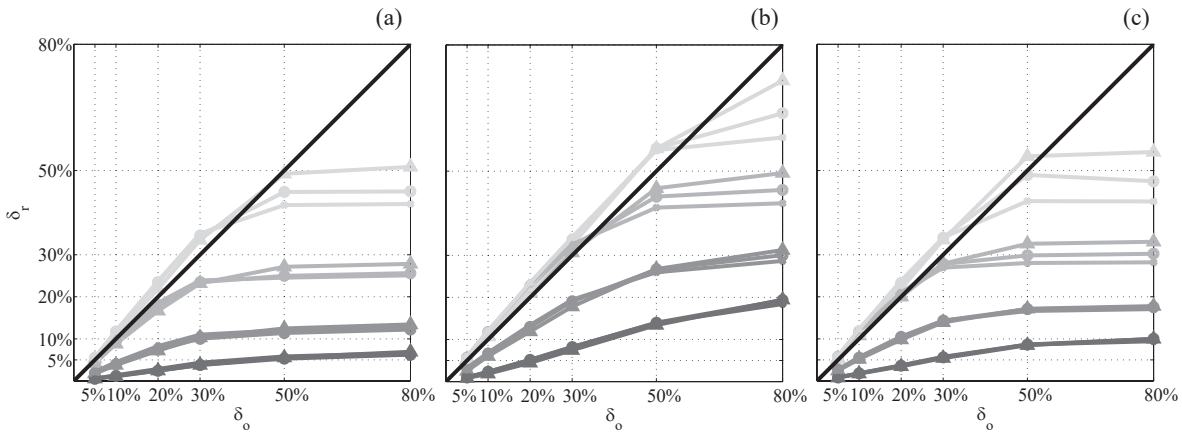

Figure 6.3: Performance characterized as the agreement between the nominal defect depth, δ_o, and reconstructed δ_r. The level of gray moves from dark to light for increasing defect width: $w = 1/4$, $1/2$, 1, 2 multiples of $\sqrt{\lambda L_{avg}}$. The marker faces ($\times$, $\circ$, $\triangle$) correspond to the array separation: $L = 2D$, $3D$, $4D$. Data for 8" schedule 40 (a), 8" schedule 120 (b), and 16" schedule 40 (c) are shown. The black line represents perfect performance where $\delta_r = \delta_o$.

Simulations are carried out using an acoustic time domain finite difference method discussed in Sec. 3.2. Each simulation runs for 1.3 hours on average. It should be noted however that the acoustic model only provides a partial representation of wave pulse propagation in an actual pipe wall. Notably, the pulse distortion due to guided wave dispersion is not simulated. As a result, different traveltime picking methods are required to process the simulated and experimental data. In the simulations we continue to use the IF method as in Chapter 5 while we process experimental data using the zero-crossing method as explained in Sec. 4.3.1. The traveltime data is then inverted using the same GWT method studied in Chapter 3 employing up to the second order helical mode.

6.2.1 Effect of pipe parameters

The results of maximum defect depth reconstructions presented in this section are based on 16 physical transducers per array, and consider helical modes up to the second order. Figure 6.3 shows the reconstructed maximum defect depth, δ_r, as a function of the nominal defect depth, δ_o, where the level of gray moves from dark to light for defect widths, w, of $1/4$, $1/2$, 1, and 2 multiples of $\sqrt{\lambda L_{avg}}$, and marker symbols ($\times$, $\circ$, $\triangle$) correspond to the array

NPS	t	λ
8" SCH 40	7.37 mm	16 mm
8" SCH 120	18.24 mm	38 mm
16" SCH 40	12.7 mm	27 mm

Table 6.1: Wavelength, λ, and nominal thickness, t, for each pipe.

separation, L, of $2D$, $3D$, and $4D$. Each set of data shown in Figs. 6.3(a)-(c) correspond to the 8" schedule 40, 8" schedule 120, and 16" schedule 40 pipes respectively. Notice in Fig. 6.3 that the two darkest gray lines correspond to defect width of 1/4 and 1/2 of $\sqrt{\lambda L_{avg}}$, and thus their performance is expected to be lacking via sensitivity kernel theory, but for the two lightest gray lines, there is good agreement between nominal defect depth, δ_o, and reconstructed defect depth, δ_r, up to a particular point on the nominal depth axis that shifts for each individual curve.

The obvious comparison to point out is between the 8" schedule 40 and 120 pipes shown in Figs. 6.3(a) and (b). Both have the same diameter and thus array separations, number of transducers per array, and defect depths as percentage of nominal thickness (i.e. contrasts) are also the same. This leaves only the defect widths as the root cause of differences between the reconstructed defect depth, δ_r, and the nominal defect depth, δ_o, resulting from the defect widths dependence on $\sqrt{\lambda L_{avg}}$.

In terms of this study, the main contribution of pipe thickness is to the determination of the wavelength. This is due to the CGV method being central to GWT. Thus, increasing thickness leads to decreasing frequency and ultimately increasing wavelength, as shown in Tab. 6.1. This leads to the defect widths in the 8" schedule 120 pipe being wider than those in the 8" schedule 40 pipe. This points to the observation that even though all parameters (other than width) are the same in the two examples, and the defect widths correspond to the Fresnel zone width in the same way, there is increased performance (i.e. δ_r matches δ_o for a wider range of defects in Fig. 6.3) in the case where the wavelength is longer. This implies that the width of the defect is more important than its relationship to the Fresnel zone width, or wavelength.

It should also be true that if the defect widths are the same in the 8" schedule 40 and 120 pipes than the inputs (based on first-arrival traveltimes) to the two problems would be nearly identical, and thus the result of GWT would be the same in spite of the difference in wavelength/Fresnel zone width. This is demonstrated in the results shown in Fig. 5.13 where the reconstructed contrasts obtained using the eikonal and IF solver data are similar.

Most importantly, the saturation of the reconstructed depth, δ_r, occurs in all cases (even those where widths are greater than the Fresnel zone width) which implies that the Fresnel zone limit is insufficient to serve as the only criterion for predicting the accuracy of GWT reconstructions. These observations, particularly those regarding the influence of defect width, will be studied in greater detail in the section on defect parameters.

6.2.2 Effect of defect parameters

In this portion of the study, the CGV method must again be considered as it prescribes the link between wave speed and pipe wall thickness. Consequentially, defect depth as a percentage of nominal wall thickness is equivalent in terms of contrast across all pipes. This normalization of defect depth, and equivalence of it to the contrast, provides a convenient way of comparing the accuracy of the reconstructed maximum WTL. Furthermore, it means that both the critical contrast, and critical depth curves are universal for all pipe and defect sizes, when width is properly normalized. The purpose of this section is to investigate this claim.

Defect width dependence on the first Fresnel zone width computed with respect to L_{avg}, rather than the separation distance of the source and receiver arrays, L, was implemented to ensure more than just the direct (shortest path) source-receiver pairs would encode accurate information about the defect interior as predicted by the sensitivity kernel theory. As previously mentioned, the use of the CGV method is that increasing pipe thickness leads to increasing wavelength, which per the definition of defect size leads to larger defect widths in thicker pipes.

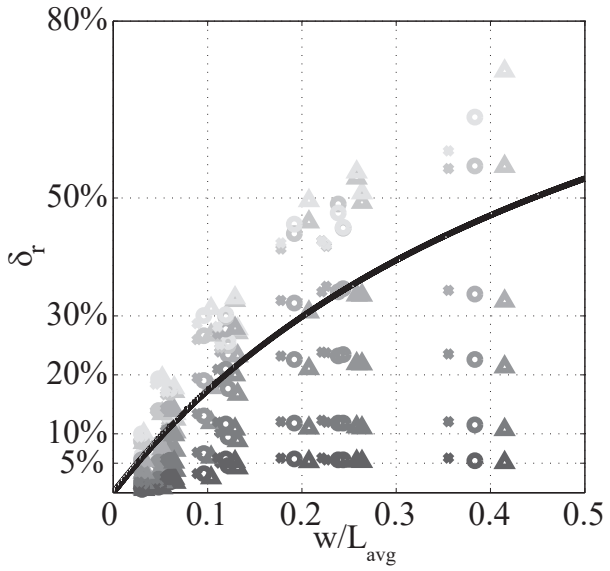

Figure 6.4: Performance characterized as the agreement between the nominal defect depth, δ_o, shown as the horizontal grid lines, and reconstructed, δ_r. The level of gray moves from dark to light for increasing defect depth: δ = 5, 10, 20, 30, 50, and 80% of wall thickness. The marker type ($\times$, $\circ$, $\triangle$) correspond to the array separation: $L = 2D$, $3D$, $4D$. Data is the same as that shown in Fig. 6.3. The black line corresponds to the δ_{cr} criterion.

The existence of a critical defect depth criterion, suggests that the there will be similar performance for defects of similar normalized size (i.e. size relative to the size of the pipe and array dimensions). The consequence of the equivalence between normalized WTL and wave speed contrast, shown in Fig. 6.1, should be that all GWT performance can be described by the critical defect depth for any combination of pipe and defect.

Figure 6.4 shows the data from Fig. 6.3 reorganized so that the reconstructed defect depth, δ_r, is a function of normalized defect width, w/L_{avg}, where marker symbols ($\times$, $\circ$, $\triangle$) correspond to the array separations ($2D$, $3D$, $4D$), the level of gray corresponds to the nominal defect depth (5, 10, 20, 30, 50, and 80% of wall thickness), and the critical defect depth is shown as a solid black line. It should be noted that in the analysis shown in Fig. 6.4, the normalized width is due only to the deepest part of the defect, and the portion due to the boundary is neglected. The normalization of width by L_{avg} is done as a simple way to incorporate not only the shortest ray paths, but also many of the longer ray paths into the

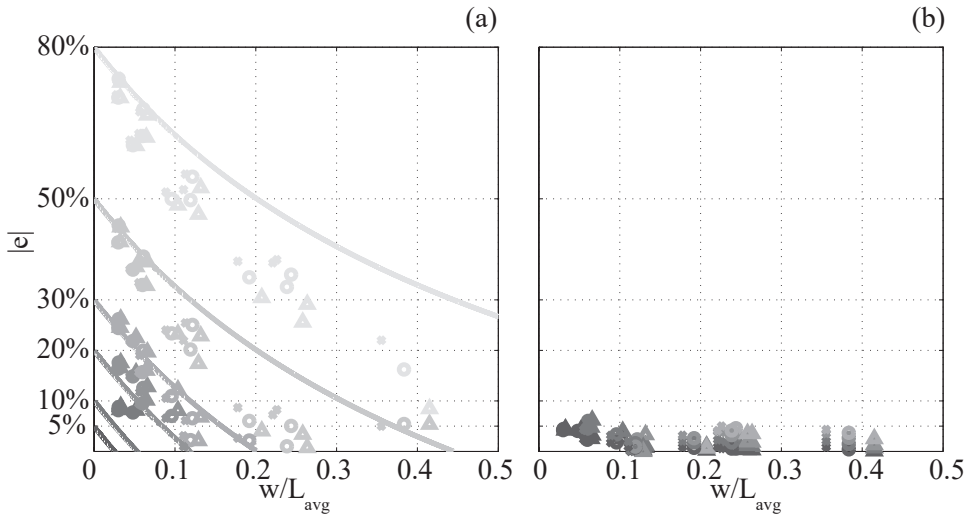

Figure 6.5: Performance characterized as the absolute value of error, $|e|$, as a function of normalized defect width, w/L_{avg}, for defects outside of (a), and within (b) the δ_{cr} curve shown in Fig. 6.4. The level of gray moves from dark to light for increasing defect depth: δ = 5, 10, 20, 30, 50, and 80% of wall thickness. The solid curves in (a) are the analytical error curves calculated using the critical defect depth, shown in Fig. 6.4, substituted into the δ_r term in Eq. 6.1 for each nominal defect depth, δ_o. The marker type ($\times$, $\circ$, $\triangle$) correspond to the array separation: $L = 2D$, $3D$, $4D$.

calculation of the critical defect depth curve, δ_{cr}.

In Fig. 6.4, defects whose nominal sizes are outside the critical defect depth curve are observed as the points that accrue just above the critical defect depth curve. However, for defects within the critical level, the maximum reconstructed defect depth is predicted with a reasonable level of accuracy. This is observed as the convergence of the reconstructed defect depths, δ_r, towards the nominal defect depth, δ_o, represented as the horizontal grid lines. This confirms the assertion that the critical contrast theory applies to GWT reconstructions, and that it is usable as a universal table, as the data shown in Fig. 6.4 is from all combinations of defect and pipe size explored in this section.

To quantify performance the normalized maximum depth error is introduced as

$$e = \frac{\delta_r - \delta_o}{t}. \tag{6.1}$$

Figure 6.5 shows the error, e, for two groups of defects: those whose prescribed nominal

sizes are outside of the critical defect depth in (a), and those whose nominal sizes are within the critical defect depth in (b). The solid lines in Fig. 6.5(a), correspond to analytical error curves constructed by substituting the critical defect depth curve, shown in Fig. 6.4 into δ_r in Eq. (6.1), for a particular nominal defect depth, δ_o, where the darkness of the line indicates the level of δ_o. The drift between the error data points and analytical error curves in Fig. 6.5(a) is due to the convergence of the reconstructed defect depth, δ_r, towards a value slightly larger than the critical defect depth, δ_{cr}, when $\delta_o > \delta_{cr}$, but over all there is good agreement, which suggests that for defects whose nominal size is outside of the critical defect depth curve the majority of the error can be attributed to the saturation of reconstructed defect depth near the critical defect depth. Most notably, in Fig. 6.5(b), the absolute value of error is always low, and consistently stable across all widths. In this regime the maximum absolute error is approximately 6%.

6.2.3 Effect of array parameters

In this section, only the errors of defects whose nominal size is within the critical defect depth criterion will be considered in order to focus the study on the impact array parameters have on the error in the reconstructed defect depth. This section will study both array separation, L, and number of transducers per array, N, as it pertains to error, e, described in Eq. (6.1). In Fig. 6.6 the data is described using box plots shown in black, mean error shown as dark gray dots, and standard deviation error bars as light gray lines extending vertically from the mean error dots. The data spread, and mean error increases slightly (less than 3%) in all cases with increasing array separation. The low level of dependence on array separation, indicates that there could be the potential to monitor larger sections of pipe between the source and receiver arrays. Figure 6.7 displays the errors shown in Fig. 6.6 rearranged as a function of normalized defect width, w/L_{avg}, so that (a)-(c) correspond to a particular array separation, L. The solid black line corresponds to the error estimate, obtained by fitting the

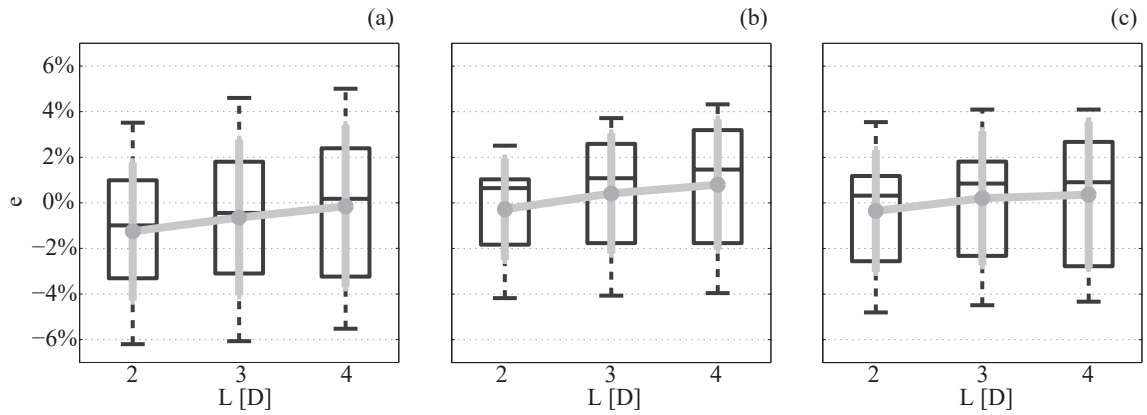

Figure 6.6: Performance characterized as signed error, e, in terms of array separation, L for all defect width and depth combinations within the δ_{cr} curve. The error for each L, is represented by the average error (dark gray dot), standard deviation error bars (light gray bars extending vertically from the average error), plotted over box plots (black) characterizing the spread of the data. The 8" schedule 40 (a), 8" schedule 120 (b), and 16" schedule 40 pipe results are shown.

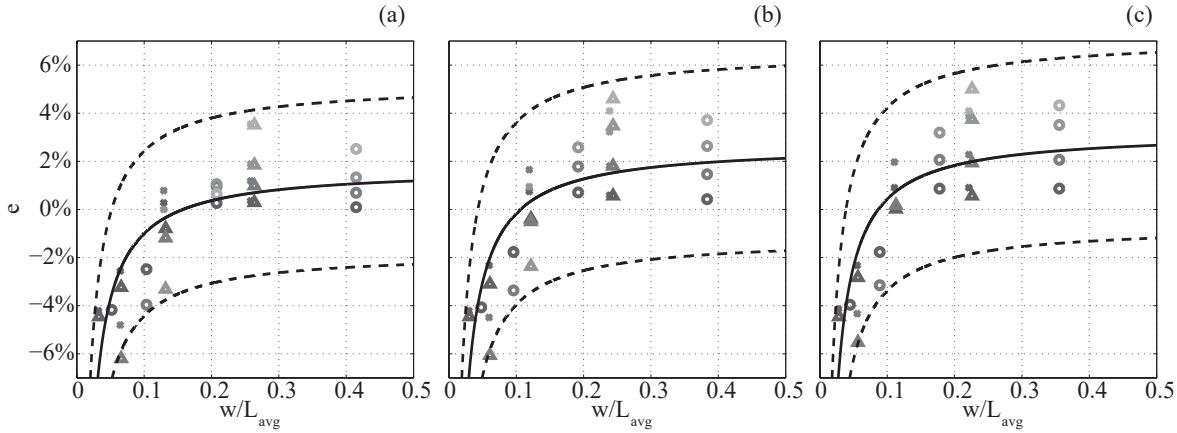

Figure 6.7: Performance characterized as signed error, e, in terms of normalized defect width, w/L_{avg}, for all defect width and depth combinations within the δ_{cr} curve. The marker type ($\times$, $\circ$, $\triangle$) correspond to the 8" schedule 40, 8" schedule 120, and 16" schedule 40 pipe results. The level of gray moves from dark to light for increasing defect depth consistent with Fig. 6.5. The solid black line and dotted black lines correspond to the fitted error curve, and nonsimultaneous prediction bounds (based on 95% confidence interval). The array separations, $L = 2D$, $3D$, $4D$, are shown in (a)-(c) respectively.

data for each array separation independently using the assumed regression model

$$\hat{e} \approx a + b/(w/L_{avg}), \tag{6.2}$$

where, a and b are the tunable parameters, and the dotted curves are nonsimultaneous prediction bounds based on a 95% confidence interval. These bounds predict the range of error that can be expected in the reconstructions based on normalized defect width.

By considering the signed error it is obvious that there is a cross-over point at which the maximum reconstructed defect depth transitions from underestimations to overestimations. The underestimations grow with decreasing normalized defect width, w/L_{avg}, and overestimations reach a stable level above the cross-over point.

The regression analysis carried out on each set of error data associated with a particular array separation L individually shows the cross-over point shifts towards increasingly larger values of w/L_{avg} (from, 8.7% to 10.7%, to 15.8%) for decreasing array separations. The cross-over point is determined by setting the error estimated by the regression model equal to zero, $\hat{e} = 0$, and solving for normalized defect width, w/L_{avg}. It is observed that the fitted error curve and the 95% confidence intervals shift by less than 2% error with increasing array separation, thus it is confirmed that the error does not change significantly for the increasing array separations.

Due to the lack of sensitivity of the error relative to the array separation, observed in Fig. 6.7, the error data is combined in Fig. 6.8, and a regression fit analysis is performed for all data simultaneously. Coefficients are determined to be (with 95% confidence bounds): $a = 2.472(1.886, 3.059)$, and $b = -0.2739(-0.321, -0.2268)$. From this analysis it is determined that the cross-over point is 11% normalized defect width. The error for $w/L_{avg} > 11\%$ converges towards a stable level of error ($\approx 2.5\%$), and the error for $w/L_{avg} < 11\%$ is increasingly negative for decreasing normalized width.

It is observed in Fig. 6.8 that the errors from common pipes (pipe type is indicated by

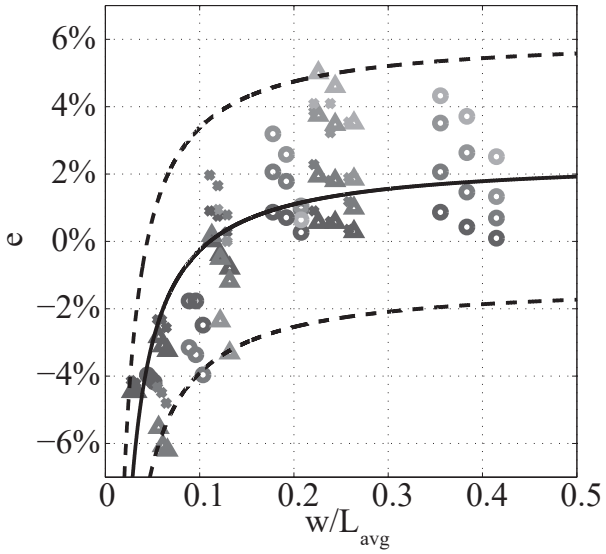

Figure 6.8: Performance characterized as signed error, e, in terms of normalized defect width, w/L_{avg}, for all defect width and depth combinations within the δ_{cr} limit. The marker type ($\times$, $\circ$, $\triangle$) correspond to the 8" schedule 40, 8" schedule 120, and 16" schedule 40 pipe results. The level of gray moves from dark to light for increasing defect depth consistent with Fig. 6.5. The solid black line and dotted black lines correspond to the fitted error curve, and nonsimultaneous prediction bounds (based on 95% confidence interval). This figure combines all data from Fig. 6.7.

NPS	$2D$	$3D$	$4D$
8” SCH 40	0.12 m	0.13 m	0.14 m
8” SCH 120	0.19 m	0.20 m	0.22 m
16” SCH 40	0.21 m	0.22 m	0.24 m

Table 6.2: Fresnel zone widths, $\sqrt{\lambda L_{avg}}$, for each pipe, and separation.

NPS	$2D$	$3D$	$4D$
8” SCH 40	0.89 m	1.04 m	1.21 m
8” SCH 120	0.89 m	1.04 m	1.21 m
16” SCH 40	1.60 m	1.87 m	2.18 m

Table 6.3: L_{avg}, for each pipe, and separation.

marker symbol) and multiple defect depths (indicated by level of gray) collect in groups near a common normalized defect width. The slight change in normalized defect width observed in each group is due to the effect of the separation distance L. Defect widths are defined in this study as multiples of $\sqrt{\lambda L_{avg}}$. The influence of L_{avg} on $\sqrt{\lambda L_{avg}}$, can be examined by comparing each element of Tab. 6.3 to the corresponding one in Tab. 6.2. The normalized width, w/L_{avg}, can be expressed as a multiple of $\sqrt{\lambda/L_{avg}}$. Thus as L increases so does L_{avg}, but in each group normalized defect width actually decreases with increasing L. Ultimately, this supports the concept that reconstructions are most sensitive to the normalized defect width, rather than the width of defect or separation distance alone.

The final array parameter to be addressed is the number of transducers per array, N. There is no stringent requirement for wavefield sampling (i.e. therefore array element spacing) in the case of ray tomography. For this reason, a study is carried out here to determine an optimal number of transducers to be used in the case of GWT, for the set of studied defect and pipe sizes. Figure 6.9 presents a break down of all errors in reconstruction in the same format as Fig. 6.6, where each column corresponds to a particular pipe size, and each row corresponds to an array separation. Decreasing the number of transducers causes in all cases a shift towards underestimations of defect depth (i.e. negative error). The shift in error between 8” schedule 40 and 120 pipes is most likely explained by the difference in

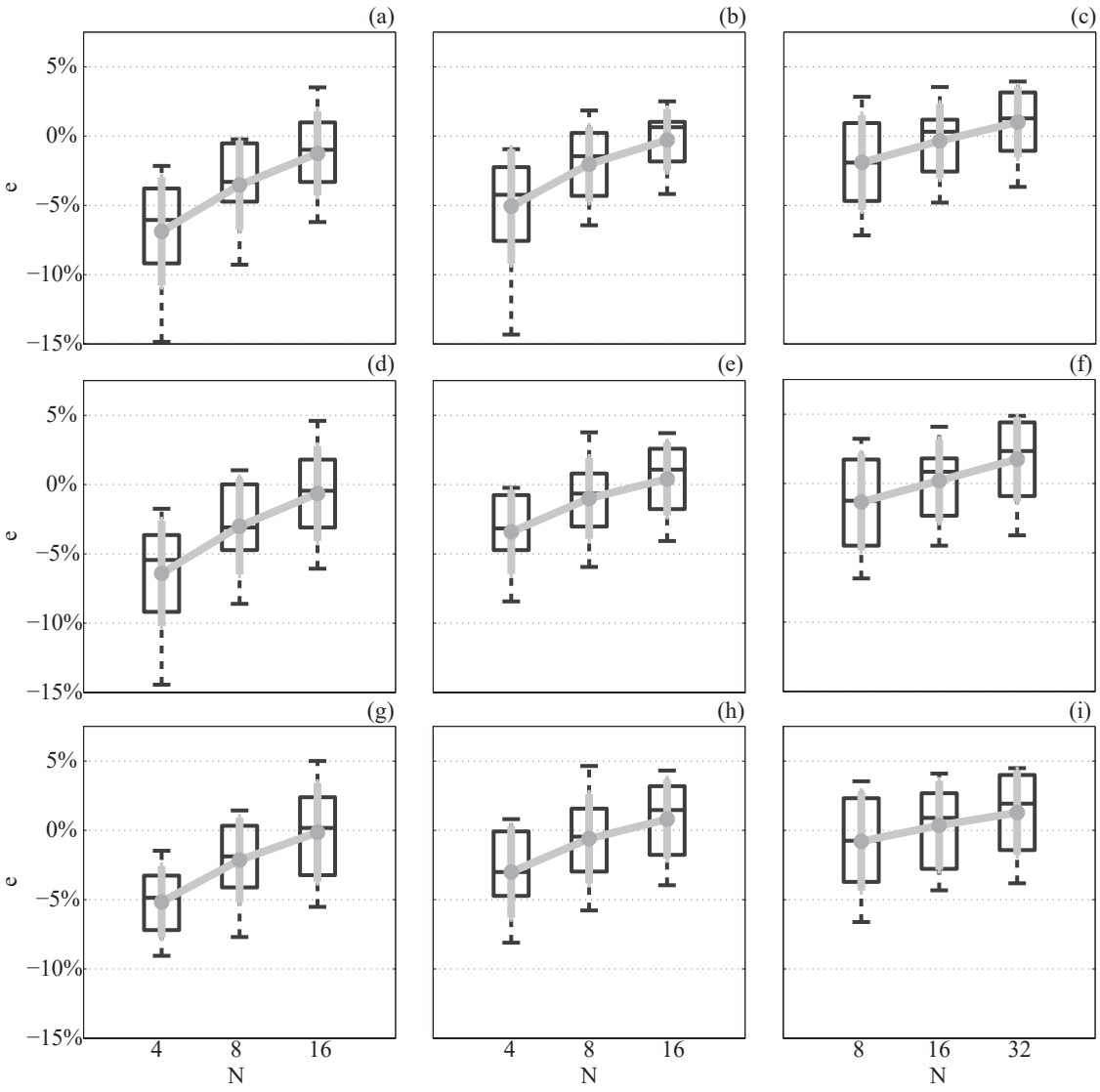

Figure 6.9: Performance characterized as signed error, e, in terms of number of transducers, N, for all defect width and depth combinations within the δ_{cr} limit. The error for each N, is represented by the average error (dark gray dot), standard deviation error bars (light gray bars extending from the average error), plotted over box plots (plotted in black) characterizing the spread of the data. Each column corresponds to the type of pipe: 8" schedule 40, 8" schedule 120, 16" schedule 40 moving left to right. Each row corresponds to the array separation: $L = 2D$, $3D$, $4D$ moving top to bottom.

defect widths. The decrease in the spread of the error between the 8" schedule 120 and 16" schedule 40, is accounted for by the fact that double the number of transducers were used in the 16" schedule 40 pipe case. When comparing the error spread across pipes, for common array separation and transducer number (e.g. 16), the spread and average error

are similar. This implies that the angle between transducers (or number of them) in a ring array, rather than the absolute spacing between them, is the measure of element spacing that should be used in evaluating the level of performance. Most importantly, for cases where $N > 8$, the average error is near zero. Also, the spread is relatively low (approximately 10%) when $N > 8$, indicating acceptable performance. For this reason, the minimum number of transducers per array recommended for GWT reconstruction accuracy is 16 with regards to the pipe, defect, and array combinations studied here.

6.3 Conclusions

In this chapter, relationships between pipe, defect, and array geometries were examined in order to determine their impacts on the accuracy of the maximum WTL reconstructed by GWT. The first Fresnel zone width (with respect to L_{avg}) is not by itself enough to determine the accuracy of GWT reconstruction based on CRT. This is demonstrated by the saturation of the reconstructed defect depth, δ_r, that is observed for increasing nominal defect depth, δ_o, shown in Fig. 6.3. This occurs even for widths as great or greater than $\sqrt{\lambda L_{avg}}$. There is a considerable amount of error in reconstructed defect depths for those defects whose nominal size is outside of the critical defect depth curve, as shown in Fig. 6.5. In these cases, the fact that reconstructed defect depths converge towards values near the corresponding critical defect depth value further confirms the concept that GWT performance is limited by the critical defect depth criterion.

Furthermore, it is demonstrated the critical defect depth criterion is universal for all GWT configurations when the normalization occurs relative to L_{avg}. Additionally, reconstructions of a particular defect can be evaluated by finding its normalized width, and maximum reconstructed depth, and comparing these against the critical depth curve. This will give the user of GWT some idea of whether the critical depth has been reached, and if the particular reconstruction is accurate.

It is also observed that defect width has a consequence other than determining the limiting value of depth that can be reconstructed. For normalized defect width, w/L_{avg}, there is a cross-over point at 11%, where defects shift from being underestimated, to being overestimated. For $w/L_{avg} < 11\%$ the error decreases with increasing w/L_{avg}. For $w/L_{avg} > 11\%$ the estimated error curve converges towards 2.5%, and the error is no more than 5%.

Finally, when considering the number of elements in the ring array, the number of transducers rather than the absolute spacing between them is determined to be the most consequential factor. Because the 8" schedule 40 pipe had the smallest defect in widths, and its performance was only comparable to the other two pipes for the case of 16 transducers per array, it is concluded that this is the minimum number of elements required for acceptable accuracy (for the set of studied defects). In all pipes performance was acceptable (i.e. the maximum absolute error is 6%) for 16 transducers. Even in the case where 32 transducers are available, the decrease in spread of error/shift of average error, was not substantial, thus 16 transducers per array is a good trade off between accuracy, and cost.

Chapter 7

Conclusions

7.1 Review

A full characterization of the performance of curved ray tomography (CRT) based guided wave tomography (GWT) was undertaken in this thesis, as well as improvements made to increase accuracy in order to yield highly accurate reconstructions of the maximum wall thickness loss (WTL). Chapter 1 explained that the need for a highly accurate WTL structural health monitoring system is based in the necessity to evaluate damage in oil and gas assets in order to provide the WTL rate needed as an input to corrosion mitigation strategies.

Chapter 2 reviewed the theory of guided waves. It began with an example of an optical guided wave, and then transitioned to the case of elastic wave theory. The types of guided waves available to plates were explored, along with an explanation of dispersion. Next, guided waves in pipes were reviewed, and links to the modes in plates were pointed out. Finally, justification was given for the selection of the A_0 Lamb mode to be used as the probing wave in GWT.

Chapter 3 introduced a framework for GWT based on CRT. A method for mapping the pipe wall to a two dimensional (2-D) domain by representing the wall thickness with an equivalent acoustic model was presented. In addition, a structure for the inclusion of

information from high-order helical wave-paths in GWT was described. The benefit to GWT is the virtual extension of the array aperture which increases the number of viewing angles available to the limited view array. A numerical example of the reconstruction of a WTL map containing three defects of varying width and depth was performed. The effect of including increasingly higher orders of helical wave-paths in GWT was tested. Indeed, the inclusion of the high-order helical wave-paths was found to result in increased accuracy of reconstructions.

The problem of compensating for parametric uncertainties was addressed in Chapter 4. These were split into the time independent parametric uncertainties (TIPU), and time dependent parametric uncertainties (TDPU), and addressed separately. A method for the mitigation of the TIPU based on residuals comparing the current state of the pipe to a baseline state through the use of differential traveltimes was presented. A method for the amelioration of TDPU due to thermal variations was also introduced. An experimental study of GWT with, and without thermal variations was performed and the results showed the methods of compensating for TIPU and TDPU to be effective.

A new criterion for the accuracy of CRT and by extension GWT was introduced in Chapter 5. It was validated in its ability to predict agreement between measured and ray theoretical traveltimes, and the ability of CRT to reconstruct the maximum absolute contrast for fast and slow inclusions. It was demonstrated that the limiting effect of the new criterion, based on the relationship between an inclusions size and contrast, only applies to the reconstruction of slow contrast inclusions. In addition, examples of the reconstruction of more complex media that incorporate both fast and slow contrast into a single region were presented.

Finally, in Chapter 6 a parameter study of the GWT problem was performed. The parameters studied described pipe, defect, and array geometries. The study was meant to characterize the performance of GWT for a wide variety of pipes used in the petrochemical industry, as well as defects due to corrosion/erosion patches of multiple sizes. It was demon-

strated that the critical contrast criterion, developed in Chapter 5, can be transformed into a critical defect depth criterion for use with GWT. The array parameters were studied in terms of a statistical analysis of the error in reconstructed defect depth.

7.2 Main findings

This thesis introduces an advanced method for structural health monitoring of oil and gas pipelines by combining ultrasonic guided waves with the CRT algorithm to provide a means of accurately reconstructing the current state of wall thickness degradation in a region enclosed by two ring arrays of sensors, termed GWT. In addition, this thesis has explored the range of applicability of CRT (and by extension GWT) by making links between geometrical diffraction and ray theories to yield a new criterion of accuracy, termed the critical contrast criterion. This will not only have implications for CRT, but also for higher resolution imaging methods that use CRT reconstructions as a starting point. Additionally, the critical contrast criterion is used to construct a critical defect depth criterion that applies directly to GWT. The high accuracy of GWT within the critical defect depth criterion, leads to a structural health monitoring system capable of providing the level of accuracy required for the evaluation of oil and gas assets. Moreover, the critical defect depth criterion serves as a convenient tool for the assessment of GWT reconstruction error. Chapter 1 of this thesis introduced the need for a highly accurate system for structural health monitoring of pipelines in the oil and gas industry. It was concluded that current point monitoring techniques are insufficient due to their limited area coverage.

In Chapter 3 not only was a general framework for GWT introduced, but also the technique for enhancing the resolution of GWT by making use of the helical wave-paths. By including the information within the helical modes up to the m^{th} order, the effective array aperture is extended by a $m + 1$ factor, thus leading to superior ray coverage and hence improved wall thickness estimation accuracy, as well as the suppression of artifacts. A nu-

merical study showed that by considering increasing numbers of helical modes the maximum depth estimation error could be reduced from -10% of nominal wall thickness (when no helical modes are considered) to under 0.5% of nominal wall thickness (when two orders of helical modes are considered).

Further increases in accuracy were obtained by introducing methods for mitigating the effect of parametric uncertainties in Chapter 4. Each method is made possible by considering a residual based on differential traveltimes rather than one based on absolute traveltimes. The use of the differential residual has the effect of mitigating the TIPU. Alleviation of the TDPU resulting from thermal variation necessitated the development of a scheme for predicting the effect of temperature on the baseline traveltimes using the differential residual itself, and an assumed model linking the change in baseline traveltimes to a change in the background wave speed due to temperature. This method was of course only possible because of the thermal stability of the electromagnetic acoustic transducers (EMATs). An experimental study was performed by monitoring an 8" schedule 40 steel pipe with a non-uniform defect (maximum depth 0.78 ± 0.05 mm) over a number of days, and temperatures. By implementing these parametric uncertainty compensation methods in conjunction with the consideration of helical modes up to the second order, GWT was shown to yield reproducible reconstructions of maximum defect depth of 0.78 ± 0.02 mm. Moreover, when thermal effects were studied, the temperatures ranged from approximately 50°C to 175°C, and still an estimated maximum defect depth of 0.79 ± 0.04 mm was obtained.

In Chapter 5 the theory of geometrical diffraction, and ray theory were considered in order to construct a critical contrast criterion which defines the ability of CRT to accurately reconstruct the contrast of an inclusion of given width. Traveltime shift curves constructed by combining geometrical diffraction and ray theories were compared to measured traveltime shifts for contrasts ranging from -40 to 100%, and widths ranging from 10 to 500% of the sensitivity kernel width. It was found that good agreement was obtained when the data picking method detected first-arrivals traveltimes. In addition, the critical contrast criterion

was investigated by testing the ability of CRT to reconstruct positive and negative inclusions whose widths were 25, 50, and 100% of the sensitivity kernel width using a full view circular array. All positive contrast inclusions (contrast up to 100%) were accurately reconstructed when data came from first-arrival traveltimes resulting from full wave simulations, or the eikonal solution. Alternatively, for negative contrast inclusions, the reconstructed contrasts were accurate for a given width up until the critical contrast was reached, and then were observed to saturate just above the critical level.

The critical contrast criterion was studied further in Chapter 6, and adapted for use with the limited view linear arrays used in GWT. It was shown to be especially important for the implementation of GWT studied in this thesis due to the use of the A_0 phase velocity dispersion curve to link wave speed to pipe thickness. This led to all defects being described as regions of negative contrast, and thus the critical contrast criterion applies. In addition, it was shown that the critical contrast can be recast in terms of a critical defect depth normalized by nominal plate thickness. When comparing the reconstructed defect depths of many combinations of pipe, and defect size to the critical defect depth criterion, it was observed that all reconstructed depths abide by this rule, thus confirming that the critical defect depth criterion is universal. It was noted that the absolute error of the reconstructed defect depth is typically below 1% of pipe wall thickness and does not exceed 6% for defects whose nominal sizes were within the critical defect depth criterion. Finally, after analyzing the error in reconstructed defect depths within the critical defect depth criterion, in terms of array parameters, it was observed that the array separation is less sensitive than the defect width, or the number of transducers per array.

7.3 Avenues of future research

In this thesis, GWT has been demonstrated to be effective in reconstructing WTL with high accuracy using data from simulation, and controlled laboratory experiments. While the

results of these experiments are encouraging, it is extremely difficult to test in the laboratory every possible situation that might be encountered in the field. For this reason, the obvious next step is to further validate GWT with field trials. Oil and gas pipelines exist all over the world in a multitude of climates, and carrying various types of feedstock. It is possible that each combination might have a unique effect on the rate of WTL. For this reason a pilot program instituting structural health monitoring using the GWT system outlined in this thesis should be carried out in each type of climate where pipelines exist. This would serve to highlight unforeseen difficulties, and provide future avenues to improve the robustness of GWT.

Another suggested path of research is the development of an eikonal solver that is capable of discerning between the ray paths of geometrical diffraction and ray theory. Ideally, the algorithm would track wavefronts of both geometrical diffraction, and ray theory. This would involve building in a method for the identification of wavefront branches, and subsequently tracking each. It is possible this could result in many wavefronts being tracked if the media is sufficiently complex. An eikonal solver capable of multiple wavefront tracking could be achieved by including some intuition of the laws of refraction and diffraction in the wavefront tracking process. Further difficulty may arise when tracking wavefronts that cross over themselves, as in the case of a wavefront being focused. If this more complex eikonal solver could be built, it would have the potential to greatly increase the ray coverage, and ideally the resolution of ray tomography. This of course leads to the need for a complementary method of identifying the data present in the received signals in order to find appropriate residuals required to perform the model updating that occurs during CRT iteration. This would require that the traveltime data be reevaluated during the solution process of CRT.

List of Publications

Patents

[P1] Patent Application no. PCT/US2014/013843, entitled "Measuring Wall Thickness Loss for a Structure"

Journal Papers

[P2] C.L. Willey, F. Simonetti. On the accuracy of wave speed reconstructions below the resolution scale of ray tomography, *J. Acoust. Soc. Am.* submitted.

[P3] C.L. Willey, F. Simonetti, P.B. Nagy, G. Instanes. Guided wave tomography of pipes with high-order helical modes, *NDT&E International*, **65**, 8-21, 2014.

Refereed Conference Proceedings

[P4] F. Simonetti, P.B. Nagy, A. Brath, C.L. Willey, G. Instanes, A.O. Pedersen. Ultrasonic computerized tomography for continuous monitoring of corrosion and erosion damage in pipelines. *Proceedings of Corrosion/15 NACE International, Dallas, Texas*, pages 1-13, 2015.

[P5] C.L. Willey, F. Simonetti, P.B. Nagy, G. Instanes. Thermal stability of curved ray tomography for corrosion monitoring. *Proceedings of the Review of Progress in QNDE*,

Am. Inst. Phys., volume **1581**, pages 316-323, 2014.

Bibliography

[1] L. Maugeri. Oil: The Next Revolution. Discussion paper 2012-10. Technical report, Belfer Center for Science and International Affairs, Harvard Kennedy School, President and Fellows of Harvard College., 2012.

[2] L. Maugeri. The shale oil boom: a U.S. phenomenon. Discussion paper 2013-05. Technical report, Belfer Center for Science and International Affairs, Harvard Kennedy School, President and Fellows of Harvard College., 2013.

[3] W.H. O. Recovery of oil from oil shale, February 7 1961. US Patent 2,970,826.

[4] L.F. Elkins. Shale oil recovery, May 5 1981. US Patent 4,265,307.

[5] Donald M. Fenton, Harvey Henning, and Ryden L. Richardson. *The Chemistry of Shale Oil and Its Refined Products*, chapter 21, pages 315–325. American Chemical Society, 1981.

[6] James G. Speight. *Handbook of Industrial Hydrocarbon Processes*. Elsevier, 2011.

[7] James G. Speight. *Shale Oil Production Processes*. Elsevier, 2012.

[8] Gary L. Baughman, Ronald L. Gist, and Edwin H. Bentzen. Transportation and marketing of shale oil. In *Proc. of Symposium on Processing of Oil Shale Tar Sands and Heavy Oils joint with Divisions of Petroleum Chemistry and Industrial and Engineering Chemistry*, pages 207–213, 1982.

[9] Institute for Clean and Secure Energy at the University of Utah. A Market Assessment of Oil Shale and Oil Sands Development Scenarios in Utah's Uinta Basin, 2013.

[10] Lekan Popoola, Alhaji Grema, Ganiyu Latinwo, Babagana Gutti, and Adebori Balogun. Corrosion problems during oil and gas production and its mitigation. *Int. J. Ind. Chem.*, 4(1):35, 2013.

[11] R. Heidersbach. *Metallurgy and Corrosion Control in Oil and Gas Production*. John Wiley & Sons, Inc., Hoboken, NJ, USA, 2011.

[12] Z. Ahmad. *Principles of Corrosion Engineering and Corrosion Control*. Elsevier Ltd., Burlington, MA, USA, 2006.

[13] Baotong Lu. Erosion-corrosion in oil and gas production. *Res. Rev. Mater. Sci. Chem.*, 2:19–60, 2013.

[14] Chinedu I. Ossai. Advances in asset management techniques: An overview of corrosion mechanisms and mitigation strategies for oil and gas pipelines. *ISRN Corrosion*, 2012, 2012.

[15] Ramakrishna Malka, Srdjan Nešić, and Daniel A. Gulino. Erosion–corrosion and synergistic effects in disturbed liquid-particle flow. *Wear*, 262(7–8):791 – 799, 2007.

[16] Lisa Demer. Appeals court gives go-ahead to bp investor suit over 2006 alaska oil spills. http://www.adn.com/article/20140213/appeals-court-gives-go-ahead-bp-investor-suit-over-2006-alaska-oil-spills, February 2014.

[17] N.I.I. Mansor, S. Abdullah, A.K. Ariffin, and J. Syarif. A review of the fatigue failure mechanism of metallic materials under a corroded environment. *Eng. Fail. Anal.*, 42(0):353 – 365, 2014.

[18] ASTM Standard A 106/ A 106M 04b (2004). "Standard Specification for Seamless Carbon Steel Pipe for High-Temperature Service". ASTM International, West Conshohocken, PA, 2004.

[19] R. D. Strommen, H. Horn, and K. R. Wold. New technique monitors pipeline corrosion, cracking. *Oil Gas J.*, 91(52):88–93, 1993.

[20] G. Sposito, P. Cawley, and P. B. Nagy. Potential drop mapping for the monitoring of corrosion or erosion. *NDT&E Int.*, 43:394–402, 2010.

[21] GE. Corrosion monitoring installed sensors, June 2009.

[22] F. B. Cegla, P. Cawley, J. Allin, and J. Davies. High-temperature (>500°C) wall thickness monitoring using dry-coupled ultrasonic waveguide transducers. *IEEE Trans. Ultrason., Ferroelectr., Freq. Control*, 58(1):156–167, 2011.

[23] D. N. Alleyne, B. Pavlakovic, M. J. S. Lowe, and P. Cawley. Rapid, long range inspection of chemical plant pipework using guided waves. *Insight*, 43:93–96,101, 2001.

[24] P. Mudge. Field application of the teletest long range ultrasonic testing technique. *Insight*, 43:74–77, 2001.

[25] P. Cawley, M. J. S Lowe, D. N Alleyne, B. Pavlakovic, and P. Wilcox. Practical long range guided wave testing: application to pipes and rail. *Mater. Eval.*, 61(1):66–74, 2003.

[26] R. Carandente and P. Cawley. The effect of complex defects profiles on the reflection of the fundamental torsional mode in pipes. *NDT&E Int.*, 46:41–47, 2012.

[27] G. Instanes, A. Pedersen, M. Toppe, and P. B. Nagy. Constant group velocity ultrasonic guided wave inspection for corrosion and erosion monitoring in pipes. In D. O. Thompson and D. E. Chimenti, editors, *Rev. Prog. Q.*, volume 28, pages 1386–1393. AIP, New York, 2009.

[28] P. B. Nagy, F. Simonetti, and G. Instanes. Corrosion and erosion monitoring in plates and pipes using constant group velocity lamb wave inspection. *Ultrasonics*, 54(7):1832 – 1841, 2014.

[29] D.P. Jansen and D.A. Hutchins. Lamb wave tomography. In *IEEE Proc. Ultrasonics Symposium*, pages 1017–1020. IEEE, 1990.

[30] J. Pei, M. Yousuf, F. Degertekin, B. Honein, and B. Khuri-Yakub. Lamb wave tomography and its application in pipe erosion/corrosion monitoring. *Res. Nondestruct. Eval.*, 8:189–197, 1996.

[31] E.V. Malyarenko and M.K. Hinders. Fan beam and double crosshole lamb wave tomography for mapping flaws in aging aircraft structures. *J. Acoust. Soc. Am.*, 108:1631, 2000.

[32] K. R. Leonard and M. K. Hinders. Guided wave helical ultrasonic tomography of pipes. *J. Acoust. Soc. Am.*, 114(2):767–774, 2003.

[33] L.R. Rose and C.H. Wang. Mindlin plate theory for damage detection: imaging of flexural inhomogeneities. *J. Acoust. Soc. Am.*, 127:754–763, 2010.

[34] P. Belanger, P. Cawley, and F. Simonetti. Guided wave diffraction tomography within the Born approximation. *IEEE Trans. Ultrason. Ferroelectr. Freq. Contr.*, 57:1405–1418, 2010.

[35] A. Volker and J. Bloom. Experimental results of guided wave travel time tomography. In D. O. Thompson and D. E. Chimenti, editors, *Rev. Prog. Q.*, volume 30B, pages 215–222, 2011.

[36] P. Huthwaite and F. Simonetti. High-resolution guided wave tomography. *Wave Motion*, 50(2013):979–993, 2013.

[37] T. Lo. *Seismic Borehole Tomography*. Massachusetts Institute of Technology, Department of Earth, Atmospheric and Planetary Sciences, 1987.

[38] A. J. Devaney. Geophysical diffraction tomography. *IEEE Trans. Geosc. Rem. Sens.*, GE-22:3–13, 1984.

[39] A. J. Devaney. The limited-view problem in diffraction tomography. *Inverse Probl.*, 5:501–521, 1989.

[40] A. L. Kimball and D. E. Lovell. Variation of young's modulus with temperature from vibration measurements. *Phys. Rev.*, 26:121–124, Jul 1925.

[41] D. Colton and R. Kress. *Inverse Acoustic and Electromagnetic Scattering Theory*, volume 93. Springer-Verlag, Berlin, 1992.

[42] A. C. Kak and M. Slaney. *Principles of Computerized Tomographic Imaging*. IEEE Press, New York, 1998.

[43] Michal Kvasnička and Vlastislav Červený. Analytical expression for fresnel volumes and interface fresnel zones of seismic body waves. part 1: Direct and unconverted reflected waves. *Stud. Geophys. Geod.*, 40(2):136–155, 1996.

[44] V. Červený. *Seismic Ray Theory*. Cambridge University Press, 2001.

[45] P.R. Williamson. A guide to the limits of resolution imposed by scattering in ray tomography. *Geophysics*, 56(2):202–207, 1991.

[46] E. Wielandt. On the validity of the ray approximation for interpreting delay times. In Guust Nolet, editor, *Seismic Tomography*, volume 5 of *Seismology and Exploration Geophysics*, pages 85–98. Springer Netherlands, 1987.

[47] 'Oli Gudmundsson. On the effect of diffraction on traveltime measurements. *Geophys. J. Int.*, 124(1):304–314, 1996.

[48] Alison E. Malcolm and Jeannot Trampert. Tomographic errors from wave front healing: more than just a fast bias. *Geophys. J. Int.*, 185(1):385–402, 2011.

[49] Joseph B. Keller. Geometrical theory of diffraction. *J. Opt. Soc. Am.*, 52(2):116–130, Feb 1962.

[50] K. F. Graff. *Wave motion in elastic solids*. Clarendon Press, Oxford, 1975.

[51] J. L. Rose. *Ultrasonic Waves in Solid Media*. Cambridge University Press, 2004.

[52] Horace Lamb. On waves in an elastic plate. *P. Roy. Soc. Lond. A. Mat.*, 93(648):114–128, 1917.

[53] Lord Rayleigh. On the free vibrations of an infinite plate of homogeneous isotropic elastic matter. *P. Lond. Math. Soc.*, 20(357):225–237, 1888-1889.

[54] H. Lamb. On the flexure of an elastic plate. *P. Lond. Math. Soc.*, 21:85, 1889-1890.

[55] B. Pavlakovic and M.S.J. Lowe. Disperse software, v. 2.0.6 (Mechanical Engineering, Imperial College). http://www3.imperial.ac.uk/nde/products and services/disperse, 2000.

[56] Denos C. Gazis. Three dimensional investigation of the propagation of waves in hollow circular cylinders. i. analytical foundation. *J. Acoust. Soc. Am.*, 31(5), 1959.

[57] J. L. Rose. *Ultrasonic Guided Waves in Solid Media*. Cambridge University Press, 2014.

[58] Denos C. Gazis. Three dimensional investigation of the propagation of waves in hollow circular cylinders. ii. numerical results. *J. Acoust. Soc. Am.*, 31(5), 1959.

[59] M. G. Silk and K. F. Bainton. The propagation in metal tubing of ultrasonic wave modes equivalent to Lamb waves. *Ultrasonics*, 17(1):11–19, 1979.

[60] Milton Abramowitz. *Handbook of Mathematical Functions, With Formulas, Graphs, and Mathematical Tables,*. Dover Publications, Incorporated, 1974.

[61] Guoli Liu and Jianmin Qu. Guided circumferential waves in a circular annulus. *J. Appl. Mech.*, 65(2):424–430, June 1998.

[62] Xiaoliang Zhao and Joseph L. Rose. Guided circumferential shear horizontal waves in an isotropic hollow cylinder. *J. Acoust. Soc. Am.*, 115(5), 2004.

[63] P. M. Morse and H. Feshbach. *Methods of Theoretical Physics*. McGraw-Hill Book Company, New York, London, 1953.

[64] J. Hadamard. *Lectures on Cauchy's Problems in Linear Partial Differential Equations*. Yale University Press, New Haven, 1923.

[65] A. Tikhonov. On the solution of incorrectly formulated problems and the regularization method. *Soviet Math. Dokl.*, 4:1035–1038, 1963.

[66] G. R. Pratt, C. Shin, and G. J. Hicks. Gauss–Newton and full Newton methods in frequency–space seismic waveform inversion. *Geophys. J. Int.*, 133(2):341–362, 1998.

[67] R. Potthast. *Point Sources and Multipoles in Inverse Scattering Theory*. Chapman & Hall / CRC, London, 2001.

[68] W. W. Hager and H. Zhang. A survey of nonlinear conjugate gradient methods. *Pac. J. Optim.*, 2(1):35–58, 2006.

[69] G. R. Pratt. Seismic waveform inversion in the frequency domain, part 1: Theory and verification in a physical scale model. *Geophysics*, 64(3):888–901, 1999.

[70] M. Fink. Time reversal acoustics. *Phys. Today*, 50:34–40, 1997.

[71] W. S. Phillips and M. C. Fehler. Traveltime tomography: A comparison of popular methods. *Geophysics*, 56(10):1639–1649, 1991.

[72] P. R. Williamson and M. H. Worthington. Resolution limits in ray tomography due to wave behavior: Numerical experiments. *Geophysics*, 58(5):727–735, 1993.

[73] F. Simonetti. Multiple scattering: The key to unravel the subwavelength world from the far-field pattern of a scattered wave. *Phys. Rev. E*, 73:036619–1, 2006.

[74] F. Simonetti, L. Huang, and N. Duric. On the sampling of the far-field operator with a circular ring array. *J. Appl. Phys.*, 101:083103, 2007.

[75] A. J. Brath, F. Simonetti, P. B. Nagy, and G. Instanes. Acoustic formulation of elastic guided wave propagation and scattering in curved tubular structures. *IEEE Trans. Ultrason., Ferroelectr., Freq. Control*, 2014.

[76] Kane Yee. Numerical solution of initial boundary value problems involving maxwell's equations in isotropic media. *IEEE T. Antenn. Propag.*, 14(3):302–307, May 1966.

[77] Dimitri Komatitsch and Roland Martin. An unsplit convolutional perfectly matched layer improved at grazing incidence for the seismic wave equation. *Geophysics*, 72(5):SM155–SM167, 2007.

[78] P. Huthwaite, A. Zwiebel, and F. Simonetti. A new regularization technique for limited-view sound-speed imaging. *IEEE Trans. Ultrason., Ferroelectr., Freq. Control*, 60(3):603–613, 2013.

[79] G. Instanes, P. B. Nagy, F. Simonetti, and C. L. Willey. Measuring wall thickness loss for a structure, 01 2013. US Patent 61758433.

[80] L. Mažeika and L Draudvilienė. Analysis of the zero-crossing technique in relation to measurements of phase velocities of the lamb waves. *Ultrasound*, 66(2):7–12, 2010.

[81] C. B. Scruby and B. C. Moss. Non-contact ultrasonic measurements on steel at elevated temperatures. *NDT&E Int.*, 26(4):177–188, 1993.

[82] J. C. Dodson and D. J. Inman. Thermal sensitivity of Lamb waves for structural health monitoring applications. *Ultrasonics*, 53(3):677–685, 2012.

[83] G. Nolet. *Seismic tomography*. Cambridge University Press, Cambridge, 2008.

[84] O. Yilmaz. *Seismic data analysis*, volume II. Society of exploration geophysicists, Tulsa, 2001.

[85] C. Li, N. Duric, P. Littrup, and L. Huang. In vivo breast sound-speed imaging with ultrasound tomography. *Ultrasound Med. Biol.*, 35(10):1615–1628, 2009.

[86] F. Simonetti, L. Huang, N. Duric, and P. Littrup. Diffraction and coherence in breast ultrasound tomography: A study with a toroidal array. *Med. Phys.*, 36(7):2955–2965, 2009.

[87] J Wiskin, D.T. Borup, S.A. Johnson, and M. Berggren. Non-linear inverse scattering: High resolution quantitative breast tissue tomography. *J. Acous. Soc. Am.*, 131(5):3802–3813, 2012.

[88] N. V. Ruiter, Mi. Zapf, R. Dapp, T. Hopp, W. A. Kaiser, and H. Gemmeke. First results of a clinical study with 3d ultrasound computer tomography. In *IEEE Int. Ultrason. Symp.*, pages 651–654. IEEE, 2013.

[89] P. Palanichamy, A. Joseph, T. Jayakumar, and R. Baldev. Ultrasonic velocity measurements for estimation of grain size in austenitic stainless steel. *NDT&E Int.*, 28(3):179–185, 1995.

[90] D. I. Crecraft. The measurement of applied and residual stresses in metals using ultrasonic waves. *J. Sound Vib.*, 5(1):173–192, 1967.

[91] C. L. Willey, F. Simonetti, P. B. Nagy, and G. Instanes. Guided wave tomography of pipes with high-order helical modes. *NDT&E Int.*, 65:8–21, 2014.

[92] E. Wolf. Three-dimensional structure determination of semi-transparent objects from holographic data. *Opt. Commun.*, 1:153–156, 1969.

[93] A. Sentenac, C. A. Guerin, P. C. Chaumet, F. Drsek, H. Giovannini, N. Bertaux, and M. Holschneider. Influence of multiple scattering on the resolution of an imaging system: a cramer-rao analysis. *Opt. Express*, 15(3):1340–1347, 2007.

[94] F. Simonetti, M. Fleming, and Marengo E. A. Illustration of the role of multiple scattering in subwavelength imaging from far-field measurements. *J. Opt. Soc. Am. A*, 25(2):292–303, 2008.

[95] C. Li and N. Duric. Resolution limitation of travel time tomography: beyond the first fresnel zone. In *Proc. SPIE Medical Imaging*, pages 86751D–86751D. International Society for Optics and Photonics, 2013.

[96] R. G. Pratt, F. Gao, C. Zelt, and A. Levander. The limits and complementary nature of traveltime and waveform tomography. In *J. Conf. Abstr.*, volume 7, pages 181–182, 2002.

[97] H. Marquering, G. Nolet, and F. A. Dahlen. Three-dimensional waveform sensitivity kernels. *Geophys. J. Int.*, 132(3):521–534, 1998.

[98] F. A. Dahlen, S. H. Hung, and G. Nolet. Fréchet kernels for finite-frequency traveltimes—I. theory. *Geophys. J. Int.*, 141(1):157–174, 2000.

[99] S. H. Hung, F. A. Dahlen, and G. Nolet. Fréchet kernels for finite-frequency traveltimes II. examples. *Geophys. J. Int.*, 141(1):175–203, 2000.

[100] J. Spetzler and R. Snieder. The fresnel volume and transmitted waves. *Geophysics*, 69(3):653–663, 2004.

[101] S. H Hung, F. A. Dahlen, and G. Nolet. Wavefront healing: a banana–doughnut perspective. *Geophys. J. Int.*, 146(2):289–312, 2001.

[102] J.A. Sethian. A fast marching level set method for monotonically advancing fronts. *Proc. Nat. Acad. Sci. USA*, 93(4):1591, 1996.

[103] S. Geoltrain and J. Brac. Can we image complex structures with first-arrival traveltime? *Geophysics*, 58(4):564–575, 1993.

[104] B. Boashash. Estimating and interpreting the instantaneous frequency of a signal. I. fundamentals. *Proc. IEEE*, 80(4):520–538, 1992.

[105] J. I. Sabbione and D. Velis. Automatic first-breaks picking: New strategies and algorithms. *Geophysics*, 75(4):V67–V76, 2010.

Appendix A

Definition of the inhomogeneous region

The inhomogeneous region shown in Fig. 5.9(a) is derived from a function $p(x_1, x_2)$ that is the weighted sum of Bessel functions of the first kind and order two, J_2, according to

$$p(x_1, x_2) = \sum_{m=1}^{3} \sum_{k=1}^{3} Q_{mk} J_2 \left(2 z_m \frac{\sqrt{x_1^2 + x_2^2}}{W} \right) \sin(k \angle (x_1 + i x_2) + \pi/2), \tag{A.1}$$

where z_m are the zeros of the Bessel function. The factor Q_{mk} is a matrix of coefficients that determine the contour of the inhomogeneous profile and are given in Tab. A.1. The support of the inhomogeneous region is made compact via,

$$g(x_1, x_2) = \begin{cases} p(x_1, x_2) & \text{if } \sqrt{x_1^2 + x_2^2} \leq W/2 \\ 0 & \text{if } \sqrt{x_1^2 + x_2^2} > W/2 \end{cases}, \tag{A.2}$$

which limits the inhomogeneous profile to a circular region as wide as the sensitivity kernel, and centered at the origin. The inhomogeneous contrast is finally obtained by scaling the

(m,k)	Q_{mk}
(1,1)	0.0844
(1,2)	0.8001
(1,3)	0.1818
(2,1)	0.3998
(2,2)	0.4314
(2,3)	0.2638
(3,1)	0.2599
(3,2)	0.9106
(3,3)	0.1455

Table A.1: Factors of Eq. (A.1), noted as Q_{mk}.

expression given in Eq. (A.2), as

$$\mu(x_1, x_2) = 0.4g(x_1, x_2)/g_{max}, \tag{A.3}$$

which has peak values of $\pm 40\%$.